Printed and Templated 3D MXene Structures for Energy Storage Applications

A thesis presented to Trinity College Dublin, The University of Dublin

for the degree of Doctor of Philosophy in Chemistry

by Dahnan Spurling B. A. (Mod.)

Under the supervision of Prof. Valeria Nicolosi

May 2023

Careful! We don't want to learn anything from this.

Calvin

DECLARATION

I declare that this thesis has not been submitted as an exercise for a degree at this or any other university and it is entirely my own work. I agree to deposit this thesis in the University's open access institutional repository or allow the Library to do so on my behalf, subject to Irish Copyright Legislation and Trinity College Library conditions of use and acknowledgement. I consent / do not consent to the examiner retaining a copy of the thesis beyond the examining period, should they so wish (EU GDPR May 2018).

Signed:_____

Date:_____

Dahnan Spurling B. A. (Mod.)

ABSTRACT

Recently, MXenes have emerged as a promising family of materials for a variety of energy storage devices, with much of the work surrounding supercapacitors based on $Ti_3C_2T_x$. Nanosheets of this material combine a metallically conductive titanium carbide core and a surface functionalised by a range of polar and pseudocapacitive surface groups such as F, O and OH – denoted T_x. This Thesis first covers the synthesis and characterisation of $Ti_3C_2T_x$ MXene, along with a facile freeze-thaw method for enhancing the yield of delaminated flakes by 42 ± 6%. The high conductivity and capacitance of this material makes it ideal for supercapacitors, though real-world applications will need control of electrode structure, as excessively dense and/or thick electrodes compromise both rate performance and specific capacitance. Therefore, this thesis describes two methods to create hierarchically structured 3D $Ti_3C_2T_x$ electrodes at distinct length scales and for distinct applications.

At smaller scales, such as internet of things (IoT) and portable electronics, microsupercapacitors may present a solution to the requirement for compact energy storage. Specifically, directly incorporating microsupercapacitors into the product through printing is very appealing. To address the ion transport and capacitance issues of more conventional, dense, 2D printed films, we show that aerosol jet printing (AJP) of aqueous $Ti_3C_2T_x$ inks can be used to fabricate symmetric, interdigitated microsupercapacitors where the 3D structured microsupercapacitors exhibit up to 97% greater areal capacitance than mass equivalent planar microsupercapacitors, up to 138 mF/cm^2 at 5 mV/s. Additionally, three-electrode measurements of high areal loading 3D electrodes resulted in exceptional values for areal and volumetric capacitance of 3.47 F cm^{-2} and 347 F cm^{-3} respectively at 5 mV s^{-1}.

For larger, macroscopic electrodes, this Thesis presents a method to create hierarchical 3D networked $Ti_3C_2T_x$ thin film "aeromaterial" with tuneable nano- and microstructure. Using sacrificial templates of sintered ZnO tetrapods, and careful control of the coating process, highly porous MXene structures with tailored layer thickness are obtained. These structures may be compressed to a desired thickness, from 2 mm to 0.05 mm to tailor the microstructure. By balancing porosity and thickness, electrodes that combine a high areal loading of up to ~7.2 mg cm^{-2}, high density of ~1440 mg cm^{-3}, and high electrochemical performance of 240 F g^{-1} and 140 F cm^{-3} are demonstrated. Optimising the above properties, electrodes with a remarkable areal capacitance of ~1.4 F cm^{-2} are achieved, even at high rates of 200 mV s^{-1}, outperforming other state of the art MXene based electrodes of comparable density and thickness by almost 200%. I hope that this concept will pave the way to transfer the exceptional properties of nanomaterial thin film electrodes to the macroscopic level, enabling the development of advanced, high-performance electrodes for practically relevant energy storage applications.

ACKNOWLEDGEMENTS

Ask someone to name a scientist and they will give you: “Einstein”, “Hawking”, or “that English fella on the TV with the big mouth who talks about, you know, space? Come on, you know him, you do”. These individuals possess some perfect combination of drive, genius, showmanship, and let’s face it, staggering luck. Luck insofar as their neurons fired in the right way, at the right time, in response to the right problem. They are figures who may singlehandedly revolutionise their field, make stacks of cash, become a Nobel laureate, or perhaps even receive the greatest accolade of all: become a person to whom quotes are misattributed on low-effort motivational images that end up shared on your uncle’s Facebook page.

Real science and real scientists aren’t like that. We have teammates, friends, mentors, and in my case, it most definitely has taken a village. First and foremost, I would like to thank my incredible supervisor Prof. Valeria Nicolosi, for her inspiring aura, her steadfast support and her plain badassery whenever there’s a problem we are facing. Next, I would not be able to undertake this research without the advice and camaraderie from members of the Nicolosi group. Special mentions given to Dr. Matthias Kremer, Dr. João Coelho, Dr. Sergio Pinilla, Dr. Daire Tyndall, Dr. Oskar Ronan, Sean Ryan, Anastasiia Shandra and Lucia Hughes. I would also like to recognise the brilliance of my colleagues in Kiel. Firstly, the brilliant *engineer* Dr. Helge Krüger, who after his stay in Ireland was unceremoniously cut short by the pandemic after only two weeks, still managed to work (with me, bless him) on our aeromaterial project over the following two years. I would also like to thank the guiding hand of Dr. Fabian Schütt, without whom the project would not have been such a success.

I am very grateful for the financial backing for my projects, provided by the Irish Research Council and Intel under the Enterprise Partnership Ph.D. Scholarship, as well as the support of the School of Chemistry, and Trinity College Dublin as a whole. I would also like to thank Prof. Neville Cox for his administrative aid concerning the aforementioned institution.

Of course, none of this would have been possible if I wasn't born, so I would like to thank my parents, Dorothy, and Graham whose unconditional love I couldn't be without.

Last but certainly not least is Jason. This isn't some perfunctory nod to my partner because *everyone* has to acknowledge their partner, but a profound thanks. A thanks for all things you do, for all the things you say (and for all the things you don't). Thank you for being there for me as I stumble my way through my silly little endeavours.

CONTENTS

List of Figures

LIST OF ABBREVIATIONS AND ACRONYMS

0D – Zero-Dimensional

1D – One-Dimensional

2D – Two-Dimensional

2.5D – Two-point-five-Dimensional

3D – Three-Dimensional

ADF – Annular Dark Field

AE – Auger Electron

AJP – Aerosol Jet Printing

AM – Additive Manufacturing

BF – Bright Field

BSE – Backscattered Electron

CE – Counter Electrode

CNTs – Carbon Nanotubes

cTEM – Conventional Transmission Electron Microscopy

CV – Cyclic Voltammetry

DARPA – Defense Advanced Research Projects Agency

DC – Direct Current

DF – Dark Field

DFT – Density Functional Theory

DOS – Density of States

EDLC – Electrostatic Double Layer Capacitance

EDX – Energy Dispersive X-ray Spectroscopy

EELS – Electron Energy Loss Spectroscopy

EIS – Electrochemical Impedance Spectroscopy

ESB – Energy-Selective Backscattered Electron

EV – Electric Vehicle

FAD – Freeze-Thaw Assisted Delamination

FEG – Field Emission Gun

FIB – Focused Ion Beam

GCD – Galvanostatic Charge/Discharge

HAADF – High Angle Annular Dark Field

HDI – Human Development Index

HOMO – Highest Occupied Molecular Orbital

IDS – Drain-to-Source Current

IHP – Inner Helmholtz Plane

IJP – Inkjet Printing

LIB – Lithium-Ion Battery

LSPR – Localised Surface Plasmon Resonance

LUMO – Lowest Unoccupied Molecular Orbital

MICE – Mesoscale Integrated Conformal Electronics

MILD – Minimally Intensive Layer Delamination

Near-IR – Near-Infrared

NMR – Nuclear Magnetic Resonance

OHP – Outer Helmholtz Plane

PLA – Polylactic acid

PTFE – Polytetrafluoroethylene

PV – Photovoltaic

RE – Reference Electrode

rGO – Reduced Graphene Oxide

SCCM – Standard Cubic Centimetres per Minute

SE – Secondary Electron

SEM – Scanning Electron Microscopy

STEM – Scanning Transmission Electron Microscopy

STP – Standard Temperature and Pressure

TBAOH – Tetrabutylammonium hydroxide

TEM – Transmission Electron Microscopy

TMDs – Transition Metal Dichalcogenides

UV-Vis – Ultraviolet-Visible

VDS – Drain-to-Source Voltage

WE – Working Electrode

XANES – X-ray Absorption Near Edge Structure

XAS – X-ray Absorption Spectroscopy

XRD – X-ray Diffraction

COMMUNICATIONS

Publications

Krüger, H., **Spurling. D.**, Kohlmann, N., Rasch, F., Kremer, M.P., Kienle, L., Adelung, R., Nicolosi, V. & Schütt, F. 3D networked MXene thin films for high performance supercapacitors. *Nat. Mat.* Under review (2022).

Cabré, M.B., **Spurling, D**., Martinuz, P., Longhi, M., Schröder, C., Nolan, H., Nicolosi, V., Colavita, P.E. & McKelvey, K. Pseudocapacitance beyond intercalation: probing pseudocapacitance of MXene monolayers at the nanoscale. *Nat. Commun.* Under review (2022).

Ryan, S., **Spurling, D.**, Browne, M., Zhussupbekova, A., McKeown, L., Douglas-Henry, D., Prendeville, L., Shvets, I. & Nicolosi, V. Single walled carbon nanotube functionalisation in printed supercapacitor devices and shielding effect of Tin(II) Oxide. *Electrochim. Acta*. Under review (2022)

Tyndall, D., Gannon, L., Hughes, L., Carolan, J., Pinilla, S., Jaśkaniec, S., **Spurling, D.**, Ronan, O., McGuinness, C., McEvoy, N., Nicolosi, V. & Browne, M.P. Understanding the Effect of MXene in a TMO/MXene Hybrid Catalyst for the Oxygen Evolution Reaction. *NPJ 2D Mat*. Under review (2022).

Asaro, G.A., Solazzo, M., Suku, M., **Spurling, D.**, Genoud, K., Gonzalez, J.G., O'Brien, F., Nicolosi, V. & Monaghan, M.G. Crosslinked extracellular matrix biomaterials functionalized with 2D-nanomaterial MXenes for cardiac tissue engineering drive iPSC-derived cardiomyocyte maturation. *NPJ 2D Mat.* Under review (2022).

Piatti, E., Arbab, A., Galanti, F., Carey, T., Anzi, L., **Spurling, D.**, Roy, A., Zhussupbekova, A., Patel, K.A., Kim, J.M., Daghero, D., Sordan, R., Nicolosi, V., Gonnelli, R.S. & Torrisi, F. Charge transport mechanisms in inkjet-printed thin-film transistors based on two-dimensional materials. *Nat. Electron.* **4**, 893–905 (2021).

Borghetti, M., Serpelloni, M., Sardini, E., **Spurling, D**. & Nicolosi, V. Temperature influence on $Ti_3C_2T_x$ lines printed by aerosol jet printing. *Sensors Actuators A Phys.* **332**, 113185 (2021).

Taurisano, N., Bravetti, G., Carallo, S., Liang, M., Ronan, O., **Spurling, D.**, Coelho, J., Nicolosi, V., Colella, S., Gigli, G., Listorti, A. & Rizzo, A. Inclusion of 2D transition metal dichalcogenides in perovskite inks and their influence on solar cell performance. *Nanomaterials* **11**, 1–15 (2021).

Oral Presentations

Spurling, D., Kremer, M.P., Coelho, J., Zhang, C.J., Nerl, H., McEvoy, N., & Nicolosi, V. All-MXene 3D Aerosol-Jet Printed Microsupercapacitors. IIM 2022 (June 29 – July 01), Kiel, Germany.

Spurling, D., Krüger, H., Kremer, M.P., Adelung, R., Schütt, F. & Nicolosi, V. Printed and Templated 3D $Ti_3C_2T_x$ MXene Structures for Energy Storage Applications. MRS Spring Meeting 2022 (May 8 – 13), Honolulu, HI, USA.

Poster Presentations

Spurling, D., Kremer, M.P., Coelho, J., Zhang, C.J., Nerl, H., McEvoy, N., & Nicolosi, V. All-MXene 3D Aerosol-Jet Printed Microsupercapacitors. ECS PRiME 2020 (October 4 – 9), Honolulu, HI, USA (remote due to restrictions).

Spurling, D., Kremer, M.P., Coelho, J., Zhang, C.J., Nerl, H., McEvoy, N., & Nicolosi, V. 3D Printed All-MXene Microsupercapacitors. Flatlands 2019 (September 2 – 6), Toulouse, France.

1 INTRODUCTION

Ever since our ancestors began using stone tools, around 2.6 million years ago,[1] technology and materials science have been used both for our collective benefit: “sharp rock crack nut” and our detriment: “sharp rock crack skull”. A glance at the timeline of human history from Stone to Bronze to Iron Age tells us that our development has been defined by the materials we have been able to master. This is because unlike other animals, our ability to produce specialised tools frees us in part from the limitations of our biology. We don’t need millions of years of evolution to fly, we can just build an aeroplane. With the breadth of what our tools have allowed us to achieve thus far, it’s only natural that society has been influenced in turn by the materials from which its foundations are quite literally built. Most notably, it’s hard to overstate the effect that steel, concrete, and silicon have had over the last two centuries, ushering in an age of (relative) peace and abundance. However, much like the Bronze Age weapon, mastery of these materials has been a double-edged sword. For every piece of infrastructure, every building, and every thinking machine there is a price; to be paid for by ecosystems and the people least able to afford it. This reality presents us with a moral imperative to eliminate our CO_2 emissions, without hindering the advancement of developing nations. For this we need new tools and new materials – because we have yet to find a problem which we materials scienced our way into that we couldn’t materials science our way out of.

It is encouraging then, that we have a growing list of nanostructured materials whose unique properties may yet provide solutions to the most pressing technical challenges that we face. If the middle of the 20th century to early 21st century was the Silicon Age, perhaps we will look back on today as the beginning of the nanomaterials age. In recent decades, research and development in nanoscience has seen a meteoric rise, though it is important to note that the unique properties of nanostructured materials have been unwittingly exploited for millennia.[2] Metallic (often copper) nanoparticles were used to create red glass in Egypt and the Levant as far back as 1300 BCE,[3] and carbon nanotubes as well as cementite nanowires have been found to reinforce Wootz steel blades.[4] It wasn't until 1857 that material properties would be linked to the dimensions of the material itself, when Michael Faraday created colloidal dispersions of gold. The red liquid came as a result of etching gold leaf, however Faraday noticed a cone of scattered light appeared when the dispersion was illuminated.[5] He correctly reasoned that this phenomenon arose from miniscule gold particles in suspension rather than dissolved gold salts, though directly resolving such particles directly would have to wait nearly a century for the advent of electron microscopy.

Nowadays, we have access to a plethora of fascinating materials, the full implications of which are only beginning to be explored. Of particular importance to this Thesis are nanomaterials used for energy storage applications. Specifically, supercapacitors, whose high-power density and cycle stability come at the expense of energy density.[6] In this context, nanostructured materials such as graphene,[7] carbon black,[8] or MXene [9] are particularly attractive for high-performance supercapacitor electrodes due to their high conductivity, large surface area, and redox activity. To bring these materials from the lab to the market, practical devices will need to be created. Practical energy storage

devices need high areal loading, which requires thick electrodes, but the nanomaterials must retain as much of their theoretical performance as possible, or they are pointless.[10] Conventional methods to fabricate thick films of nanostructured materials show a drastic decrease in performance due to long, meandering diffusion paths that strongly inhibit ion transport, limiting both the response time and the accessible surface area of the electrode.

To circumvent these issues, this Thesis will outline two sophisticated techniques to produce hierarchical 3D structured electrodes of $Ti_3C_2T_x$ MXene. The synthesis and characterisation of this material will be covered in detail in Chapter 3. Using this material, Chapter 4 will present aerosol jet printing of 3D structured MXene microsupercapacitors with exceptional areal capacitance. Finally, Chapter 5 will demonstrate that high areal capacitance as well as high charge and discharge rates can be achieved *via* template-based fabrication of thick 3D networked MXene electrodes.

1.1 Nanomaterials

For many people, the words “nanomaterial” or “nanotechnology” probably conjure images of mobile swarms of tiny robots, though Prof. Coleman and Brownian motion thoroughly undermined the feasibility of this sci-fi staple during our undergraduate nanomaterials course. Instead, nanotechnology, nanoscience, etc. refer to the enormously broad and interdisciplinary study of both the fundamental properties and potential applications of nanomaterials. Most often, a nanomaterial is defined as any material with at least one of its dimensions being less than 100 nm,[11] though more rigorous definitions have been proposed.[12]

The menagerie of nanomaterials can be broken down into three categories: zero-dimensional (0D), one-dimensional (1D) and two-dimensional (2D). Nanoparticles, fullerenes, and large molecules are approximately point-like, and so are referred to as 0D; nanotubes and nanowires are roughly linear and referred to as 1D; and nanosheets are roughly planar and referred to as 2D.

1.2 MXenes

The MXene family of 2D nanomaterials has garnered a staggering amount of interest from the materials science community over the last decade.

1.2.1 MXene Precursors: MAX Phases

MAX phases are a large family of more than 60 ternary metal carbides and nitrides with anisotropic properties that arise from their laminated structure.[13] These materials have the formula $M_{n+1}AX_n$, where M is an early transition metal, A is an A-group element of groups 13 or 14, X is carbon and/or nitrogen and n = 1, 2 or 3. They possess a hexagonal structure, with X atoms occupying octahedral sites within approximately close-packed M layers. These $M_{n+1}AX_n$ layers are interspaced by A layers, forming a laminar overall structure. Examples of the 211 (n = 1) stoichiometry MAX phases were initially discovered in the early 1960s in Vienna and dubbed H-phases.[14–16] This family was expanded with discovery of three related 312 (n = 2) phases such as Ti_3SiC_2 in the late 60s.[13,17] In the years following, there was a dearth of research in this field until > 99% pure Ti_3SiC_2 was synthesised and characterised by Barsoum et al. in 1996.[18] The group later went on to create a general classification for this entire family of materials

calling them $M_{n+1}AX_n$ phases or more simply, MAX phases, in the wake of their discovery of Ti_4AlN_3 in 1999.[19,20] In terms of their properties, MAX phases have much in common with binary metal carbides or nitrides such as TiC, notably in their stiffness, as well as thermal and electrical conductivity. Where they differ is in mechanical properties. They are easily machinable; soft in comparison to other ceramics; and resistant to both physical damage and thermal shock.[13,21] It is this intriguing hybridisation of metallic and ceramic traits that led to a resurgence in MAX phase research in the 2000s.

The interleaved A atoms are known to be more loosely bound than the $M_{n+1}AX_n$ blocks, leading a commensurate increase in A-layer reactivity as well as anisotropy in the electrical and mechanical properties of the system overall.[22] For example, in the case of Ti_3AlC_2, the weaker M-A bonding is evidenced in the thermal decomposition (*in vacuo*) of MAX phases according to the reaction:[23]

$$M_{n+1}AX_n \xrightarrow{\Delta} nMX + A + M \quad (1)$$

This does not result in a laminar $M_{n+1}AX_n$ system, but rather a bulk, cubic MX_x phase owing to the high temperature sublimation of both the A and M species.[24,25] Similar loss of the A species, de-twinning, and formation of a 3D cubic MX_x phase occurs when MAX phases are immersed in liquid Na_3AlF_6.[26] The relatively weak M-A bonding would later be exploited to exfoliate MAX phases into 2D MXene nanoflakes.

1.2.2 Exfoliated MAX phases: MXenes

In 2011, Naguib et al. reported the first known instance of the selective removal of the A-layer and subsequent exfoliation of the $M_{n+1}AX_n$ blocks into 2D nanoflakes.[27] Ti_3C_2 would be the first in a new family of MAX phase-derived nanomaterials, named "MXenes" for their morphological similarities to graphene. This nomenclature is even more apt considering that Ti_3SiC_2 was deemed to be somewhat of a Si analogue of graphite as far back as the '90s, owing to its morphology, conductivity, and self-lubricity.[28] In the initial study, Ti_3AlC_2 was immersed in concentrated HF for 2 hours and sonicated in methanol for 5 minutes, producing sheets of Ti_3C_2. The general reaction for HF etching of MAX phases given below:[28]

$$M_{n+1}AlX_n + 3HF = AlF_3 + M_{n+1}X_n + 1.5H_2 \quad (2)$$

The etched MXene is more properly denoted $M_{n+1}AX_nT_x$ where T_x are the surface terminations introduced due of the etching environment used. In the above conditions, the surface of the MXene, for example $Ti_3C_2T_x$, will be terminated by O, OH, and F groups[29–31] as shown in Figure 1.1. This will occur according to the following overall reactions:

$$Ti_3AlC_2 + 3HF = AlF_3 + Ti_3C_2 + 1.5H_2 \quad (3)$$

$$Ti_3C_2 + 2H_2O = Ti_3C_2O_2 + 2H_2 \quad (4)$$

$$Ti_3C_2 + 2H_2O = Ti_3C_2(OH)_2 + H_2 \quad (5)$$

$$Ti_3C_2 + 2HF = Ti_3C_2F_2 + H_2 \quad (6)$$

This HF immersion synthesis was extended to other MAX phases and used to successfully etch and exfoliate a wide range of new MXenes beyond $Ti_3C_2T_x$, including Ti_2CT_x, Nb_2CT_x, V_2CT_x, $(Ti_{0.5}Nb_{0.5})_2CT_x$, $(V_{0.5}Cr_{0.5})_2C_2T_x$, Ti_3CNT_x and $Ta_4C_3T_x$ over the following 3 years.[28,32,33]

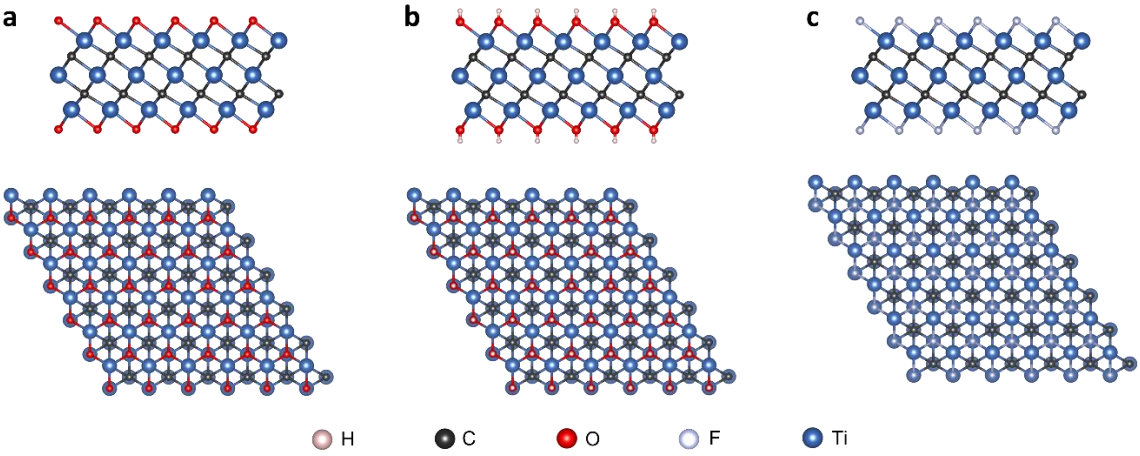

Figure 1.1: Structure of $Ti_3C_2T_x$ MXene with the typical surface terminations arising from HF etching. In each case, the view is down the a-axis on top and the c-axis on bottom. Figure a: $Ti_3C_2O_2$, b: $Ti_3C_2(OH)_2$, c: $Ti_3C_2F_2$. Structures were created using VESTA 3.

Given the hazards inherent in HF storage and handling, a safer synthesis route for MXenes was sought. This manifested in the form of an HCl-LiF etchant, that yielded a $Ti_3C_2T_x$ 'clay' that could be rolled into conductive, high capacitance films.[34] This method used ultrasonication as before to delaminate the etched multilayer MXene, yielding monolayer flakes of sub-micron lateral size. Additionally, ^{1}H and ^{19}F nuclear magnetic resonance (NMR) spectra of $Ti_3C_2T_x$ revealed a huge disparity in F termination abundance when comparing the HF and HCl-LiF etching routes, owing to the much higher F^- concentration present in the HF etchant.[31,35] The overall

stoichiometry which was derived for $Ti_3C_2T_x$ using the HF synthesis and HCl-LiF synthesis routes were, respectively:

$$Ti_3C_2O_{0.54}(OH)_{0.12}F_{0.8} \quad (7)$$

and

$$Ti_3C_2O_{0.84}(OH)_{0.06}F_{0.25} \quad (8)$$

This clearly shows the variation in surface chemistry which results from differing etching environments. Despite the much less aggressive etchant, the HCl-LiF method produces acceptable yields of delaminated material because LiF in addition to providing F^- ions essential to the etching of Al, also provides Li^+ ions which intercalate between the etched layers and assist in delamination, water alone being insufficient to delaminate the material. The addition of organic intercalants such as tetrabutylammonium hydroxide (TBAOH) were later shown to be effective in scaling up yield of delaminated material, further increasing interlayer spacing and the c-lattice parameter to exfoliate the layers more thoroughly.[36]

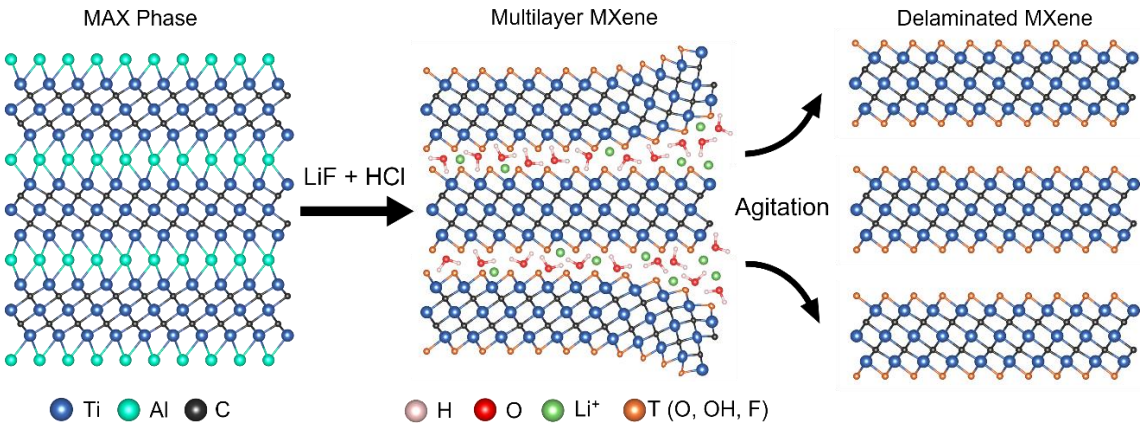

Figure 1.2: Schematic showing the etching and delamination of $Ti_3C_2T_x$ MXene using the MILD synthesis. The structure of the MXene and its parent Ti_3AlC_2 MAX phase is represented, viewing down the a-axis. Structure visualised using VESTA 3.

Further optimisation of the HCl-LiF method, using an excess of LiF for better intercalation, allowed the sonication step to be cut entirely [37] and yielded larger (> 2 µm) flakes which were less defective.[38] This method would be referred to as the minimally intensive layer delamination (MILD) method in literature thereafter.[39] While highly effective, this route has only been shown to work with a handful of MAX phases, Ti_3AlC_2,[34] Mo_2Ga_2C,[40] Ti_2AlC,[41] and Ti_3AlCN.[42]

1.2.3 Properties of MXenes

As with their precursor MAX phases, all non-terminated MXenes are predicted to be metallic,[43] having a high density of states (DOS) at the Fermi level. Surface terminations are an inevitability however, and they have a profound effect on the electronic properties of MXene flakes. For example, a number of MXenes outside the scope of this thesis become semiconducting depending on their surface functionalisations; these include Sc_2CT_x, Ti_2CO_2, Zr_2CO_2, and Hf_2CO_2.[43] Density

functional theory (DFT) studies reveal that this metal-to-semiconductor transition occurs due to complete oxidation of the M species, and consequent shift of the Fermi energy down to the gap between M species' d-bands and X species' p-bands.[44] In general, MXenes exhibit a set of interesting and in some ways atypical characteristics with respect to other 2D materials. For example, a huge boon for $Ti_3C_2T_x$ when compared to other 2D materials such as graphene is the retention of its metallic conductivity when terminated with hydrophilic surface groups. This allows the creation of highly stable, surfactant-free aqueous dispersions of conductive 2D nanosheets. The stability arises from the negative charge on the surface of the sheets at neutral and basic pH. Measurements reveal an isoelectric point at pH = 2.36 (the pH at which a molecule carries no net charge in solution) and ς-potential of approximately -30 mV at a pH above 6.[45] Zeta potential refers to the difference in potential between the double layer at the surface of a particle in dispersion and the surrounding solvent. Sufficiently small particles with a high absolute ς-potential will resist aggregation and form a colloid.[46] The retention of metallic conductivity while exhibiting strong hydrophilicity is in stark contrast to graphene/graphene oxide which becomes insulating at high O fractions due to the loss of the conjugated sp^2 system.[47] $Ti_3C_2T_x$'s metallic conductivity has been verified experimentally, having a linear dependence of drain-to-source current (IDS) on drain-to-source voltage (VDS).[37] Indeed, $Ti_3C_2T_x$ films have been demonstrated with direct current (DC) conductivity approaching 15000 S cm^{-1},[48] greatly exceeding that of graphene or reduced graphene oxide (rGO) thin films at around 550 S cm^{-1}.[49,50] According to theoretical models, this metallic conductivity should be preserved even with a moderate number of defects introduced.[38]

Pertinent to this thesis is the excellent performance of MXenes (specifically $Ti_3C_2T_x$) as the active material for supercapacitor electrodes.[51] Using *in-situ* electrochemical X-ray absorption spectroscopy (XAS) measurements, it was determined that the electrochemical behaviour of $Ti_3C_2T_x$ in aqueous H_2SO_4 is primarily pseudocapacitive,[52] that is, its capacitance arises predominately as a result of reversible redox reactions, see Section 1.3.2. During charge/discharge, the X-ray absorption near edge structure (XANES) spectra revealed a shift in the Ti K-edge pointing to a continuous change in the average Ti oxidation state, making $Ti_3C_2T_x$ a true pseudocapacitive material. It was believed by the authors that ion intercalation provided access to the metal oxide sites, while the inner titanium carbide layer provided the conductivity needed for charge transfer. This was reinforced in a computational study to understand the capacitance mechanism in H_2SO_4.[53] Charge storage was rationalised through redox reactions on the O and OH functional groups, as well as double layer capacitance. The overall capacitance was calculated to be dominated by proton transfer (pseudocapacitance) through the functional groups, hindered by the double-layer charging.

1.3 Energy Storage Devices

Energy storage devices play a critical role in society and industry today. They are used to store excess energy that can be used at a later time, and in the face of runaway climate change, they have growing economic, ecological, and political importance. The most commonly encountered types of energy storage devices are fuel cells, batteries, capacitors, and supercapacitors.[54]

Fuel cells are devices that convert a fuel's chemical energy into electricity through an electrochemical reaction. They consist of an anode and a cathode, separated by an ionically conductive membrane. H_2, when used as a fuel, is ionised to H^+ at the anode, setting up an electron flow to the cathode. Here, it reacts with the oxygen and the electrons to produce water. The flow of electrons from anode to cathode is harnessed to do work. Fuel cells have the advantage of being able to operate continuously as long as they have a supply of fuel and oxygen, and are relatively efficient, achieving energy conversion efficiencies of up to 60%.[55] Their reliance on an external fuel supply gives them excellent energy density (see Ragone plot in Figure 1.3), however they suffer from poor power density due to the sluggish kinetics of oxygen reduction reaction (ORR).[56] Fuel cells are used in a variety of applications, including electronic devices, EVs, and stationary power generation. Fuel cells are of increasing import as we decarbonise our energy supply and promise to aid in reducing energy costs and improving energy security.

As seen in Figure 1.3, batteries are lower in energy density but higher in power density than fuel cells. Batteries store chemical energy and release it as electricity when needed, consisting of an anode and a cathode separated by an electrolyte. As a battery discharges, a reaction at the anode releases electrons which flow through an external circuit to the cathode. Having acceptable energy and power density and having no reliance on fuel, batteries, specifically Li-ion batteries have found their way into the pocket of nearly every person on earth, and an increasing number of driveways.[57]

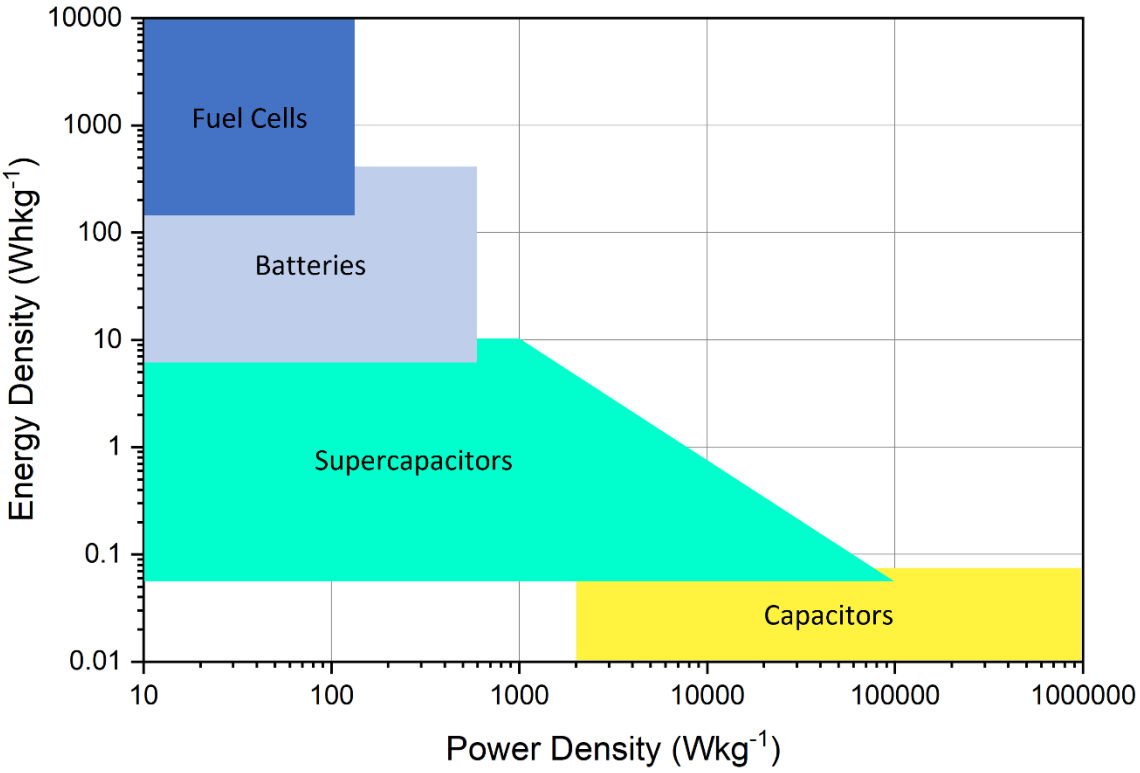

Figure 1.3: Ragone plot illustrating the typical power and energy density characteristics of common energy storage devices. Based on data from Halper, M.S. and Ellenbogen, J.C.[58]

Though batteries and fuel cells occupy far more consumer facing niches than capacitors, these devices are nonetheless critical electronic components. Storing energy using an electric field, they have low energy density and are generally used for short-term energy storage. They make up for this in their enormous power density, having no reliance on slow chemical reactions. Capacitors are widely employed in signal processing, voltage smoothing, and other power conditioning applications and are essential for modern circuitry.[59]

Supercapacitors lie between batteries and conventional capacitors on the Ragone plot in Figure 1.3. They also share physical similarities to both, storing energy through either

charge separation, redox reactions, or some combination thereof. Supercapacitors are generally very robust, with long service lives and temperature stability compared to batteries. They find use in high power electronics applications, similar to capacitors, though fall short of the energy density of batteries. This limits their usefulness as a sole power source for vehicles and mobile electronics, though they may be used to relieve strain on batteries by providing limited-duration high power charging and discharging.[60]

1.3.1 Electrostatic Capacitors

Classically, capacitors are devices which store energy electrostatically, by charge separation. The prototypical capacitor consists of two conductive electrodes with an insulating medium separating them; this medium may be a vacuum if you prefer working with spherical cows but is more commonly a dielectric material. Polymer or ceramic dielectrics are often used, ideally with a high permittivity and high ionisation potential to increase the charge stored and operate at higher potentials, respectively.[61]

The simplest example is the parallel-plate capacitor, consisting of two parallel conductive plates separated by vacuum. The ideal capacitor, one defined only by its constant capacitance, C, stores an amount of charge, q, as outlined by the expression below:[62]

$$q = CV \tag{9}$$

Where V is the potential difference between the plates. The work done charging an ideal capacitor to a certain voltage is equal to the energy stored by that capacitor. Consider an

infinitesimal charge, dq, moving from one electrode to the other against a voltage, $\frac{q}{C}$, the infinitesimal work, dE required to move the charge will be:

$$dE = \frac{q}{C} dq \quad (10)$$

A general expression for energy stored in a capacitor can then be obtained by integrating from zero charge to a full charge, Q:[63]

$$E = \int_0^Q \frac{q}{C} dq \quad (11)$$

$$E = \frac{Q^2}{2C} \quad (12)$$

substituting CV for Q:

$$E = \frac{CV^2}{2} \quad (13)$$

1.3.2 Electrochemical Capacitors: Supercapacitors

Supercapacitors, ultracapacitors, or more properly, electrochemical capacitors, are a class of energy storage device that sits between the high energy density/low power density of batteries and the low energy density/high power density of conventional capacitors (see Figure 1.3). Structurally, they differ from traditional capacitors in that the electrodes are separated by an electrolyte as opposed to a dielectric medium. This electrolyte can in principle be any conductive solution, though organic electrolytes are most common due to their high decomposition voltages of around 3 V.[64]

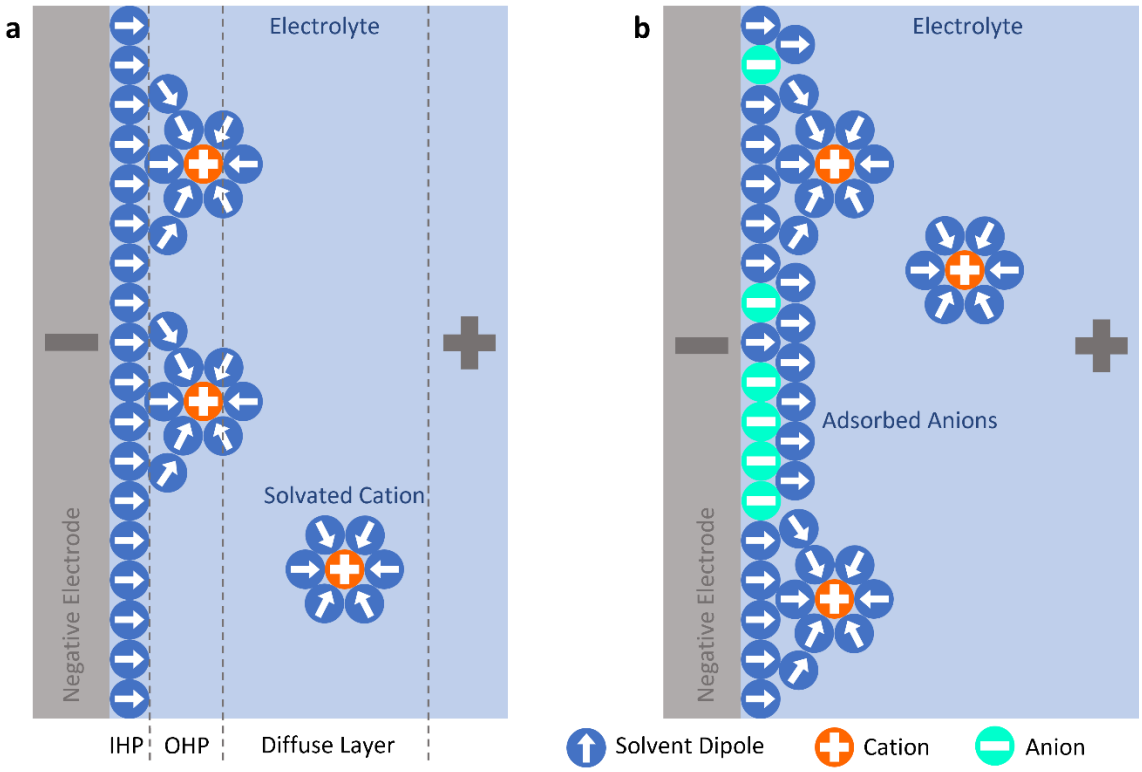

Figure 1.4: Diagram depicting the two principal charge-storage mechanisms in supercapacitors. a: EDLC, cations in solution are separated from anions in the anode by the IHP. b: pseudocapacitance, - in addition to the polarised solvent layer forming the IHP, adsorbed anions directly transfer charge to the anode. Inner and outer Helmholtz planes are denoted by IHP and OHP respectively

The Ragone plot in Figure 1.3 shows how supercapacitors bridge the gap in performance between electrostatic capacitors and batteries. As such, they are useful in applications which require high power for short periods of time,[64,65] having charge/discharge times typically in the range of 1-30 s. Charge is stored in supercapacitors *via* two principal mechanisms: electrostatic double layer capacitance (EDLC) and pseudocapacitance. EDLC is based upon charge separation and reversible adsorption of ions onto an electrode's surface. The applied potential between the electrodes creates a layer of polarised solvent molecules which adsorb onto the

electrode surface, forming the inner Helmholtz plane (IHP). Simultaneously, the electrode attracts counterions in electrolyte which diffuse towards it, forming the outer Helmholtz plane (OHP). This sets up the electrostatic double-layer for which the process is named and is illustrated in Figure 1.4a. The double-layer resembles a parallel-plate capacitor; the OHP acts akin to a counter electrode while the IHP with its polarised molecules behaves similarly to a dielectric. The very close spacing and hence charge separation between the electrode and OHP partially explains the high capacitance values seen in supercapacitors.

On the other hand, pseudocapacitance, seen in Figure 1.4b relies on rapid, reversible redox reactions at the electrode surface. These Faradaic charge transfers lead to direct, physical adsorption of redox ions onto the electrode. Electrons that are transferred occupy a valence orbital in either the redox ion or the electrode.[66] In contrast to batteries, the non-diffusion-controlled nature of these surface electron transfers leads to a build-up of charge that is linearly proportional to the potential applied between the two electrodes.[62]

The performance of a supercapacitor can be evaluated using three main techniques: cyclic voltammetry (CV), galvanostatic charge/discharge (GCD) and electrochemical impedance spectroscopy (EIS). These techniques will be elaborated on in Section 2.7.

1.4 Objectives

Overall, the goals of this thesis are on the development of novel energy storage devices, namely, supercapacitors, which are based on the MXene $Ti_3C_2T_x$. Emphasis is placed on both the synthesis and implementation of the MXene, in an effort to produce good quality material, and make best use of it. With this in mind, the production strategies for the supercapacitors, 3D aerosol jet printing and a 3D templating method both aim to improve the performance of these devices relative to more conventional architectures.

Chapter 3 concerns the synthesis and characterisation of the $Ti_3C_2T_x$ MXene and aims to produce high quality material suitable for energy storage applications. Furthermore, this work aims to improve both the yield and conductivity of the MXene by using a simple freeze-thaw assisted delamination process.

Chapter 4 aims to leverage the flexibility of 3D aerosol jet printing to produce $Ti_3C_2T_x$ microsupercapacitors which incorporate 3D electrode structures. It is hoped that the intrinsic performance of the 3D microsupercapacitor electrodes can be improved relative to more conventional 2D electrodes by overcoming the diffusional limitations of thick planar electrodes.

Chapter 5 targets supercapacitors of larger scale than Chapter 4, but similarly targets the improvement of performance using 3D structured electrodes. This chapter aims to produce 3D networked thin films of MXene, formed on the surface of a sacrificial ZnO template. The electrochemical performance of these networks will be evaluated, and their micro- and nanostructure tuned to produce high performance supercapacitor electrodes.

2 DEPOSITION AND CHARACTERISATION TECHNIQUES

This chapter outlines the operating principles of the most important deposition and characterisation methods used in this work.

2.1 Additive Manufacturing

Additive manufacturing (AM), also known as 3D printing, is the process of creating objects using layer-by-layer deposition according to a digital model. It represents a paradigm shift in the way we manufacture and design products, as it allows for greater customization, faster prototyping, and the ability to create single part complex geometries that would be difficult or impossible to achieve using traditional manufacturing techniques. Furthermore, in traditional manufacturing processes, objects are typically created by cutting or shaping stock materials (subtractive manufacturing), which in addition to often being time consuming has significantly higher waste generation, which may or may not be able to be recycled and reincorporated into earlier stages of the manufacturing process. The ability to produce customised parts on-

demand, without the need for highly specialised and expensive tooling, has led to the creation of new business models. With on-demand production enabled by AM, companies can produce small batches of niche products as they are ordered. This has the potential to greatly reduce waste and improve supply chain efficiency. It's therefore quite easy to see how AM can impact society at large, having the potential to revolutionise production and consumption of goods. By reducing the need for large-scale manufacturing facilities, it has the potential to greatly improve access to specialised products, particularly in remote areas lacking the robust supply chain needed to support mass manufacturing and distribution. In a sense, this would democratise manufacturing, allowing small businesses or even individuals to produce items locally rather than relying on huge facilities and global supply chains. With any luck, this will lead to a shift towards more localised, sustainable, and resilient manufacturing.

AM encompasses many techniques, notably inkjet printing (IJP), fused deposition modelling (FDM), stereolithography (SLA), and selective laser sintering (SLS). A further technique, aerosol jet printing (AJP) will be covered in detail in Section 2.2. Each method has its own set of capabilities and limitations and is suited to different materials and applications. IJP uses a print head to deposit a liquid or powdered material onto a substrate layer-by-layer. Each layer is dried, cured, or sintered after deposition build up the object. Inkjet printing is a relatively low-cost and simple method of additive manufacturing, and it is well suited to producing small parts or structures with high resolution and fine details. The technique that most people associate with 3D printing is FDM, which extrudes a filament of plastic or other high viscosity through a nozzle to create the constituent layers of the object. FDM and is well suited to polymer printing at a high level of detail, and its ubiquity means that both printers and feedstock

are quite affordable. SLA relies on a laser to selectively cure a photopolymer layer-by-layer. Offering generally much higher resolution than FDM, SLA is suitable for producing parts with fine details, though the selection of feedstock is generally more limited and expensive. Using SLS, powdered materials can be printed, using a laser to sinter each layer. The laser rapidly fuses the powder (often metals such as steel or titanium) into a solid and is widely used in boutique manufacturing for its ability to realise high quality metal parts with geometries that cannot be achieved using machining.

The variety of AM techniques enables an even larger variety of materials to be printed, including, but not limited to, plastics, metals, ceramics, and even biomaterials. With this breadth of capability, AM isn't limited to manufacturing of "dumb" components. In the healthcare sector, it is being used to produce custom prosthetics, implants, and other medical devices. The creation of personalised medical devices that are tailored to fit an individual's specific needs can improve patient outcomes and reduce costs. Pertinent to this work, AM is leveraged in the energy storage sector, being used to produce batteries, supercapacitors, fuel cells, or components thereof. For example, 3D printing may be used to produce customised electrodes for batteries and supercapacitors, or to create complex fuel cell structures to improve efficiency and performance. High resolution techniques like IJP enable smaller scale energy storage devices, such as microbatteries and microsupercapacitors, which could even be integrated into the structure of portable electronic devices or wearables.

2.2 Aerosol Jet Printing

An emerging technology in additive manufacturing, aerosol jet printing (AJP) is a method for direct writing of functional inks onto a wide range of substrate materials and geometries.[67] It appeared in the literature in the early 2000s,[68,69] having been developed through the Defense Advanced Research Projects Agency (DARPA) Mesoscale Integrated Conformal Electronics (MICE) project,[70] which focussed on the creation of material- and substrate-agnostic printing techniques. Briefly, the AJP process begins with the "atomisation" of a chosen ink into an aerosol of fine particles, colloidally suspended in a carrier gas, typically nitrogen or argon. The carrier gas drives the aerosol to a deposition head where a secondary sheath gas aerodynamically focuses the aerosol into a collimated beam which then impinges upon the substrate. This process confers significant advantages over more established printing techniques such as inkjet printing (IJP), most notably the ability to pattern over complex topologies [71] and fewer constraints in terms of ink composition or viscosity, as in principle, any material that can be suspended in an aerosol may be deposited using AJP.[72] Deposition of conductive inks containing silver nanoparticles,[73–76] graphene,[76–78] or carbon nanotubes (CNTs)[79–83] have been widely reported, but examples extend to cover polymers,[84–86] ceramics,[87,88] proteins,[89–91] and a range of functional nanomaterials including transition metal dichalcogenides (TMDs) [92,93] and perovskites.[94,95] Reflecting this distribution, AJP research to date has largely centred around printed circuits and transistors,[81–83,96,97] however its wide material compatibility has increasingly led to AJP being investigated for emerging technologies in printed electronics. These include energy storage devices,[98–100] millimetre wave and terahertz communications;[101–104] physical,[105,106]

chemical,[107] and biological [108–112] sensing; high-energy photodetection;[95,113] and photovoltaics.[86,114,115] While AJP's material agnosticism is largely conferred by the aerosolisation of the functional ink, the jetting of the aerosol ink affords the user a measure of freedom from the geometric constraints associated with traditional direct write methods. The large substrate-nozzle separation (standoff distance) of around 2 – 5 mm [116] means surface irregularities may be ignored, and the focused jet can realise feature sizes as small as 10 μm.[117] Additionally, due to the jetting of material, AJP can be treated as a 2.5-dimensional (2.5D)[71,118] or even 3-dimensional (3D)[95,102,108,110,119] direct write technique, and has been used to create self-supporting 3D features[120–122] which would be difficult or impossible to produce though IJP.

2.2.1 Principles of Aerosol Jet Printing

While the core operating principles of this elaborate rattle can are straightforward, the interaction of many rheological, aerodynamic, and morphological effects begs a more robust understanding of the process. Indeed, the viscosity, surface tension, and vapor pressure of the solvent, as well as the size and density of any dispersed solids, will impact the quality of the aerosol generated.[72] In an ideal case, the aerosol would be of high density, monodisperse and all droplets would have sufficient inertia to be deposited on the substrate. Large or slow droplets can settle before exiting the nozzle and lead to flow restrictions and clogging.[67,123] Unfortunately, a convenient summary of parameters which determine an ink's suitability for AJP like the Z number [124] for IJP does not yet exist, but it is generally accepted that viscosities in the range of 1 – 1000 cP will be at a bare minimum, technically printable.[98,125]

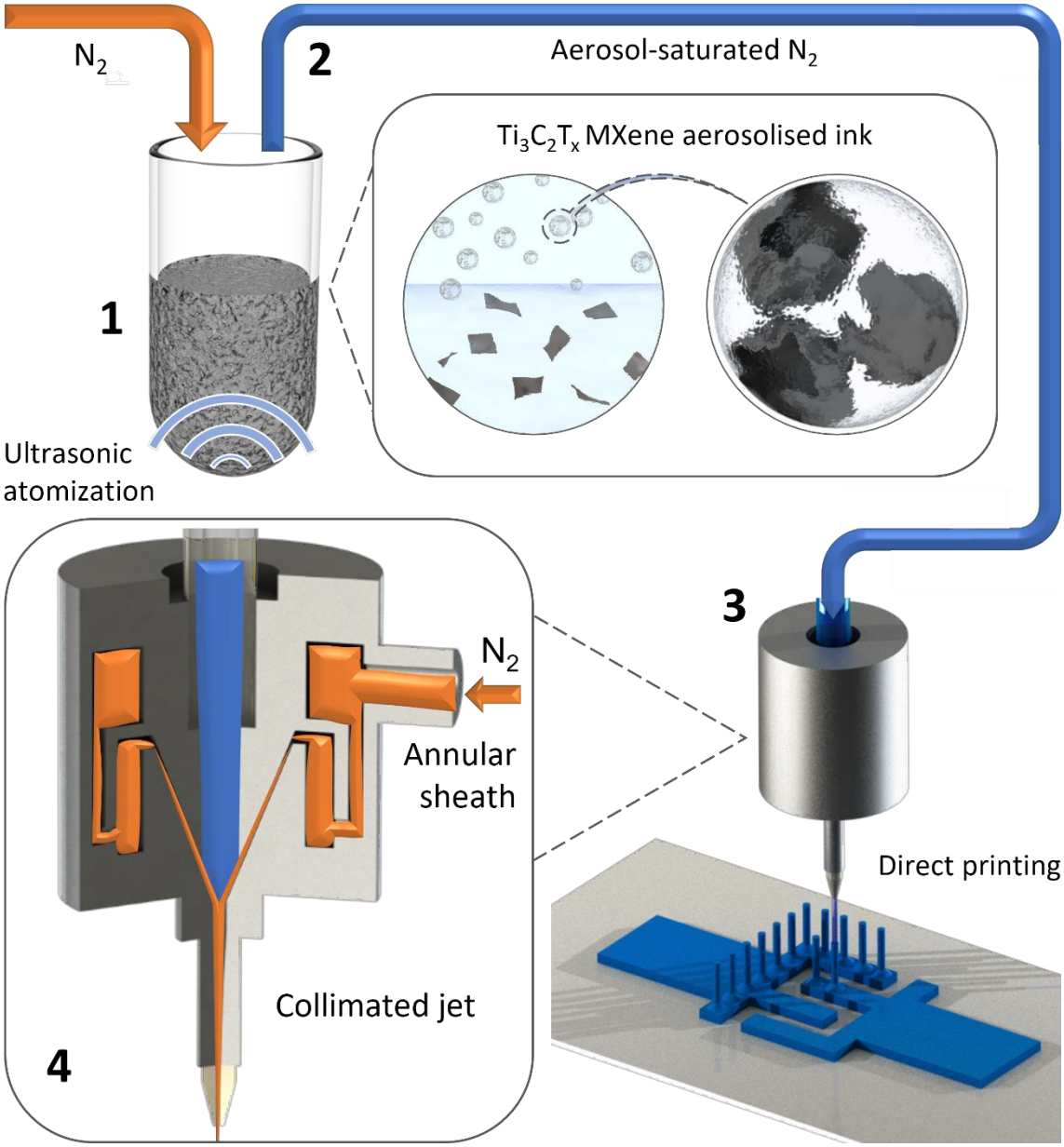

Figure 2.1: Schematic of the Aerosol Jet Printing process. 1: Formation of the aerosol via ultrasonic atomisation. 2: Transport to the print head. 3: Arrival at print head and direct printing of 2D and 3D features. 4: Cutaway view of the print head, showing the channels which guide the annular sheath flow, focusing the aerosol into a collimated jet for printing.

Aerosolisation is generally achieved through either ultrasonic or pneumatic atomisation, with the latter able to handle high viscosity (up to 1000 cP) inks at the expense of

producing a more polydisperse aerosol.[72] This means that pneumatically generated aerosols require additional refinement downstream of the atomiser, using a virtual impactor to remove low-inertia droplets from the stream.[125]

A diagrammatic representation of the Optomec Aerosol Jet system used in this work is presented in Figure 2.1. As high viscosity solvents are not required in our case, the process begins by generating an aerosol of functional ink using the ultrasonic atomiser. This process is intended for relatively low viscosity inks, up to c. 20 cP,[126] and small volumes, in the range of 0.5 – 3 ml. An ultrasonic transducer is immersed in a temperature-controlled bath of distilled water and is driven at a frequency of c. 1.7 MHz,[127] generating pressure waves which are coupled to the vial of ink through the distilled water. The resultant capillary waves at the phase boundary of the ink form a faraday excitation of sufficient amplitude to shed droplets from the surface.[128] The effectiveness of this process as determined by the ejection rate and mean droplet diameter are strongly dependent on the rheological properties of the ink.[129] However, the physics governing the critical driving amplitude at which the faraday excitation becomes unstable, reaching the ejection threshold, and the physics governing the diameter of the ejected droplet are quite different, resulting in divergent behaviour. Both phenomena undergo an inviscid-viscous transition above a certain dimensionless frequency, Ω,[130] but this frequency is on the order of 10^4 times greater in the case of droplet diameter.[131] Ω is given by the following formula:

$$\Omega = \omega\left(\frac{v^3\rho^2}{\gamma^2}\right) \quad (14)$$

Where ω is the driving frequency, υ is the viscosity, ρ is the density and γ is the surface tension. It has been established that for water, the transition to the regime dominated by viscous damping of the amplitude occurs at Ω corresponding to $\omega = 27$ Hz.[132] This dependence on viscosity can be used to rationalise the unsuitability of ultrasonic atomisation for aerosolising highly viscous inks. The critical acceleration, a_c, that is the peak acceleration corresponding to the critical amplitude, can be used to calculate the critical power, P_c, required for aerosolisation.[130,133] This figure is noteworthy as it also determines the rate of droplet generation.[130] Taking $P = Fv$, $F = ma$, and $v = \frac{a}{\omega}$, where P is the applied power, F is the force applied to the liquid, v is the velocity of the wave, m is the mass of the liquid and a is the peak acceleration of the wave, we can express P_c as a function of υ and ω:

$$P_c = \frac{m{a_c}^2}{\omega} = mv\omega^2 \quad (15)$$

Thus, for our fixed 1.7 MHz driving frequency, the minimum power required to eject droplets from the ink surface scales linearly with the viscosity of the ink.

Conversely, as early as 1962 it has been known that the diameter of the ejected droplets even at driving frequencies approaching the MHz range is independent of viscosity and depends strongly on the surface tension of the ink.[134] This behaviour was able to be modelled by assuming a linear relationship between the wavelength of the ultrasonically generated capillary waves and the diameter of the resultant droplets. The wavelength, λ, of the capillary waves is given by the Kelvin equation,[135] calculated using the depth, h, capillary wave frequency, f, density and surface tension:

$$\lambda(tanh\frac{2\pi h}{\lambda})^{-\frac{1}{3}} = (\frac{2\pi\gamma}{\rho f^2})^{\frac{1}{3}} \quad (16)$$

In our case, as the depth of ink is on the order of several mm, $\frac{2\pi h}{\lambda} \gg 1$. Thus, we can take $\tanh\frac{2\pi h}{\lambda} = 1$. Furthermore, for ultrasonically driven capillary waves, the frequency of the standing waves is half the driving frequency,[136] such that $f = \frac{\omega}{2}$. In terms of ω, this gives us:

$$\lambda = (\frac{8\pi\gamma}{\rho\omega^2})^{\frac{1}{3}} \quad (17)$$

The average diameter of the produced droplets, D_{50}, was found to be proportional to the capillary wavelength such that:

$$D_{50} = a\lambda = a(\frac{8\pi\gamma}{\rho\omega^2})^{\frac{1}{3}} \quad (18)$$

Where a is a constant, first experimentally measured in 1962 as 0.34,[134] and more recent studies have closely agreed with this figure, with 0.35 ± 0.03 reported in 2004.[131] In stark contrast to Equation (15), we can see that D_{50} is independent of ν. Accordingly, where exactly an ink lies within the acceptable range of ν for aerosol formation has little bearing on the final print quality, which is strongly affected by droplet diameter.[137] For our case, using a driving frequency of 1.7 MHz, assuming a water-based ink with low concentration, using a value of 0.72 mN/m for σ[138] and 997 kg/m^3 for ρ[139] gives a value of D_{50} c. 2.95 µm. This is comfortably within the c. 1 – 5 µm range typical for the Optomec AJ 300 system used.[140] Being able to decouple the ν contribution makes formulating a printable ink that much simpler than in IJP, where printability, as determined by the Z number, is dependent on droplet diameter, D, γ, ρ, and ν:

$$Z = \frac{\sqrt{\gamma \rho D}}{\nu} \quad (19)$$

These frequently co-dependent parameters mean that achieving a printable ink within the acceptable range of $\sim 4 < Z < \sim 14$ [124] can be challenging.

Referring again to Figure 2.1 a flow of N_2 is used as a carrier gas to drive the generated aerosol from the vial through a polytetrafluoroethylene (PTFE) mist tube towards the print head. This gas flow can lead to significant changes in the aerosol composition, as the micron-scale droplets have evaporation times on the order of microseconds in a dry atmosphere.[141] Premature drying of the droplets may lead to an increase in the apparent deposition rate, and in inks whose viscosity is close to the limit for ultrasonic atomisation, can confoundingly lead to decreased deposition rate as the concentration of the ink increases.[142] To mitigate these issues, the carrier gas should be passed through a bubbler to pre-saturate with solvent before entering the vial. As the aerosol is carried through the mist tube, a further source of process drift is encountered, in the form of transport losses. These losses predominantly affect the largest and smallest droplets in the stream, where the former are lost through gravitational settling and the latter through diffusion.[67] While gravitational loss of large droplets is intuitive if you have ever been caught in the rain, diffusional loss is explained by considering the random Brownian motion of droplets near the walls of the mist tube.[143] Droplets within a mean square diffusion length of the walls may impinge on the surface and be removed from the stream, should they be adsorbed. Though these loss mechanisms reduce the overall transport efficiency of the aerosol stream, they act as somewhat useful low and high pass filters for droplet size. Both gravitational[144] and diffusional losses[145] have long

been established as dependent on the size and velocity of the droplets, in addition to the tube length. Thus, the carrier gas flow rate can be used as a primitive dial to adjust these filtering effects, with low flow rates (and hence, velocities) resulting in a smaller proportion of both the largest and smallest droplets arriving at the print head, narrowing the size distribution of the printed droplets. This also results in a non-linear scaling of deposition rate with carrier gas flow rate, low values of which reduce both the overall transport efficiency and the maximum print time.

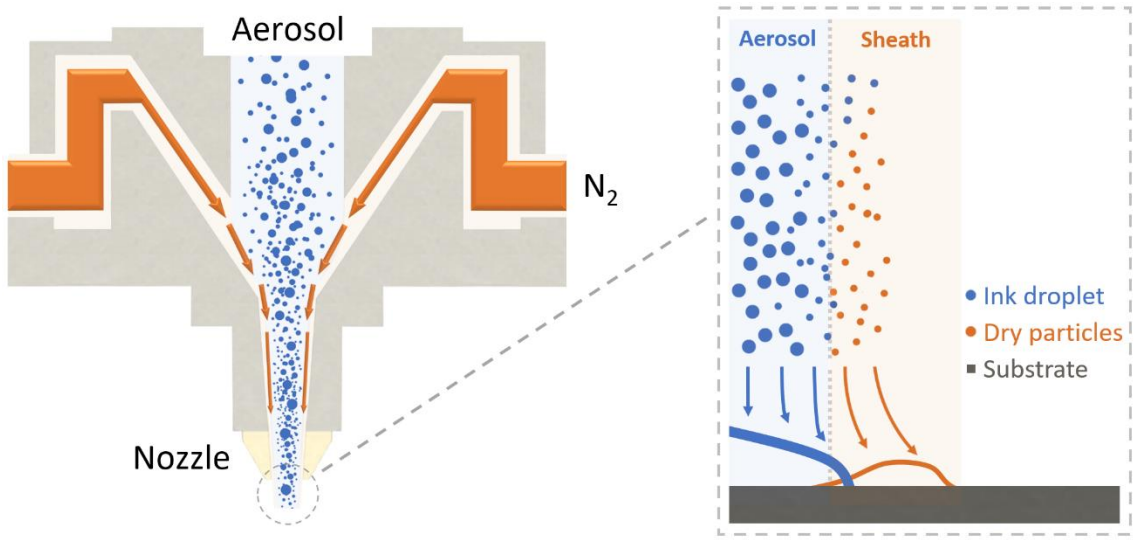

Figure 2.2: Cross-section of print head, showing focusing of the aerosol stream into a collimated jet. Detail view shows a representation of the outer edge of the aerosol jet in-flight and impinging on the substrate.

Though the filtering effect can improve print consistency to an extent, droplets lost in transport are not removed from the system entirely and coalesce into macroscopic drops in the mist tube given enough time. Drops of a sufficiently large size to constrict the aerosol flow tend to be catapulted towards the print head, ruining any pattern unfortunate enough to be caught in their path and necessitating a clean out of the print head and nozzle. With the reduced transport losses associated with high carrier gas

flows, one can expect to deposit a greater mass before condensation in the tube becomes an issue. Nonetheless, the operator must monitor the build-up and periodically purge the tube to minimise the risk to already printed structures.

Once at the print head, the aerosol stream encounters a secondary N_2 flow, emanating from an annular channel circumscribing it. This is referred to as the sheath gas, and it serves to accelerate and focus the aerosol, functioning as a virtual nozzle working in concert with the ceramic nozzle through which the aerosol jet finally exits. A cross section of this process can be seen in Figure 2.2. More rigorously, as it enters the print head, the aerosol is focused and accelerated slightly by a constriction just upstream of the transition region, where the sheath gas is injected around the stream. Here, the sheath gas focuses the aerosol a second time as it forms a boundary layer wrapping the aerosol. This collimates the aerosol by volume displacement and accelerates it further,[125] but additionally serves to prevent contact between the aerosol and the walls of the channel. This prevents deposition of material or condensation of solvent on the surface which could disturb the laminar flow of the sheath gas or lead to clogging if left unchecked.[146] This also reduces the cleaning requirements for the print head which is a blessing considering the complex geometry of the part and its very tight tolerances. Downstream of the transition region, the aerosol is focused a third time as the channel constricts gradually, exiting through a sub-millimetre diameter nozzle, which may be as narrow as 50 µm. The aerosol jet as it emerges will have been focused to a diameter approximately 10% - 20% that of the nozzle,[146,147] and accelerated to a velocity on the order of 100 ms^{-1}.[137,146] In general, the diameter of the aerosol jet, D_J, is controlled by the sheath gas flow rate, the beam tightening and accelerating with higher sheath flows.

This does not scale *ad infinitum*, as a transition to turbulent flow would disperse the jet, and intuitively, a velocity of ~340 ms^{-1} forms a hard limit as the combined beam and sheath velocity cannot exceed the speed of sound. An estimate of D_J can be obtained using the focusing ratio, FR,[73,148] the ratio of sheath to carrier gas flow rates:

$$FR = \frac{F_S}{F_C} \tag{20}$$

Where F_S is the sheath gas flow rate and F_C is the carrier gas flow rate, both reported in standard cubic centimetres per minute (SCCM), 1 SCCM being equal to 1 cm^3/min at standard temperature and pressure (STP). The relationship between FR and D_J is then given by:[125]

$$D_J = D_N \sqrt{1 - \sqrt{\frac{FR}{1 + FR}}} \tag{21}$$

Where D_N is the nozzle diameter. This formula, being independent of droplet diameter, is agnostic of ink formulation and only weakly dependent on F_C,[146] large values of which will broaden the distribution of droplets as discussed. This relationship is a useful guide; however, the final resolution of printed features cannot be wholly explained by the focusing achieved within the confines of the print head. In addition to nonideal behaviours such as turbulence, axial asymmetry and premature drying, there is some evidence that the aerosol jet is subject to a small amount of positive aerodynamic lensing effects while in-flight.[149,150] Low inertia particles suspended in polydisperse jets have long been observed to follow gas flow streamlines, confining higher inertia particles to a narrow central region.[67,151] The dimensionless Stokes number, Stk quantifies this effect. Moreover, the Stokes number indicates if a droplet in the jet will

eventually impact the substrate.[125] Low Stokes number particles ($Stk \ll 1$) are advected by the flow, tracing the path of the fluid streamlines, while the paths of high Stokes number particles ($Stk \gg 1$) are inertially determined, detaching in response to changes in direction or velocity of the flow.[152] Stk can be determined for a given droplet using the following expression:[153]

$$Stk = \frac{\rho C_C D V}{4.5 {\upsilon_G}^2 D_N} \quad (22)$$

Where C_C is the slip correction factor, V is the droplet velocity, and υ_G is the viscosity of the surrounding gas. On average, the Stokes number for the droplets increases dramatically going from the transition region (low V, high D_N) to the nozzle exit (high V, low D_N). This facilitates the initial collimation upon injection of the sheath gas, with the droplets adhering to the direction of the flow, as well as the final deposition of the droplets, where they predominantly separate from the flow and impinge as a tight beam as the gas disperses laterally across the substrate.

To reliably achieve a well-focused jet, as well as the desired printed line profile, the focusing ratio, outlined in Equation (20) may be used as a guide when setting printing parameters. Though the deposition rate of ink on the substrate is predominantly controlled with F_C, while D_J and V are predominantly controlled with F_S, there is clearly an interaction between the two flows in the print head. The corresponding influence on the internal pressure associated with each has meant it has proved quite useful to consider the two parameters together. In general, the width of a printed line can be expected to decrease when FR is increased, along with an increase in thickness, and it is generally accepted that $\mathrm{FR} = 2$ is a sensible ratio that works in most cases.[73]

However, this scaling assumes that all of the ink is deposited on the surface, and it has been shown that at higher focusing ratios the thickness of a line may actually decrease. This is despite the amount of ink exiting the nozzle remaining the same.[154] The non-ideal behaviour of the jet can explain this phenomenon and is represented in the detail view of Figure 2.2, showing the profile of the outer edge of the jet both in-flight and impacting the substrate. Here, we can see a spatial and temporal variance in droplet size distribution brought on by drying of the outermost droplets while in-flight.[154] Dry particles with sufficient velocity may even rebound from the substrate entirely, reducing the effective deposition rate and explaining the inability for FR to predict deposition profile entirely. In any case, substantial evaporation of solvent from the droplets in-flight can reduce the Stokes number below the value required for impaction, leading to deposition further off-axis and being a source of "overspray" or the deposition of satellite particles that reduce the resolution of the final print, should they adhere to the substrate on impact. High volatility solvents will be especially prone to drying effects, though this may be mitigated in part through ink composition, using a fraction of low volatility cosolvent, for example 10% V/V terpinol in chloroform.[155]

Impaction and aerosol-substrate interaction are the final physical processes that need to be taken into consideration when utilizing AJP. Broadly speaking, high Stokes number droplets will impact close to the central axis, as is desirable. The lowest Stokes number droplets/particles we expect to fail to impact the surface at all,[156] being carried far from the central axis and dropping out of suspension or becoming airborne when the flow has diffused sufficiently. This can give the user very tight focusing but has implications for the overall efficiency of the process, and even presents potential health concerns. Users should be aware of these trade-offs, especially in industrial settings with a large

throughput of ink, or in cases where the functional material is itself, hazardous. Finally, droplets or particles close but below the critical Stokes number required for direct impaction will be deposited off centre and cause the ubiquitous AJP overspray, as in the case of the dry particles in Figure 2.2, and is a driving factor in ink composition. This overspray also occurs with especially small and/or slow droplets, even in the absence of drying effects, and sets minimum F_S values in practice. Moreover, how "wet" or "dry" the aerosol is upon impact will also have significant influence on the overall aerosol-substrate interaction and final morphology of the printed features. Much of this interaction will be governed by the ink's wetting characteristics on the substrate and as with IJP [157] or other direct write techniques, must be acknowledged for best results. Viscous forces in a droplet on impact will dissipate some if its kinetic energy, while the remainder becomes surface energy. The droplet then spreads to a diameter determined by the relative surface energies of the ink and substrate.[158] Good adhesion and line consistency needs good matching of the surface tension of the ink and surface energy of the substrate.[159] In general, it can be expected that a wet, well spreading ink will flow, filling voids and resulting in a compacted, low porosity film. This is desirable in many cases, as is a high deposition rate, especially in industrial processes where throughput is an important concern. However, excessive solvent can introduce cracks during drying,[154] and a high deposition rate may cause enough wet ink to coalesce on the surface, resulting in uneven lines and line profiles.[67] More catastrophically, the high-pressure gas from the jet can send erratic flows of fluid ink over the substrate like rain on an aeroplane window. High print speed can be used to reduce the effective deposition rate per unit area of the substrate; however, this may introduce its own irregularities,[160] vibrations due to abrupt changes in direction, or at worst the stage can

reach an acceleration limit, which halts the printing process entirely. Avoiding designs containing sharp corners or fill patterns with back-and-forth rasterization minimises the acceleration the stage will experience. Considering the potential pitfalls of overly wet deposition, uniform, partial drying of droplets in-flight has been found to be beneficial.[154] More drying may result in a more porous or granular structure,[67] especially in the case of solid suspension inks, though in cases where a high surface area is desirable, this may be a benefit.

The above outlines the myriad interactions and parameters that influence the AJP process, and perhaps explains the absence of a unified framework determining the overall printability of arbitrary inks. AJP therefore relies on a significant amount of user experience, empirical measurements, and trial-and-error to make good use of its capabilities. When properly leveraged though, AJP boasts rapid, high-resolution printing and unmatched flexibility in ink composition, substrate material, and substrate geometry.

2.3 Critical Point Drying

Critical point drying (CPD), also known as supercritical drying, is a process used to dry delicate samples while preserving their structure. A sample is first placed in a high-pressure vessel filled with a liquid solvent, usually CO_2. The pressure and temperature are then increased until the solvent reaches its critical point, i.e., temperatures and pressures above 304 K and 7.38 MPa, respectively.[161] The solvent then becomes a supercritical fluid, which has properties of both a gas and a liquid. The supercritical CO_2 is able to penetrate the pores and voids within the sample, displacing any liquid

inside. The pressure and temperature are then reduced, causing the supercritical fluid to return to a gaseous state, leaving a dry sample.[162]

Unlike other drying methods, such as freeze-drying, CPD does not cause shrinkage or damage to the internal structure of the sample. In conventional drying, surface tension between the evaporating liquid and the surrounding air pulls on any solid surfaces in the sample, which can lead to fracturing or collapse. Freeze-drying has expansion associated with the phase transition from water to ice, and this can also lead to deformation or damage. By using a supercritical fluid, the liquid and gas phases become indistinguishable, leading to a homogenous drying environment.[163]

2.4 Microscopy

Since the Middle Ages, optical lenses have been used to magnify objects too minute to be resolved in detail with the human eye. Developing from the lenses used for spectacles and magnifying glasses, optical microscopes resembling those we use to this day first appeared in the 17th century.[164] The limits of optical microscopes' resolving power were established by Ernst Abbe in the late 19th century, who proposed the diffraction limited resolution as defined by the following expression:[165]

$$d = \frac{\lambda}{2sin\,\theta} \quad (23)$$

Where d is the resolution, λ is the wavelength of light being focused, and θ is the half aperture angle. This was firmly proven as a fundamental limitation of optical microscopes by Helmholtz, with a resolution not less than 200 nm being the best possible using visible light.[166] Even still, this does not consider the effect of optical

aberrations, lens defects, or vibrations, which limit the maximum practicable resolution further. While sufficient for many applications, a resolution in the low hundreds of nanometres occludes the structure of nanoscale materials from optical microscopy.

2.4.1 Electron Microscopy

The solution to this optical diffraction limit presented itself in the early 20th century when De Broglie hypothesised a wave nature of matter.[167] The wavelength of these De Broglie waves could be calculated with an expression derived from Einstein's mass-energy relation and Planck's energy-frequency relation. These relations are as follows:

$$E = mc^2 \tag{24}$$

$$E = hf \tag{25}$$

Where E is energy, m is mass, c is the speed of light, h is Plank's constant, and f is frequency. To generalise for an arbitrary particle of velocity, v, and De Broglie wavelength, λ, v is substituted for c, and $\frac{v}{\lambda}$ for f, giving:

$$mv^2 = \frac{hv}{\lambda} \tag{26}$$

$$\lambda = \frac{h}{mv} \tag{27}$$

Which is to say, that a particle's wavelength is determined solely by Plank's constant and its momentum, mv. If we then consider an electron accelerated by a voltage of as little as 1 kV, using Equation (27) and Equation (23) we arrive at a wavelength of 38.7 pm, and a diffraction limited resolution of 19.35 pm, assuming a half aperture

angle of 90°. This is an order of magnitude smaller than the length of most atomic bonds and so the potential resolving power of an electron-based microscope becomes clear. Unfortunately, reaching this diffraction limited resolution is impossible in practice, not least because aperture half angles rarely exceed 80°.[168] Lens aberrations, for example chromatic aberration due to the difficulty in achieving a monochromatic electron beam; vibrations, now of even greater concern due to thermal vibration of the atoms at this scale; and beam damage at high acceleration voltages mean that the real-world resolving power is much lower than the theoretical limit for the matter wave being used. Despite these nonidealities, it can be expected that even rudimentary electron microscopes will outmatch the resolution of the most advanced optical microscopes.[169]

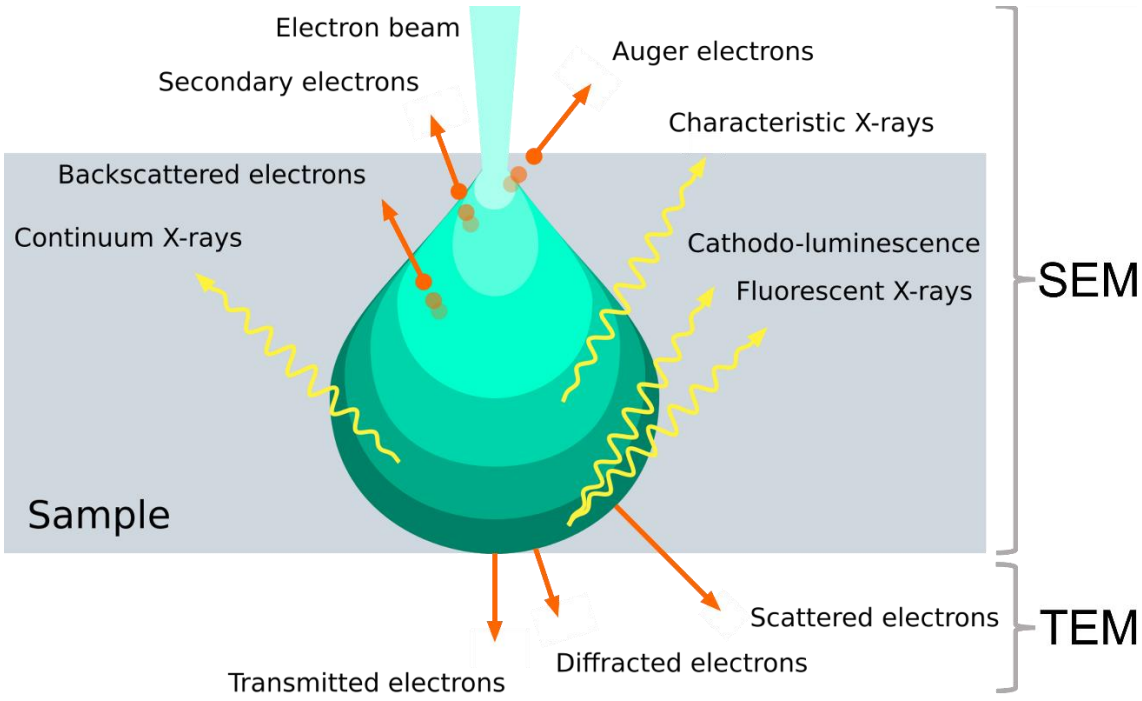

Figure 2.3: Illustration of an electron beam-sample interaction. Major scattering and photon emission types are shown for both the SEM and TEM operating regimes.

Forming an image using electrons in principle only requires pointing an electron gun at your sample and recording the position of the electrons as they strike a detector. In reality, many signals are generated and carry distinct information. In Figure 2.3, a cross-section of an electron beam interacting with a sample is shown. The teal area shows the pear-shaped extinction volume, and the relative depth at which signals emanate. As indicated, signals which emerge in the direction of the beam (transmitted, diffracted, and scattered electrons) are the domain of transmission electron microscopy (TEM) and those emerging against the direction of the beam (secondary elections, X-rays, etc.) are the domain of scanning electron microscopy (SEM). These signals will be discussed in more detail in later sections.

2.4.2 Transmission Electron Microscopy

Despite SEM being the more ubiquitous technique nowadays, electron microscopy began with TEM in 1931, developed by Knoll and Ruska.[170] TEM uses a beam of high-energy electrons, in the range of 50 – 300 keV, which can pass through thin samples of around 100 nm or less. Electrons passing though the sample can undergo many different interactions and scattering events, see Figure 2.3. Forward-scattered electrons are used to form the image in TEM, though the backward ejection of secondary electrons prompts the emission of characteristic X-rays which can be used for elemental analysis using energy dispersive X-ray spectroscopy (EDX), more details in Section 2.5.3. Inelastic forward-scattering events also lead to characteristic energy losses for the electrons, which may be analysed using electron energy loss spectroscopy (EELS),

detailed in Section 2.5.4. The typical positions for EDX and EELS detectors in a TEM column are shown in Figure 2.4a.

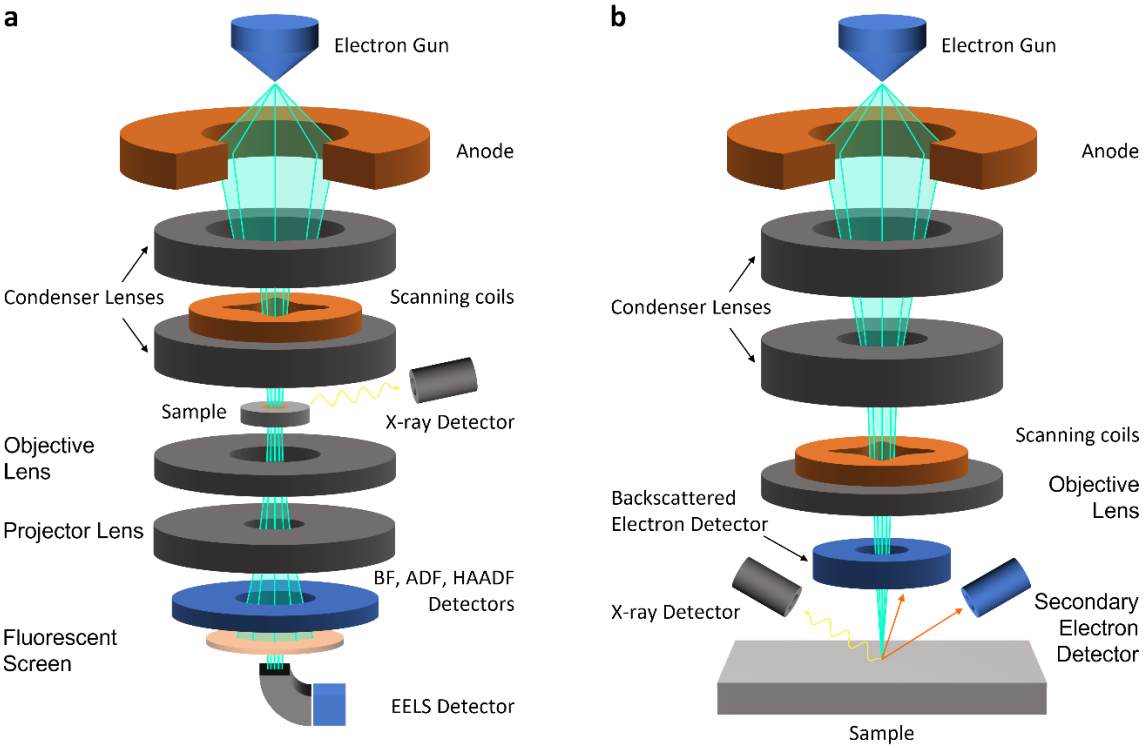

Figure 2.4: Schematic showing typical configurations for scanning and transmission electron microscopes. (a) TEM column, where the primary detectors lie below an electron-transparent sample. (b) SEM column, where the detectors lie above the sample.

A TEM column (Figure 2.4a) broadly consists of the illumination system, sample stage and imaging system. The illumination system houses the electron gun, anode, and condenser lenses. Depending on the resolution the microscope is designed for, different electron sources may be used. For lower resolution 'workhorse' TEM, a thermionic emitter is used, often LaB_6, while for atomic-resolution or other high-resolution imaging, a field emission gun (FEG), either Schottky or cold-cathode is used.[171] The emitted electrons pass through a set of condenser lenses, forming a focused beam. These

lenses determine the area of the sample that is illuminated, the overall intensity, and the operating mode.[172] There are two primary operating modes in TEM. Conventional TEM (cTEM) uses a parallel, static beam, whereas scanning TEM (STEM) uses a tightly converged beam which is rastered over the sample using scanning coils.

The sample stage may be inserted and withdrawn from the microscope, and holds the specimen steady, any vibrations being disastrous for image clarity. In terms of sample preparation, dilute dispersions of nanomaterials can be drop-cast on a TEM grid, usually a fine copper mesh with a thin, porous carbon underlayer to support the material while remaining electron transparent. Of course, electron transparency is key, so samples are usually limited to around 100 nm thick, though low atomic number, Z, atoms have a significantly lower scattering cross-section and may allow for imaging of thicker specimens.[173] Transparency will also increase as electron energy increases, so high accelerating voltages may be used, though this can result in beam damage from dislocations or chemical reactions.[174] Above the sample stage an X-ray detector for EDX is often mounted, allowing for elemental analysis, further details in Section 2.5.3.

The transmitted electrons are then focused and collected in the imaging system. Image formation and magnification are handled by a set of objective and projector lenses below the sample stage. In cTEM, bright field (BF) and dark field (DF) images may be formed. BF imaging uses the direct beam, comprised of transmitted electrons, whereas DF imaging uses the higher angle scattered (Rutherford scattering) and diffracted (Bragg scattering) electrons, see Figure 2.3.[175] Mass and thickness strongly influence the amount of scattering, giving rise to contrast in the image. Regions of low thickness or atomic number therefore appear bright in BF imaging, and dark in DF imaging. In

STEM, images are formed using three detectors, the BF, annular DF (ADF) and high angle annular DF (HAADF). A key advantage of STEM is strong Z-contrast derived from the scattering angle of the beam. Using a HAADF detector, a DF image is formed such that bright regions correspond to high atomic number atoms. The ADF detector mixes Z-contrast with diffraction contrast and can reveal dislocations or regions where the lattice is under strain.[176] BF images in STEM are comprised of low angle scattered electrons and as such can be used to image lighter elements. These inelastically scattered low angle electrons are also used for EELS analysis, see Section 2.5.4.

2.4.3 Scanning Electron Microscopy

In 1942, a decade after the debut of TEM, Zworykin developed the first SEM, using secondary electrons to achieve topographic contrast. This new microscope configuration had excellent surface sensitivity, but its resolution of 50 nm was low compared to TEM, leading to a lukewarm reception from the already established TEM community.[177] Thankfully, the appeal of the technique was not lost on some, and SEM's ability to extract 3D information from surfaces over a range of length scales from millimetres to microns led to its continued development.[178] At present, SEMs and attached EDX detectors are invaluable tools and it is truly difficult to find practice-oriented fields in physics, chemistry, biology or engineering for which they don't have some usefulness.

As can be seen in Figure 2.4b, the illumination system of an SEM is broadly very similar to that of a TEM, though SEM generally operates at far lower acceleration voltages, of between 0.1 and 30 keV.[179] Like STEM, the beam is formed into a convergent probe and rastered over the surface using the scanning coils. The spatially

varying intensity from the beam-sample interaction is then mapped using one of the detectors to form an image. The beam generates primarily secondary electrons (SE), Auger electrons (AE), and backscattered electrons (BSE), as well as the continuum and characteristic X-rays associated with SE emission, illustrated in Figure 2.3. The imaging system is, naturally, located above the sample stage, and generally comprises SE detectors, BSE detector and EDX detector, pictured in Figure 2.4b. SE emissions are the primary signals used for imaging in SEM, using the in-lens and lateral SE detector. Inelastic collisions between the beam's electrons ionise atoms in the sample, generating SEs. The in-lens detector records primarily SE1 electrons, which are SEs generated directly by beam-sample interactions. SEs generated by BSEs are referred to as SE2 electrons and are recorded by the lateral SE detector. In both cases, but especially the latter, these SEs are of very low energy, generally < 50 eV, making them extremely prone to scattering.[180] This, coupled with the sample's work function, means SE emission can occur only from within a few nanometres of the surface, giving SEM its topographical sensitivity. BSE are those that undergo Rutherford scattering and carry much more energy, between roughly 50 eV and the energy of the beam electrons.[181] This broad distribution of BSE energies stems from their tendency to undergo numerous scattering events before finally escaping the surface. Their higher energy than SEs means they provide information from deeper within the sample, though this large probe volume gives the BSE detector a lower spatial resolution than either the SE detector or the in-lens detector. As in cTEM and STEM, heavier nuclei will scatter more strongly, meaning the BSE detector can provide Z-contrast, and topographical contrast is supressed by the larger interaction volume. The Zeiss Ultra Plus SEM used in this work is equipped with an energy-selective BSE (ESB) detector. This is an evolution of a

traditional BSE detector equipped with a grid which can be biased with an arresting potential of up to 1.5 kV. Using this grid, low energy BSEs can be filtered out. For example, using a beam energy of 1 keV and arresting potential of 0.9 kV would mean that only BSEs with energies between 0.9 and 1 keV are detected. This effectively increases the surface sensitivity of the detector, eliminating most of the electrons subject to multiple inelastic scattering events.[182] This is especially useful in the context of nanomaterials research, allowing for Z-contrast from very thin layers of low-dimensional materials.[183]

2.5 Spectroscopic Characterisation

Spectroscopy refers to a broad range of techniques that extract information on the physical, chemical, or structural properties of matter from its interaction with electromagnetic[184], matter,[185] or even gravitational waves.[186] Most commonly, incident light is refracted, absorbed, scattered,[184] re-emitted,[187] or a combination thereof, and the resulting spectrum of intensities as a function of frequency may be analysed to provide information on the material. Spectroscopy has a storied history and was foundational in the development of quantum mechanics. Explanation of the discrete lines present in hydrogen emission spectra gave us the Bohr model of the atom,[188] and study of the energies of photoelectrons proved the wave-particle duality of photons, supplanting the wave theory of light proposed by Maxwell.[189]

2.5.1 Ultraviolet-Visible spectroscopy

Being non-destructive, rapid, and relatively simple, ultraviolet-visible (UV-vis) spectroscopy is a useful technique which can provide insight into the electronic structure of materials. The technique may be used on transparent solid samples, though it is most used for low concentration solutions or dispersions. A typical UV-vis spectrophotometer consists of two lamps, a tungsten lamp emitting visible and near-infrared (near-IR) light, and a deuterium lamp emitting UV. The light is passed through a monochromator, which uses mirrors and a diffraction grating to isolate discrete frequencies in the spectrum. This light is passed through the sample, contained in a quartz cuvette for liquids, and the transmitted light intensity is recorded as a function of frequency as the monochromator sweeps from UV to near-IR.[184] This is referred to as the extinction spectrum. A matching reference cuvette filled with solvent is used to account for the absorption, reflection and scattering of light from the quartz, solvent, and interfaces between them. This ideally results in a spectrum containing only contributions from the material being studied, either in solution or suspension.

Mechanistically, the absorption of light occurs when the energy of the incident photon corresponds to that of an electronic transition in the sample. For example, in commonly encountered organic chromophores, the most probable of these transitions is between the highest occupied molecular orbital (HOMO) and the lowest unoccupied molecular orbital (LUMO). These systems contain only molecular orbitals with σ or π symmetry and the allowed transitions correspond to those shown in the energy level diagram

seen in Figure 2.5. Here, the bonding molecular orbitals are denoted σ and π, non-bonding as n, and anti-bonding as σ^* and π^*.[190]

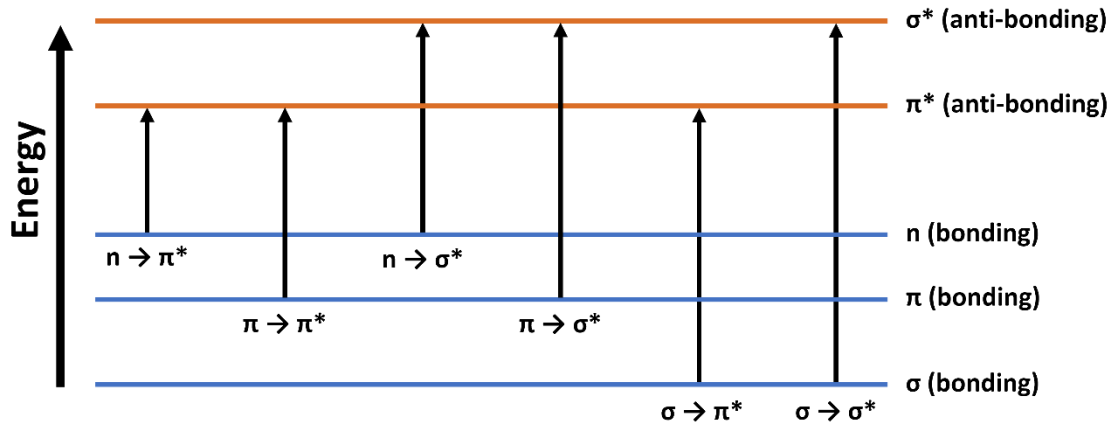

Figure 2.5: Energy level diagram depicting the allowed electronic transitions for a system containing molecular orbitals with σ and π symmetry.

Other mechanisms for absorption exist however, some which are of particular interest in nanomaterials research. Light may be absorbed through localised surface plasmon resonance (LSPR), where its electric field polarises electrons in the conduction band of a metallic nanoparticle.[191] Unlike bulk metals, light can penetrate nanoparticles with a dimension smaller than its wavelength and induce a non-propagating plasmon distributed throughout the particle. This coherent displacement of conduction electrons has an accompanying restoring force and behaves as a harmonic oscillator, where only light with a frequency in resonance with it can drive the excitation.[192] Energy absorbed in this manner is then dissipated, in the case of noble metal nanoparticles largely through valance to conduction band intraband transitions.[193]

The attenuation of light is described by the Beer-Lambert law,[184] relating the extinction, Ext, to the ratio of the incident intensity, I_0, and the output intensity, I:

$$Ext = ln\frac{I}{I_0} = -ln\,T \quad (28)$$

Where T is the transmittance. A linear dependence is found between $-ln\,T$ and the concentration, C, and path length through the sample, l:

$$Ext = \varepsilon Cl \quad (29)$$

Where the extinction coefficient is denoted by ε. It should be noted that the scaling of the Beer-lambert law is limited to dilute solutions, insofar as it assumes that $\varepsilon(\lambda)$ is independent of C. Furthermore, for dilute molecular solutions, it is usually enough to consider only the attenuation of light due to absorption. However, dispersions of nanomaterials usually have a significant scattering component.[194] Therefore, the extinction coefficient, $\varepsilon(\lambda)$, is given by:

$$\varepsilon(\lambda) = \alpha(\lambda) + \sigma(\lambda) \quad (30)$$

Where $\alpha(\lambda)$ and $\sigma(\lambda)$ are the absorption and scattering coefficients as a function of wavelength, respectively.

2.5.2 Raman spectroscopy

Raman scattering is named for Sir Chandrasekhara Venkata Raman, who discovered this inelastic scattering of light.[195] In recognition for this, in 1930 he was awarded the Nobel prize in Physics. Raman spectroscopy is an eminently useful technique for

materials science, the energy shifts of the scattered photons giving insight into a sample's physical properties, and even its environment.[196]

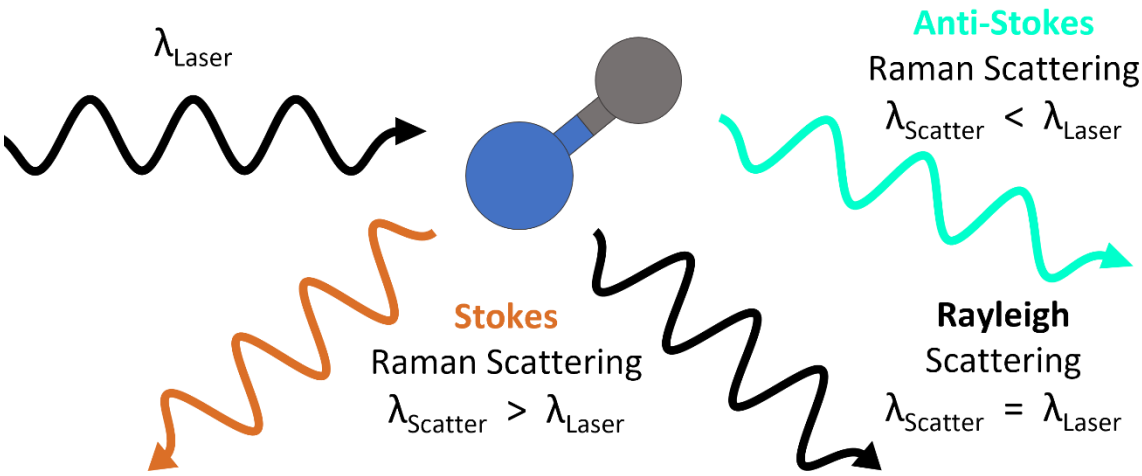

Figure 2.6: Depiction of the possible scattering events that can occur as light of wavelength λ_{Laser} interacts with two bonded atoms.

Most scattered light is scattered elastically, known as Rayleigh scattering, due to its longer wavelength than the dimensions of the lattice.[197] Figure 2.6 shows Rayleigh scattering along with the two principal inelastic Raman scattering events possible: Stokes Raman scattering is shifted longer in wavelength, whereas anti-Stokes is shifted shorter. Though comprising a tiny fraction of the scattered light, their energy shift carries away information about the lattice with which they interacted.

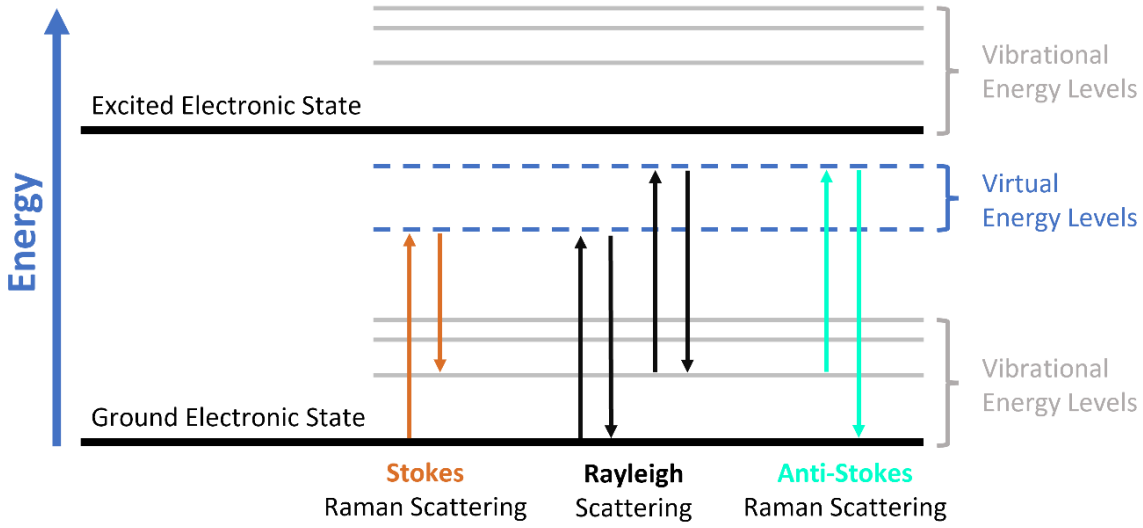

Figure 2.7: Energy level diagram showing the transitions that contribute to Raman scattering.

The mechanism of these scattering events involves two photons. The electric field of the stimulating photon induces a dipole moment in the electron cloud of the material, the magnitude of which being determined by its polarisability.[169] Through this perturbation the photon is absorbed, rationalised as the system moving to a virtual energy level, illustrated in Figure 2.7. This is "virtual" insofar as it is an ephemeral state used to describe the transition of the system from its initial to its final state. In this way, it is more of a mathematical convenience and not a stationary state or valid solution to the wave equation for the system. From this virtual excited state, the electron can relax, emitting the second, scattered photon. Only around one in one thousand photons are scattered at all, the vast majority of which are Rayleigh scattered. Inelastic scattering occurs for only around one in one million photons, where the perturbation drives or is driven by lattice vibrations.[198] Referring to Figure 2.7, the energy loss associated with Stokes Raman scattering is accounted for by the creation of a phonon, the system being left in an excited vibrational state. Conversely, anti-Stokes Raman scattering occurs

when the system is already in an excited vibrational state, the phonon being absorbed, and its energy added to the emitted photon as the system relaxes to a ground state. The Raman shift of the scattered light, $\Delta\tilde{v}$, expressed in wavenumbers (cm^{-1}) is given by the following expression:

$$\Delta\tilde{v} = \frac{1}{\lambda_{Laser}} - \frac{1}{\lambda_{Scatter}} \quad (31)$$

Where λ_{Laser} is the wavelength of the incident light, and $\lambda_{Scatter}$ is the wavelength of the scattered light. Raman spectra are presented as intensity as a function of $\Delta\tilde{v}$, and much structural information can be extracted from the peak positions and their relative intensities. In the context of 2D nanomaterials, defects, strain, and interlayer coupling can also be observed,[199] making it an extremely useful non-contact and minimally destructive technique.

2.5.3 Energy Dispersive X-ray Spectroscopy

EDX is a tremendously useful technique to reveal compositional information from samples in transmission and scanning electron microscopes. As seen in Figure 2.3, the electron beam generates a variety of X-ray emissions in the sample, the most prominent being continuum X-rays and characteristic X-rays.

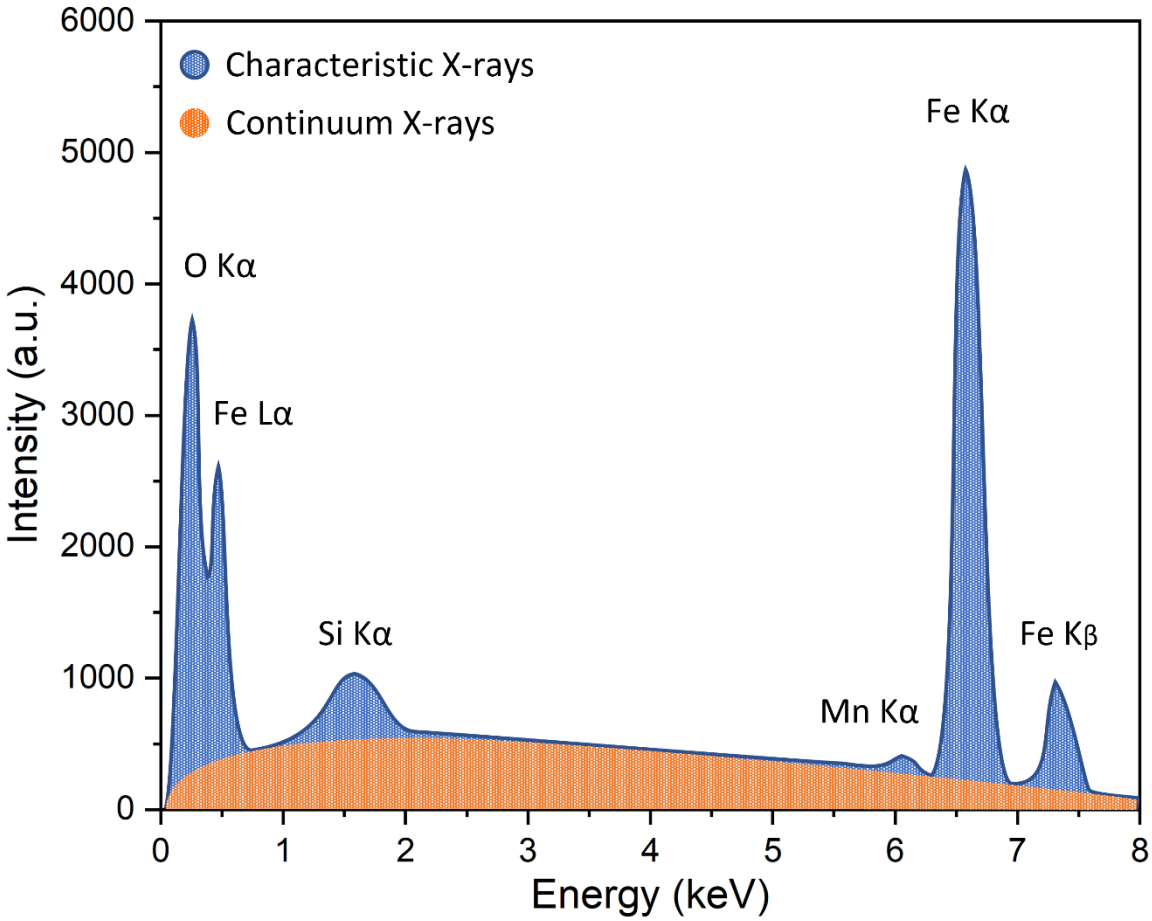

Figure 2.8: Representation of an EDX spectrum, showing characteristic peak positions for a range of common elements. Peak positions from Thompson, A. *et al.*[200]

Continuum X-rays are a consequence of incident electrons being slowed through interaction with the electric field of nuclei in the sample. It is often referred to as *Bremsstrahlung*, German for "braking radiation". When the “brakes” are applied, excess momentum is shed through the emission of a photon in the X-ray frequency range.[201] An electron can lose any amount of the momentum imparted to it by the microscope column and therefore these X-rays form a continuous, low-intensity spectrum with energies no higher than those corresponding to the acceleration voltage. This spectrum

has a soft peak in the low keV range, decaying exponentially from there, making up the orange background represented in Figure 2.8.

While little to no useful information can be gathered from the continuum X-rays, a great deal can be from characteristic X-rays.[202] A simplified model for their mechanism of emission is presented in Figure 2.9. An accelerated electron from the beam ionises an atom in the sample, kicking out a SE. The hole created is filled by an electron which relaxes from a higher energy level, releasing the excess energy as an X-ray photon. The energy levels in the atom are quantised and unique to different elements, meaning that by recording the energy and intensity of the X-rays emitted, the elemental composition of the sample can be revealed. The photons' discrete energies lead to a spectrum of peaks corresponding to their associated element and transition. Peaks are assigned a designation consisting of their element's symbol and letters indicating the final and initial shell of the relaxing electron.[203] As seen in Figure 2.9, an electron relaxing from the L shell to K shell generates a K_α emission (quantum number $n = 2$ to $n = 1$); M shell to K shell generates a K_β emission (quantum number $n = 3$ to $n = 1$); the M shell to L shell generates a L_α emission (quantum number $n = 3$ to $n = 2$); and so on. Allowed transitions within shells are also possible, though they are of low probability and energy, meaning they are usually neglected in EDX analysis. An electron microscope equipped with a typical Si-Li EDX detector becomes a powerful tool in compositional analysis, and SEM or STEM allows for elemental composition to be mapped on a per-pixel basis.[204] While EDX measurements can be performed concurrently with imaging, some considerations need to be made, as the acceleration voltage needs to exceed that of the transitions being probed. Ideally, it would be not less

than 1.5 times the energy required so that a statistically significant count of the X-rays is recorded.[205] For example, the Fe K_α emission is at 6.40 keV, meaning an acceleration voltage of around 10 kV should be used at a bare minimum, considerably higher than necessary for most SEM imaging and may lead to specimen damage. Emissions for inner shell transitions in heavier elements can only be probed in TEM at high potentials, often exceeding 100 kV.[206]

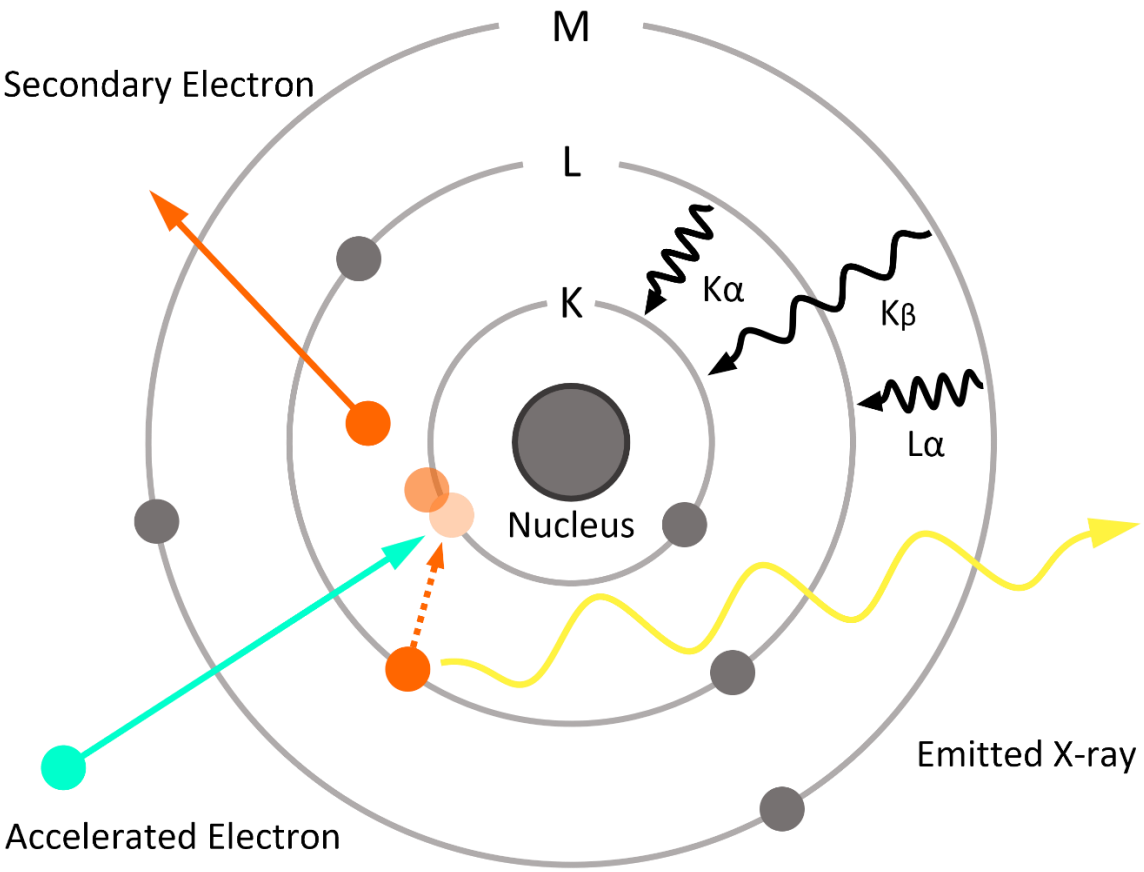

Figure 2.9: Shell diagram describing the ejection of secondary electron and the release of a characteristic X-ray photon.

2.5.4 Electron Energy Loss Spectroscopy

As the name suggests, EELS is a technique which records the energy lost by electrons to inelastic scattering after passing through the sample in TEM. Much like EDX, EELS can ascertain the elemental composition of a sample, but the nature of inelastic scattering events means that information regarding bonding, oxidation state and optical properties may also be gathered.[207] An EEL spectrometer, located at the base of a TEM column as seen in Figure 2.4a, uses a magnetic prism to deflect incoming electrons, dispersing them according to their energy.

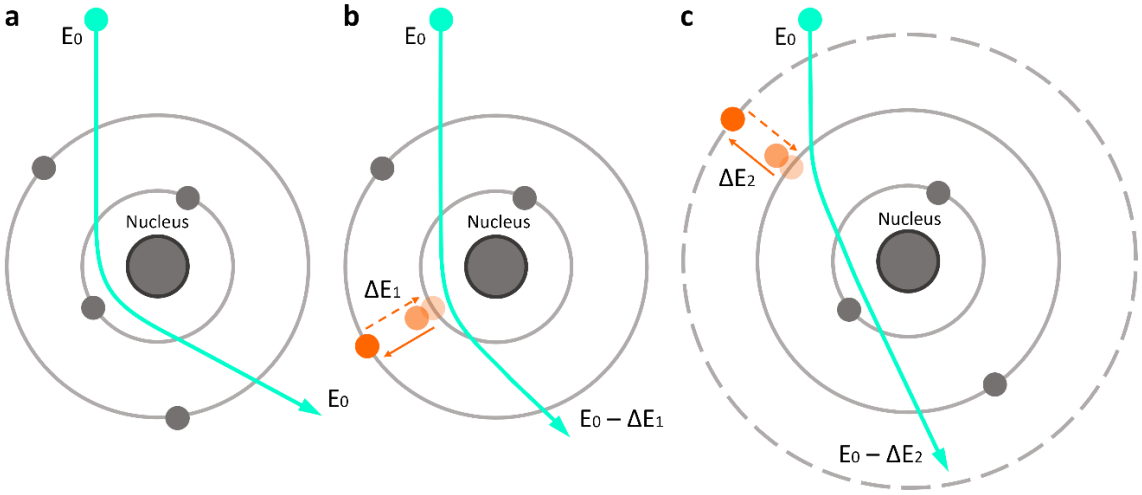

Figure 2.10: Shell diagrams illustrating scattering of incident electrons. (a) elastically scattered (zero-loss), (b) inelastically scattered by core shell electron (high/core-loss), (c) inelastically scattered by valence shell electron (low-loss).

Scattering events in EELS are broadly categorised as zero-loss (Figure 2.11a), core-loss (Figure 2.11b), and low-loss (Figure 2.11c). Zero-loss electrons may be non-scattered; minimally scattered inelastically through a phonon excitation; or scattered elastically through interaction with the atomic nucleus. The mass of the electron is miniscule

compared to the nucleus and as such the energy transfer between them is usually below the detection threshold.[208] Core-loss electrons lose energy through single excitation of a core shell electron in the sample (Figure 2.11b) and are considered high-loss due to the relatively larger energy required to promote an inner shell electron to a higher energy level. Low-loss electrons arise from interactions with valence shell electrons in the sample (Figure 2.11c), being inelastically scattered through excitation of a plasmon.

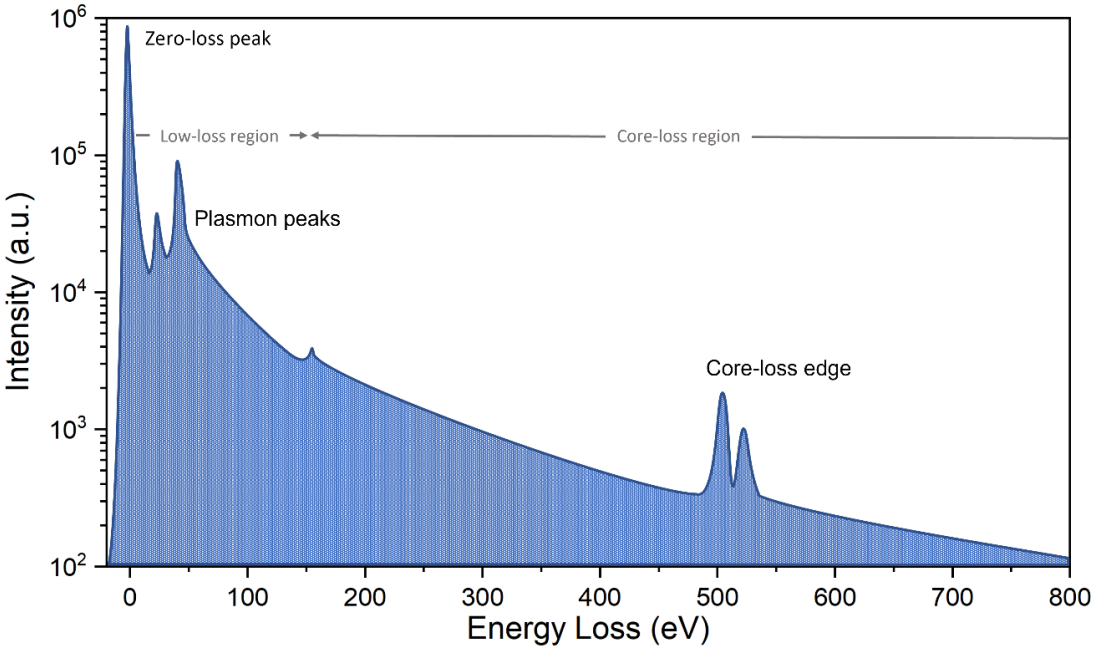

Figure 2.11: Representation of EEL spectrum, highlighting prominent features and indicating the low-loss and core-loss regions.

EEL spectra are broken down according to three previously discussed scattering classifications. A facsimile of an EEL spectrum is included in Figure 2.11 with exaggerated features for ease of explanation. The zero-loss peak does not provide any spectroscopic information about the sample but does for the illumination system of the microscope. As the zero-loss peak is of nonzero width, it implies a distribution in the electron energies of the beam. In a well-tuned system, most sources of broadening are

minimised, so the width of the zero-loss peak indicates how monochromatic the electron source is. Using a cold-cathode FEG, a range of about 0.3 eV is typical, and the zero-loss peak width gives an estimate of the resolution of the measurement.[209] The zero-loss peak may also be used to estimate the local thickness of a sample. A natural log ratio is used to determine the thickness:[210]

$$t = \lambda_{in}\, ln \frac{I_t}{I_z} \quad (32)$$

Where t is the local thickness of the sample, λ_{in} is the inelastic mean free path of the sample, I_t is the integrated total intensity of the spectrum, and I_z is the integrated intensity of the zero-loss peak. This expression is fairly intuitive, relating the total electron count to the count of those which have not been scattered. A value of λ_{in} needs to be obtained in order to find the absolute thickness of the sample, but without it, $\frac{t}{\lambda_{in}}$ at least indicates the relative thickness of different regions in the sample. λ_{in} can be determined experimentally using the following expression:[211]

$$\lambda_{in} \approx \frac{106F \frac{E_0}{E_m}}{ln\, 2\beta \frac{E_0}{E_m}} \quad (33)$$

Where E_0 is the energy of the non-scattered electrons, β is the collection semiangle for the measurement, E_m is a mean energy loss term for the sample, and F is relativistic correction factor. E_m is related to atomic number Z as follows:

$$E_m = 7.6Z^{0.36} \quad (34)$$

The relativistic correction factor is given by:

$$F = \frac{1 + \frac{E_0}{1022}}{1 + (\frac{E_0}{511})^2} \quad (35)$$

2.6 X-ray Diffraction

X-ray diffraction (XRD) can be explained using the Bragg condition, named for W.H. Bragg and W.L. Bragg. This mathematical description, proposed in 1913, considers a solid crystal consisting of atomic planes, from which waves are scattered specularly. X-rays have λ like that of atomic spacings, and thus an interference pattern emerges.

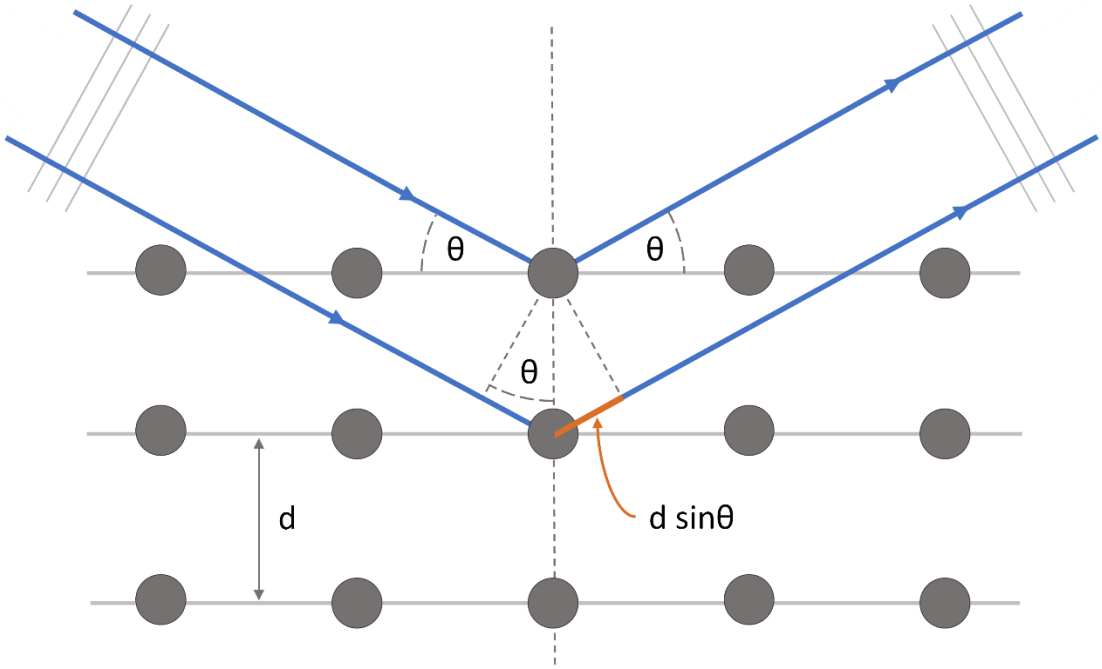

Figure 2.12: Diagram of Bragg diffraction from atomic crystal planes.

Figure 2.12 illustrates two incoming rays of wavelength, λ, being scattered such that they interfere constructively. This is maximised at a glancing angle, θ, such that the path of the lower ray is extended by a whole number multiple of λ.[212] The crystal's plane separation, d, is therefore determined by the Bragg equation:

$$n\lambda = 2d\,sin\,\theta \tag{36}$$

Where n is the diffraction order. Under the Bragg condition, reflections from successive crystal planes must interfere constructively as is the case with the first-order ($n = 1$) reflections in Figure 2.12.

An X-ray diffractometer relies on an X-ray source of known wavelength, often Cu K_α at 1.54 Å or Mo K_α at 0.71 Å. For single crystal samples, the sample is rotated about a vertical axis as the diffractometer records the reflections over a range of angles. This produces a diffractogram of intensity vs. angle with sharp peaks corresponding to reflections from crystal planes (h, k, l) from which lattice parameters can be derived. Powder XRD is performed for granular samples, the random orientation of the grains negating the need to rotate the sample about a central axis to average out the possible crystal orientations.[213]

2.7 Electrochemical Characterisation

At its core, electrochemistry concerns the influence of voltage on chemical reactions. Typically, a potential difference is applied between two electrodes which are separated by an electrolyte. Electrons are able to flow externally between the electrodes, but cannot flow through the electrolyte, and therefore ions must serve as charge carriers to complete the circuit. In this way, electrochemical reactions differ from conventional

reactions as the electron transfer between species takes place *via* the external circuit and not as a direct exchange between atoms.[214]

Electrochemical measurements therefore involve careful application and measurement of potential and/or current to a sample in an electrochemical cell. A simple two-electrode cell (Figure 2.13a) presents issues for precise analytical electrochemistry. In a two-electrode system, the reference electrode (RE) and counter electrode (CE) are combined, that is, both the voltage and current of the working electrode are measured with respect to the counter electrode. This can lead to changes in reference potential due to the fluctuating current being simultaneously provided by the CE. This also results in only the total potential difference between the working electrode (WE) and RE/CE being measured. A three-electrode cell (Figure 2.13b) solves these problems by splitting the RE and CE to maintain a constant potential at the RE. This also enables simple analysis of the half-cell potential as the RE is of known potential.[215] Potential is measured and/or applied between the WE and RE, and no appreciable current passes between them, with current being measured and/or applied between WE and CE.

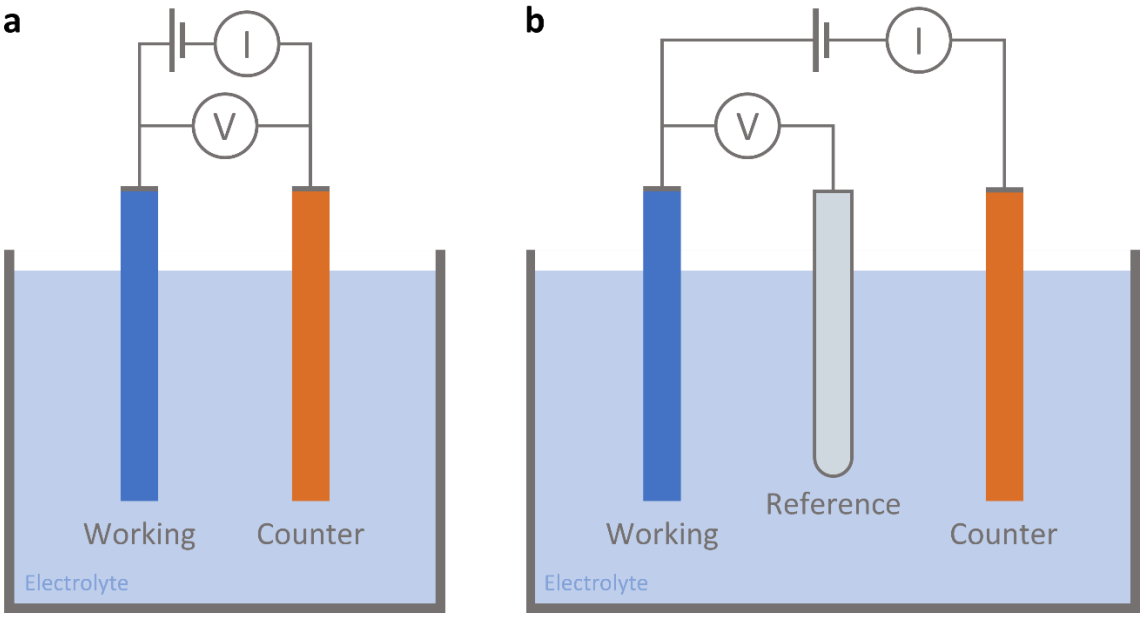

Figure 2.13: Diagram of (a) a two-electrode electrochemical configuration and (b) a three-electrode electrochemical configuration.

There are three primary analytical techniques used to measure the performance of supercapacitor electrodes. These are cyclic voltammetry (CV), galvanostatic charge/discharge (GCD) and electrochemical impedance spectroscopy (EIS).

CV is a technique where the current of an electrochemical cell is measured in response to a linear change in the applied potential. The potential is swept at a chosen scan rate (usually given in mVs^{-1}) until a potential limit is reached. The potential is then swept in reverse to another potential limit.[216] This process repeats for as many cycles as needed for the measurement. Cyclic voltammograms (CVs) provide a great deal of useful information on the nature of supercapacitor electrodes. Materials which store charge solely through EDLC should appear approximately rectangular in CVs, with no clear redox peaks. Pseudocapacitive materials on the other hand often have very clear redox peaks corresponding to the faradaic processes on the electrode surface, ideally with little

to no potential separation between the oxidation and reduction peak.[216,217] Ordinarily, diffusion and polarisation lead to a theoretical minimum peak-to-peak separation, ΔE_p, which at 25° C is given by:

$$\Delta E_p = E_{pa} - E_{pc} = \frac{57\ mV}{n} \quad (37)$$

Where E_{pa} is the peak potential at the anode, E_{pc} is the peak potential at the cathode, and n is the number of electrons transferred. However, as the redox processes in supercapacitors are surface-controlled, the theoretical minimum value of ΔE_p is 0 mV.

GCD involves the application of a constant current to the electrode being studied until a potential limit is reached. When the limit is reached, an equal current is applied in reverse until the electrode has discharged to a lower potential limit.[218] This process is repeated n_c times. In this way it can be used to determine the cycling behaviour of a capacitor and as a secondary means of calculating the capacitance. The voltage drop V_{drop} when the current is switched in GCD is often used to calculate the equivalent series resistance (ESR), of supercapacitor electrodes, or supercapacitors themselves. ESR, denoted R_{ES}, is given by the following expression:[217]

$$R_{ES} = \frac{V_{drop}}{2I_{GCD}} \quad (38)$$

Where I_{GCD} is the applied current in the GCD measurement. This is due to the current switching from $+I_{GCD}$ to $-I_{GCD}$ for a net change of $2I_{GCD}$. GCD measurements on the BioLogic potentiostat used in this work are referred to as galvanostatic cycling with potential limitation (GCPL).

EIS is a powerful, if somewhat arcane technique to probe the dynamics of electrochemical systems.[219] Measurements involve applying a small AC voltage (around 5 mV) to the device and measuring the current response. The AC signal is swept over a range of frequencies and the response is analysed to determine the impedance of the device. EIS is particularly relevant to supercapacitor research, as it can provide valuable information about the performance and behaviour of these devices, including the internal resistance, charge transfer resistance and capacitance. It can also be used to study the electrochemical processes that occur within the device, such as the charge transfer between the electrodes and the electrolyte. There are two commonly used plots that are used to visualise EIS: Bode plots and Nyquist plots. They each provide different information about the behaviour of the device. Both EDLC and pseudocapacitance can be probed using EIS and can be visualised in a Nyquist plot, which is a graphical representation of the impedance data obtained in EIS. In a Nyquist plot, the imaginary component of the impedance (Z'') is plotted on the y-axis, and the real component of the impedance (Z') is plotted on the x-axis. EDLC appears as a straight line on the Nyquist plot, while pseudocapacitance is curved. Another useful graphing technique in EIS is the Bode plot. Bode plots are a logarithmic and are used to represent the magnitude and phase of the impedance as a function of frequency. The magnitude of the impedance is plotted on the y-axis, and the frequency is plotted on the x-axis. Bode plots provide insight into the frequency dependence of the impedance and identify resonance frequencies in the device, they are also more intuitive than the physically abstract real and imaginary impedance components in a Nyquist plot.

2.7.1 Capacitance Measurements in Two- and Three-Electrode Systems

The total capacitance, C, for a supercapacitor is given by an equivalent circuit of individual capacitors with capacitance corresponding to the anode capacitance C_a and cathode capacitance C_c:[220]

$$\frac{1}{C} = \frac{1}{C_a} + \frac{1}{C_c} \quad (39)$$

Measuring the intrinsic performance of a material is made simpler by using a three-electrode or half-cell measurement. By decoupling the counter electrode, nonidealities such as mismatched capacitance on either side of the cell can be avoided, greatly simplifying experimental design and analysis. A common figure of merit used to describe supercapacitors is the specific capacitance, expressed as either areal (per unit area, C_A), gravimetric (per unit mass, C_m) or volumetric (per unit volume, C_v). To obtain the specific capacitance (C_S) from a CV measurement, the following general expression is used:[63]

$$C_S = \frac{Q}{2SVv} \quad (40)$$

$$C_S = \frac{1}{2SVv}\int_{V^-}^{V^+} I(V)\,dV \quad (41)$$

Where S is either the active area, mass, or volume of the device, A, m, or v; v is the scan rate; and V^-, V^+ are the lower and upper limits of the potential sweep, respectively. From GCD, the areal capacitance is obtained via the equation below:

$$C_S = \frac{I}{S\frac{dV}{dt}} \quad (42)$$

Where I is the discharge current, V is the potential during discharge after the resistive drop and t is the discharge time. Thus, $\frac{dV}{dt}$ is the slope of the curve under discharge.

Unlike a three-electrode measurement setup, a two-electrode or "full-cell" setup is interpreted as two capacitors connected in series. Assuming a symmetrical supercapacitor, we use equation (39), but where the values of C_a and C_c are equal:

$$\frac{1}{C_{(device)}} = \frac{2}{C_{(e)}} \quad (43)$$

thus:

$$C_{(e)} = 2C_{(device)} \quad (44)$$

Where $C_{(e)}$ is the capacitance of one of the equal electrodes, and $C_{(device)}$ is the capacitance of the symmetrical device. To compare measurements obtained in either two-electrode or three-electrode configurations, we normalise the measurements to a single electrode measured in a three-electrode configuration by using a factor, N:[221]

$$\frac{C_{(e)}}{N} = \frac{2C_{(device)}}{N} \quad (45)$$

To obtain a comparable C_S from a two-electrode measurement of a device, a further correction factor is applied to adjust the combined area, mass, or volume of the two electrodes to that of a theoretical single electrode.[222,223] For a symmetrical supercapacitor, the total area, mass, or volume is twice that of the individual electrodes, such that the normalisation factor for the theoretical electrode, $N_{(e)}$, is given by:

$$2N_{(e)} = N_{(device)} \quad (46)$$

For specific capacitance, equation (45) then becomes:[224]

$$\frac{C_{S(e)}}{2N_{(e)}} = \frac{2C_{S(device)}}{N_{(device)}} \quad (47)$$

$\frac{C_{S(e)}}{N_{(e)}}$ is definitionally the normalised specific capacitance of the electrode, denoted C_{SN}, and similarly $\frac{C_{S(device)}}{N_{(device)}}$ is the normalised specific capacitance of the device $C_{SN(device)}$. We then obtain the following expression for C_{SN} for symmetric supercapacitors, allowing more direct comparison between two- and three-electrode measurements:

$$C_{SN} = 4C_{SN(device)} \quad (48)$$

2.8 Four-Point Probe Measurements

The electrical resistance or conductivity of a material may be found using the four-wire, four-point, or Kelvin sensing technique. Named for William Thomson, Lord Kelvin who pioneered four-point measurements in 1861 in order to measure low resistance samples.[225] Often used to measure R_s in thin-film materials, this technique is desirable as it avoids any contribution from contact resistance by having independent sources of potential and current. Figure 2.14 shows the circuit and configuration of a four-point probe. The current, I, is supplied through the "force" connections 1 and 4 while the voltage, V, and voltage sense are supplied through connections 2 and 3. Provided that the voltmeter has sufficiently high resistance, the current flowing through that circuit will be negligible, thereby resulting in a negligible voltage drop through the wires and contacts. This allows for accurate determination of the sample's resistance.

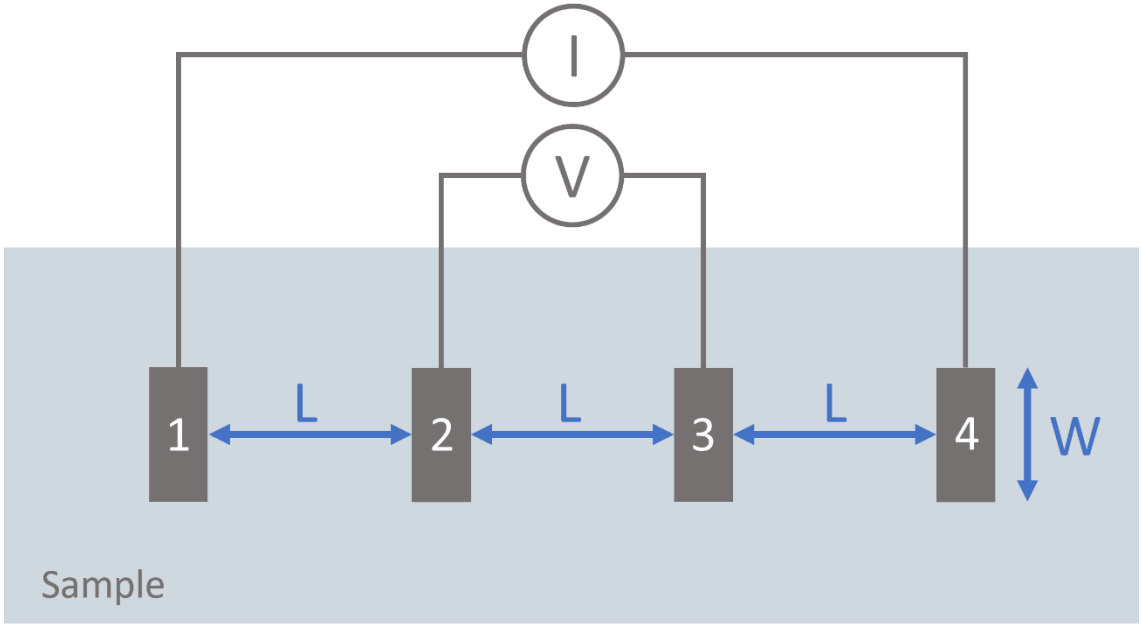

Figure 2.14: Schematic representation of a four-point probe measurement with probes 1, 2, 3 and 4.

The resistance for the central region of area, A, is given by the equation below:[226]

$$R = \frac{\rho L}{A} = \frac{\rho L}{tW} \quad (49)$$

Where R is the bulk resistance, ρ is the resistivity, L is the length, W is the width, and t is the thickness of the region between electrodes 2 and 3. For conductive films, t is often unknown and so the sheet resistance, R_s, is the only parameter that can be directly determined from a resistance measurement, where:

$$R_s = \frac{\rho}{t} \quad (50)$$

R_s is given in units of $\Omega/\square$ (ohm per square) to avoid confusion with bulk resistance in Ω. Subbing R_s into equation (49) we obtain:

$$R = \frac{R_s L}{W} \quad (51)$$

The value of R can be calculated from the reciprocal slope of an IV curve and used to find a value of R_s for a given film. Of course, should the dimensions of the sample be fully known, the conductivity, σ can be determined from the reciprocal of ρ.

3 MXENE SYNTHESIS AND CHARACTERISATION

Given that this thesis and most of my other work is centred around $Ti_3C_2T_x$, the characteristics of the synthesised material are of paramount importance. This chapter details the synthesis and ink preparation that underpins all other experiments, as well as a simple, single-step method for improving MXene yield and conductivity through freeze-thaw delamination.

3.1 $Ti_3C_2T_x$ 'MILD' Synthesis and Size Selection

The desire for a less hazardous etchant for Ti_3AlC_2 led to the use of the 'MILD' synthesis route.[34,38] Initially, 6M HCl and a 5:1 molar ratio of LiF to Ti_3AlC_2 was used, equivalent to 0.67:1 (m/m) of LiF to Ti_3AlC_2. It was later found that increasing the HCl concentration to 9M and using a > 7.5:1 molar ratio of LiF to Ti_3AlC_2 resulted in fewer defects and higher conductivity.[37] In current literature, the prevailing MILD synthesis protocol uses a 12:1 molar ratio of LiF to Ti_3AlC_2, or 1.6 g LiF to 1 g Ti_3AlC_2. This has benefits in terms of yield, flake size and conductivity.[39]

First a note on safety. While creating on the order of 5% HF *in situ* with LiF and HCl is preferable to more concentrated HF etchants, care still must be taken to minimise risk. Calcium gluconate gel and HEXAFLUORINE® eyewash need to be on hand in the

event of exposure, and that exposure must be avoided in the first place. While some would recommend heavy neoprene gloves even when working with low-concentration *in situ* HF, I personally find the loss in dexterity when handling small items like centrifuge tubes to outweigh their added protection. Nitrile gloves are sufficient for splash contact with up to 30% HF,[227] as long as they cover the wrists and are worn with a face shield and lab coat, they constitute perfectly acceptable PPE.

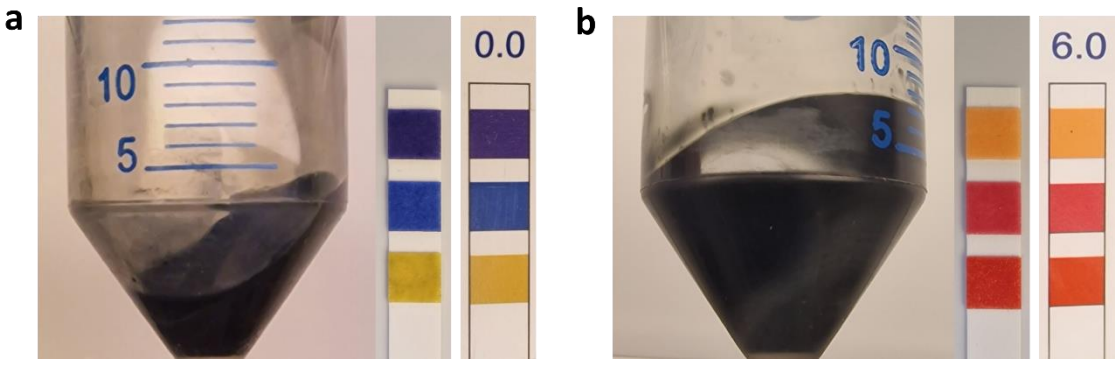

Figure 3.1: Sediments and indicated pH of supernatant during washing. The pH shown on the indicator sticks should be considered only a rough guide as to the completeness of the washing. (a) After first wash. (b) After sixth wash.

The etching procedure is relatively straightforward, but there are certain steps where attention should be paid to avoid problems with the final material. For example, the addition of Ti_3AlC_2 to the etchant needs to be done slowly, to avoid excessive bubbling and overheating which can be an issue for the health of material and scientist both. The heating for the reaction should also remain off until all of the MAX phase is added. A note on heating: the choice of 35°C for the etching procedure may seem arbitrary, and that's because it is. In reality, the reaction can be done quite successfully at room temperature,[39] though choosing to heat to a temperature slightly in excess of this

isolates the synthesis from any seasonal variations in the ambient temperature, helping to keep batches consistent year-round.

Once the etching is complete, the wash should be started immediately. Using a large volume of water in every wash will reduce the number of washes required, saving time. After each wash, it is important to ensure that the supernatant is discarded into a waste container designated for HF-containing liquids. As the pH of the supernatant increases with each wash, small amounts of MXene will begin to be dispersed, lending it a greenish colour. The sediments will also be seen to start to swell and change in sheen, slowly becoming a uniform, glossy black colour. Swelling is evident in Figure 3.1, the sediments having cleary increased in volume comaring the first (Figure 3.1a) and sixth (Figure 3.1b) washes. As water infiltrates the layers in the sediments they expand, but also become more difficult to redisperse for the final washes. Large chunks can remain if they aren't mixed sufficiently, and this will likely impact the effectiveness of the washing procedure.

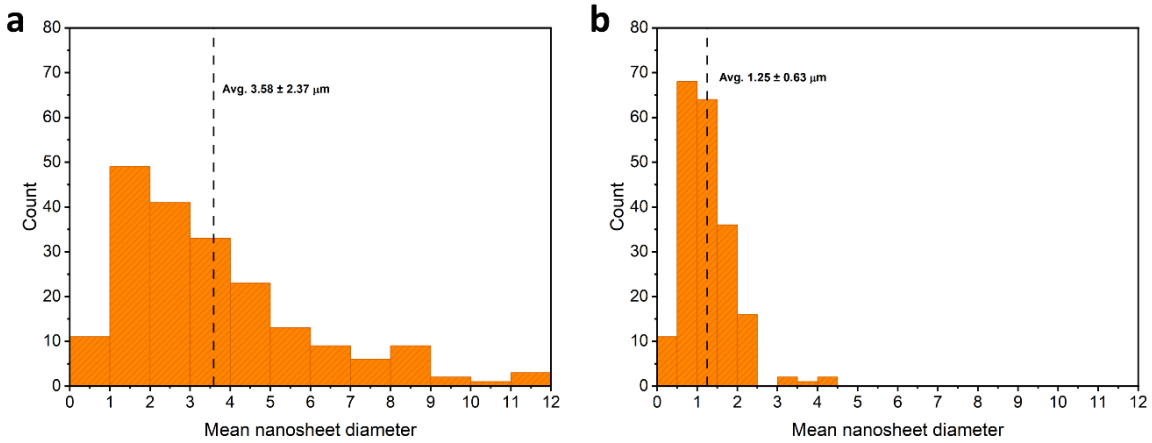

Figure 3.2: Size distributions of flakes removed from final inks. (a) Size distribution of sediments, comprised of large, multilayer flakes. (b) Size distribution of small flakes which remain in supernatant after 1 hour at 5000 rpm.

When the pH of the supernatant has reached 6.5, the sediments are redispersed and centrifuged relatively slowly (1500 rpm) to sediment any partially etched multilayer MXene or remaining MAX phase. A size distribution of these particles can be seen in Figure 3.2a. The mean diameter of these nanosheets is 3.58 ± 2.37 µm. The supernatant now contains only etched mono- and few-layer MXene. The final 5000 rpm centrifugation's purpose is twofold, firstly, it is a facile way to concentrate the dilute supernatant into a slurry which can be redispersed to whatever concentration is desired, but it also leaves the smallest flakes in the supernatant, which negatively impact the conductivity of the final MXene.[228] These flakes have an average diameter of 1.25 ± 0.63 µm as seen in Figure 3.2b and a much narrower distribution than the large, multilayer flakes. The wet, clay-like sediments from the final centrifugation may be diluted or used as is for applications such as extrusion printing.[229]

3.2 Physical Characterisation of As-Synthesised $Ti_3C_2T_x$

As seen in Figure 3.3a, the final ink when diluted is of a strong green colour, and shows strong Tyndall scattering, a hallmark of colloidal suspensions.[36] In contrast, filtered films of the material have a pronounced purple hue and metallic sheen (Figure 3.3b).[230]

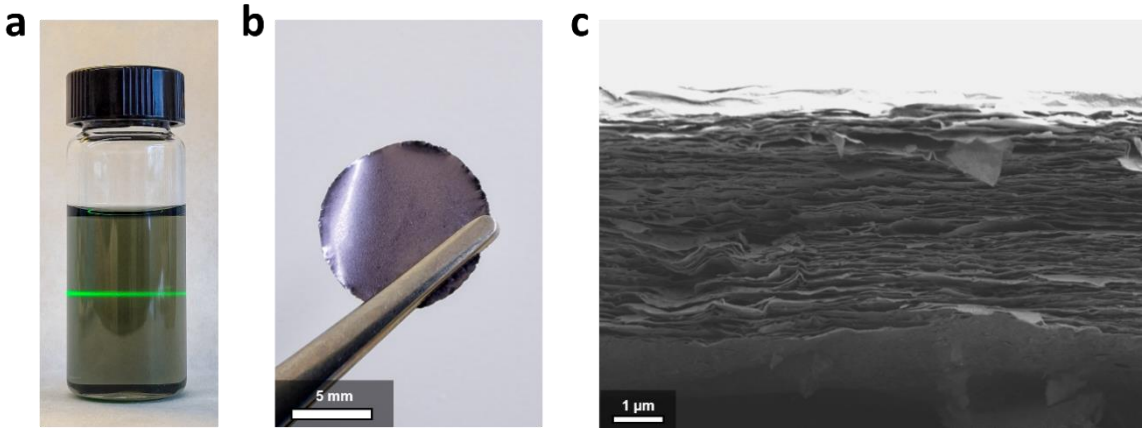

Figure 3.3: $Ti_3C_2T_x$ dispersion and film morphology. (a) Scattering of laser light showing Tyndall effect in dilute dispersion; (b) photograph of typical $Ti_3C_2T_x$ filtered film showing metallic, purple lustre; and (c) SEM micrograph using SE detector of filtered film cross-section, showing well-aligned flakes.

In cross-section, the internal structure of the $Ti_3C_2T_x$ films are fairly well-aligned, and the edges of individual flakes are easily visible, as in the SEM image in Figure 3.3b. This is in stark contrast to the bulky, layered crystals of its precursor Ti_3AlC_2 MAX phase.[231] Further evidence of the successful delamination of MXene nanosheets appears in the X-ray diffractograms of Ti_3AlC_2 and $Ti_3C_2T_x$ in Figure 3.4a and b, respectively. XRD gives one of the clearest pictures of the structural changes going from MAX phase to MXene. In Figure 3.4a, the MAX phase possesses all of the reflections expected for its $p6_3/mmc$ space group and the inset shows that it has a (002) peak position at $2\theta = 9.493°$.[230] This corresponds to a c-lattice parameter of 18.6 Å, which is characteristic of

Ti_3AlC_2.[232–234] In contrast, the diffractogram in Figure 3.4b for the filtered $Ti_3C_2T_x$ film comprises only (00*l*) reflections, and the peaks themselves are noticeably broadened.

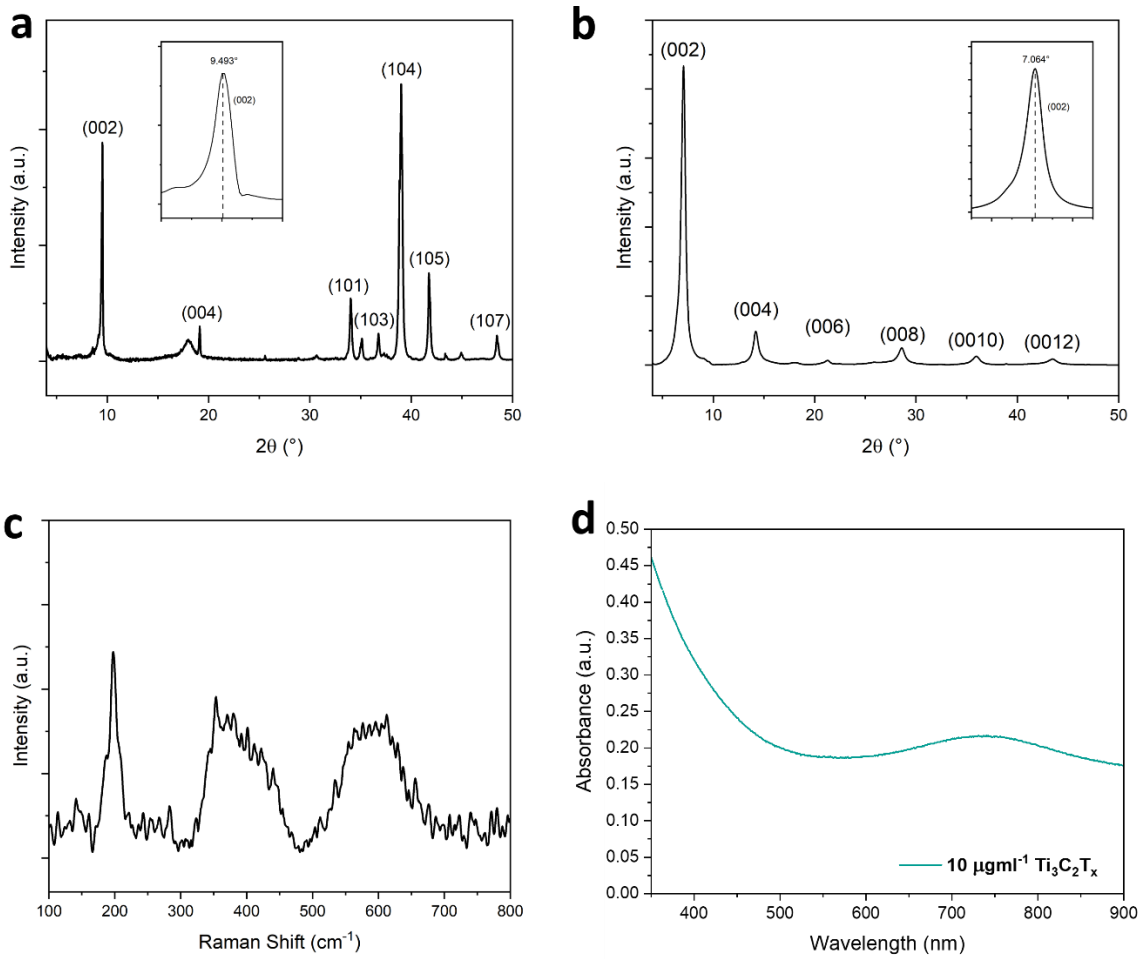

Figure 3.4: Crystallographic and spectroscopic measurements of the MXene and its parent MAX phase. (a) X-ray diffractogram for Ti_3AlC_2 MAX phase with prominent reflections indexed, inset is detail view of the (002) peak position. (b) X-ray diffractogram for $Ti_3C_2T_x$ MXene with prominent reflections indexed, inset is detail view of the (002) peak position. (c) Raman spectrum of $Ti_3C_2T_x$ film showing characteristic bands. (d) UV-Vis spectrum of $Ti_3C_2T_x$ dispersion with LSPR band between 700-800 nm.

Unlike the parent MAX phase there are no visible a-lattice reflections as well-aligned films prepared from properly delaminated MXene should only show (00*l*) peaks.

Furthermore, the (002) reflection is significantly shifted to $2\theta = 7.064°$. It should be noted that the indexing convention for MXenes is different to that of other 2D materials. Normally, (00*l*) reflections would be designated (001), (002), (003), and so on because the sample contains 2D sheets with identical layers, and one sheet per unit cell.[235] In this way, the c-lattice parameter corresponds to the d-spacing. It has become the norm in MXene research to refer to these reflections instead as (002), (004), (006), and so on, due to the parent MAX phase having two layers per unit cell.[230] This is to allow for more direct comparison with diffractograms of MAX phases, despite not being technically "correct" in terms of crystallography. Due to this convention, the c-lattice parameter obtained from the (002) peak for $Ti_3C_2T_x$ must be halved to find the d-spacing between the individual layers. In our case, the d-spacing for the filtered $Ti_3C_2T_x$ film is 12.5 Å (Figure 3.4b). The interlayer spacing (occupied by intercalated water and ions) can then be determined by subtracting the d-spacing obtained for dry, multilayer $Ti_3C_2T_x$ obtained from HF etching, 9.4 Å.[230] This gives us an interlayer spacing of 3.1 Å, corresponding to approximately 1.1 layers of water. Raman spectroscopy (Figure 3.4c) for the as-synthesised $Ti_3C_2T_x$ is also typical, with expected bands at 210, 380, 580 and 630 cm^{-1} from the in-plane and out-of-plane vibrations of the T_x surface groups.[236] UV-Vis spectroscopy in Figure 3.4d shows the characteristic absorption peak of $Ti_3C_2T_x$ at ~780 nm. This corresponds to a LSPR in the MXene sheets and is responsible for the green colour of dilute solutions and reflective purple colour of the dry material.[237–240]

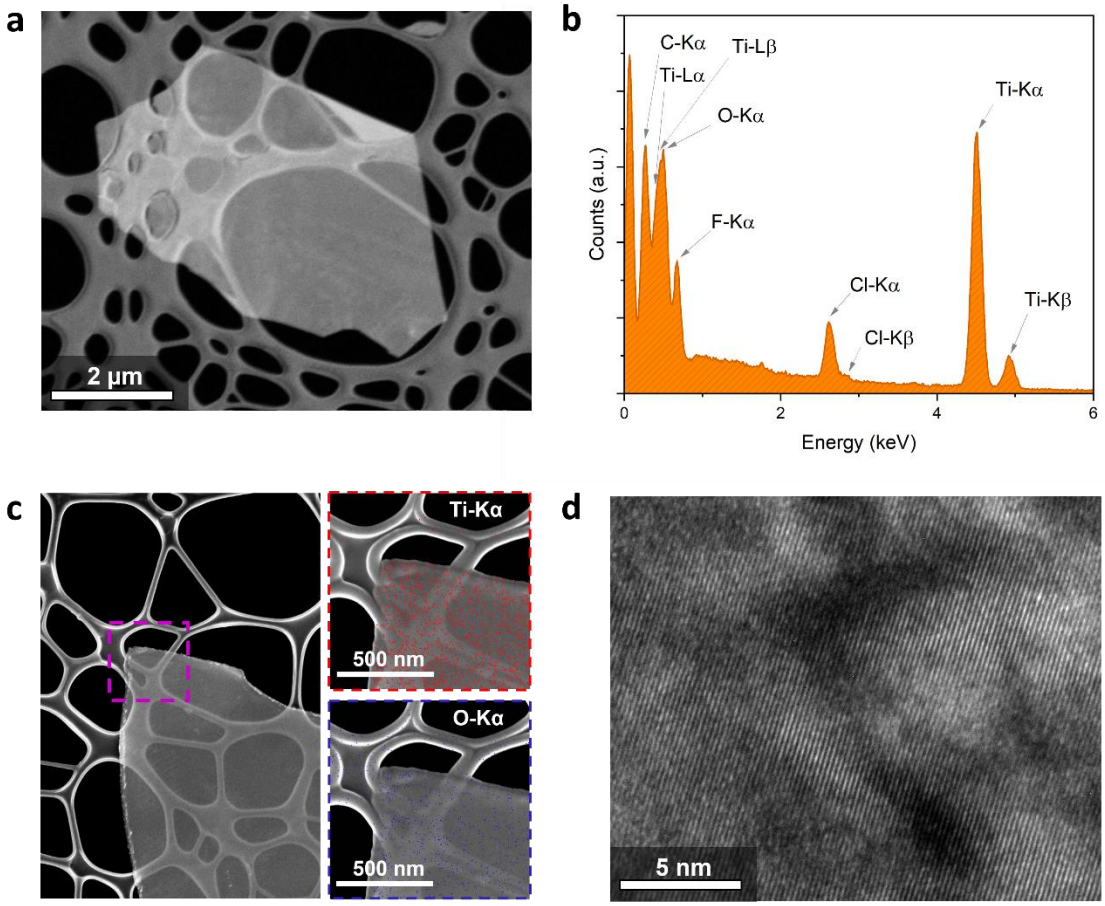

Figure 3.5: Micrographs and X-ray spectra of $Ti_3C_2T_x$ flakes. (a) ESB SEM micrograph of flake on lacey carbon at 1.5 kV. (b) EDX spectrum of MXene film obtained at 10 kV, showing typical elemental composition and removal of Al from the parent MAX phase. (c) SEM image of MXene flake with Ti-K_α and O-K_α EDX maps. (d) HRTEM of $Ti_3C_2T_x$ flake, highlighting excellent crystallinity and absence of defects.

Electron microscopy and its associated spectroscopic techniques can also give good insight into the properties of the synthesised MXene. Figure 3.5a shows an SEM micrograph of an isolated $Ti_3C_2T_x$ flake, the ESB detector being used to gain high contrast from the thinner but higher atomic weight MXene compared to the supporting lacey carbon. No prominent defects can be seen, or signs of oxidation at the edges. The EDX spectrum in Figure 3.5b gives a qualitative description of the surface chemistry of

the MXene. As can be seen, in addition to the Ti and C peaks associated with the titanium carbide centre of the flakes, there are also prominent O, F and even Cl peaks. While it is usually only reported that the T_x terminations consist of O, OH, and F,[37] it is intuitive that in the MILD etching process some Cl functionalisation would occur due to the high concentration of HCl. The absence of any appreciable peaks from common cations implies that this is more than likely not as a result of contamination or incomplete washing. Furthermore, the absence of any Al peaks in the EDX spectrum indicates successful etching, that is, complete removal of the "A" MAX phase layer. Figure 3.5c shows an SEM image of a MXene flake, with inset EDX map of Ti-K_α and O-K_α emissions. This serves to confirm the identity of the MXene synthesised and indicates no large concentrations of oxygen which may arise from degradation. HRTEM of a $Ti_3C_2T_x$ nanosheet shows close to atomic resolution, with the lines attributable to the a-lattice fringes of $Ti_3C_2T_x$. The fringes are separated by ~2.5 Å, as expected for the $Ti_3C_2T_x$ a-lattice parameter.[241]

3.3 Freeze-Thaw Assisted Delamination for Improved Yield and Conductivity

The loss of lab and equipment access on account of Coronavirus lockdowns and working restrictions was, to put it mildly, quite bad overall. Not all bad though. Quite serendipitously, I stumbled upon a very simple technique to improve the yield of MILD-etched $Ti_3C_2T_x$. When the university finally reopened after the most restrictive early lockdowns, we were limited to morning or afternoon shifts which alternated weekly. To make matters worse, we were limited to two occupants per lab. The effect of this in aggregate was a period in which both the number of shifts and the length of each shift was cut much shorter than I was accustomed to. Ordinarily, I would start a Ti_3AlC_2 etch in the morning, and begin the washing process at the same time the following day. It would then take on the order of 12 hours in total to prepare the final ink and start the vacuum filtration to determine its concentration. In this way, two days after beginning the etching process I would have a usable $Ti_3C_2T_x$ ink of known concentration. This, under the new regimen, was no longer possible.

With time constraints to work around, the best I could do was to halt the washing procedure once the pH had reached around 6 – 6.5, purge the centrifuge tubes containing the sediments with nitrogen, seal them, and place them in the fridge overnight. The real change came when the only slots available meant that the washing and ink preparation had to be stopped over a weekend. In the hopes of avoiding any degradation due to the trace amounts of etchant left in the almost pH-neutral sediments, I stored them in the freezer at -20°C for three days. The yield of that batch was improved noticeably, and subsequent batches confirmed this behaviour.

Disappointingly, this freeze-thaw assisted was not entirely new, but new to me, though previous attempts (published mere weeks after my revelation) using $Ti_3C_2T_x$ have involved ultrasonication steps,[242] a method I avoid so as to preserve the large flakes, which are associated with higher conductivity.[228]

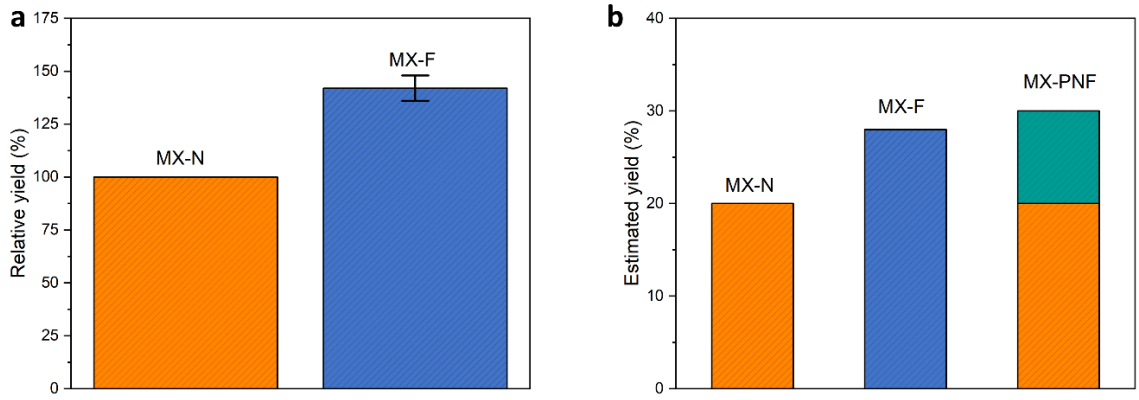

Figure 3.6: Yield from freeze-thaw assisted delamination. (a) Relative increase in yield for MX-F vs. MX-N, averaged over three batches. (b) Estimated overall yield for MX-N and MX-F batches, including further delamination from MX-N sediments to obtain MX-PNF ink.

When the yield of three batches was analysed, the freeze-thaw assisted delamination (FAD) showed an average increase of 42 ± 6%. This can be seen in Figure 3.6a, where FAD MXene (MX-F) is compared to batches which were refrigerated instead of frozen overnight (MX-N). This exceeds the previously reported increase for a single stage of freezing, at around 30%.[242] It should be noted however that their approach differs slightly in that they freeze a dilute dispersion of material as opposed to my freezing of the concentrated sediments. In Figure 3.6b, a batch was analysed to verify the effect of freezing delaminating additional multilayer material. Material was prepared from the size selected sediments of an MX-N batch by freezing overnight as before (MX-PNF). In this way, MX-PNF should be more or less only the flakes delaminated by FAD.

Overall yield of $Ti_3C_2T_x$ for MX-N and MX-PNF (30%) together slightly exceed that of MX-F (28%), though the additional agitation in preparing the final MX-PNF ink will also contribute to the yield. A figure of < 20%[243,244] yield is often quoted for MILD-etched MXene, though this has also been described as inaccurate by other authors,[245] and, for example, MILD-etched MXene with a microwave assisted delamination process achieved only 10% yield.[246] It should be noted that the yields presented in this chapter are estimated based on the ratio of the mass of delaminated MXene to the theoretical mass of $Ti_3C_2O_2$ which could be obtained from the initial mass of Ti_3AlC_2 MAX phase. This marks another deviation from the previously reported free-thaw delamination,[242] where the yield was estimated based on the ratio of the mass of delaminated MXene to the mass of MXene obtained after both etching and washing. That study reaches a yield of ~20% after one freeze/thaw step, and a maximum of ~40% after four steps. Given that material will be lost to etching, which, though "selective", cannot leave the Ti_3C_2 layers untouched, as well as lost during washing, it stands to reason that this will give an inflated yield compared to one calculated from the theoretical maximum. Additionally, while it would not be unreasonable to define a yield for the delamination process itself, in the context of MILD-etched MXene, where the intercalation and delamination processes unavoidably begin during etching and washing, I think it becomes somewhat disingenuous. Another study, using HF etching and hydrothermal delamination[245] defines their yield based on the mass of multilayer MXene obtained after etching and washing, and their delamination process achieves a yield of 74%, though this comes at the expense of conductivity, at only 405 S cm^{-1}. With all of this in mind, it becomes clear that the current literature on MXene yields is lacking in consistency, making it frustratingly difficult to draw direct comparisons

between different methods. Furthermore, there is simply a lack of literature overall. The nature of lab-scale production clearly disincentivises paying attention to the yield of the processes employed, though if MXenes are to ever become commercially viable, yields will certainly be of paramount concern.

Given that the MX-F and MX-PNF should contain flakes that were too large and/or thick to make it into the final MX-N ink, there may be appreciable differences in the size distributions of the dispersions. Figure 3.7 shows size distributions of 200 flake counts and some of the SEM micrographs from which they were obtained for each of MX-N (a, b), MX-F (c, d), and MX-PNF (e, f). The average diameter of MX-N flakes was determined to be 1.86 ± 0.93 µm, while increases were observed in both MX-F (1.99 ± 0.89 µm) and MX-PNF (2.16 ± 1.16 µm). This is good to see, especially given that these dispersions go through the same size selection process as MX-N, which will remove excessively large flakes. Visually, the distributions of both MX-F and especially MX-PNF diameters are much tighter than that of MX-N and imply more monodisperse inks.

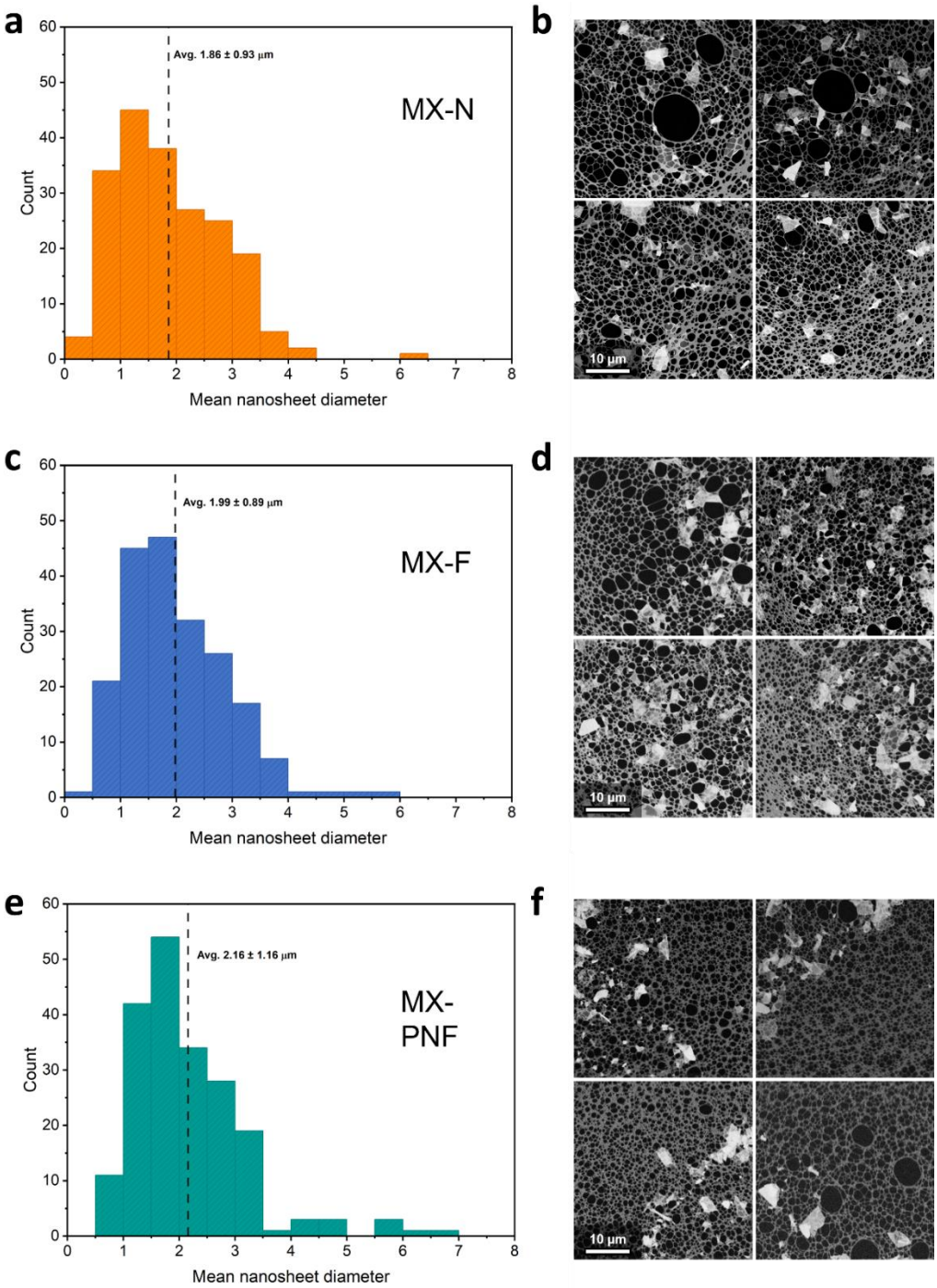

Figure 3.7: Size distributions and SEM micrographs of MX-N, MX-F and MX-PNF flakes. (a) Size distribution of MX-N flakes obtained from 200 counts, (b) ESB SEM micrographs of the regions measured. (c) Size distribution of MX-F flakes obtained from 200 counts, (d) ESB SEM micrographs of the regions measured. (e) Size distribution of MX-PNF flakes obtained from 200 counts, (f) ESB SEM micrographs of the regions measured.

Further differences between the MX-N, MX-F and MX-PNF inks are found when comparing filtered films prepared from them. Figure 3.8a shows the XRD of each film, with a clear shift in the (002) peak position for both MX-F and MX-PNF. The (002) reflection for MX-N appears at $2\theta = 7.083°$, while MX-F is shifted down to $2\theta = 6.947°$. This gives a slight increase in d-spacing from 12.47 to 12.71 Å for MX-F, increasing the interlayer spacing by 0.24 Å or just over 7%.

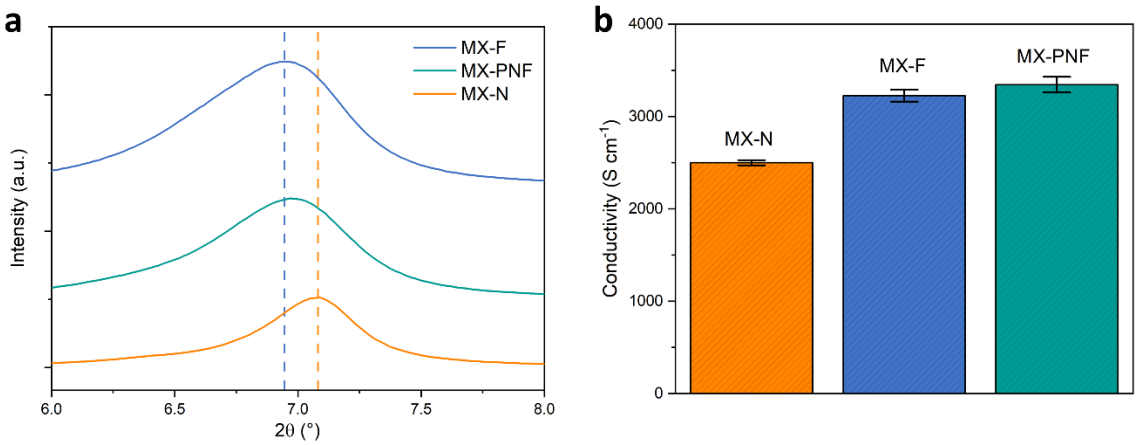

Figure 3.8: Crystallography and conductivity of MX-N, MX-F and MX-PNF films. (a) X-ray diffractograms of (002) reflections for each of MX-N, MX-F and MX-PNF, highlighting the increased d-spacing achieved using freeze-thaw assisted delamination. (b) Mean conductivity of MX-N, MX-F and MX-PNF films.

Figure 3.8b shows the DC conductivity for MX-N, MX-F and MX-PNF films. The DC conductivity, as expected, increases with the larger flakes present in the MX-F and MX-PNF inks to a maximum of 3345.5 ± 83.8 S cm^{-1}. This is middle-of-the road for $Ti_3C_2T_x$ films, however they were not subject to any of the post-synthetic treatments such as annealing in vacuum which can greatly improve conductivity though removal of intercalated water and formation of bonding between nanosheets.[39] Vacuum filtration is also known to be suboptimal for peak conductivity due to imperfect alignment of

nanosheets.[48] Finally, it is known that DC conductivity in MXene films has an inverse thickness dependence, and the filtered films presented in this chapter are between 14 and 15 µm thick. For example, freeze-thaw delaminated films dropped in DC conductivity nearly linearly from 10000 to 6000 S cm^{-1} when comparing 3 µm films to 8.5 µm films.[242] The highest reported value to date for MILD-etched $Ti_3C_2T_x$ is 15000 S cm^{-1}, this being obtained with highly aligned, blade cast films, annealed at 200° C and with a thickness of 214 nm.[48] As with the aforementioned freeze-thaw delaminated films,[242] these films also saw a precipitous drop in conductivity with increasing thickness, to around 10000 S cm^{-1} at a thickness of 2.4 µm. Taking these factors into consideration, the conductivity improvements measured for MX-F and MX-PNF should be considered indicative of a relative improvement compared to conventionally obtained MILD-etched MXene but should not be taken as absolute values to be compared without context.

3.4 Conclusions

To summarise the Chapter, high quality $Ti_3C_2T_x$ was synthesised from its precursor MAX phase, Ti_3AlC_2. The material was etched using a derivative of the MILD synthesis protocol, relying on the joint etching and intercalating properties of LiF in the presence of HCl. Dispersions and films of the final MXene were characterised using a variety of imaging, spectroscopy and crystallography measurements, and exhibit features typical of properly etched, high quality $Ti_3C_2T_x$.

The yield of the MILD synthesis was improved dramatically by a simple, single step freeze-thaw assisted delamination, increasing the mass of MXene flakes obtained by 42

± 6%. The average diameter and conductivity of freeze-thaw delaminated $Ti_3C_2T_x$ nanosheets was found to improve significantly versus the conventionally delaminated material.

While not used in the subsequent chapters for consistency's sake, it is my hope that the yields of our future MXene will be improved using this facile method, and that it may be leveraged for other MAX phases which are often more difficult to delaminate.

3.5 Experimental Methods

3.5.1 Preparation of $Ti_3C_2T_x$ Ink

$Ti_3C_2T_x$ was synthesized from its parent MAX phase through a variation of the minimally intensive layer delamination (MILD) method.[34,38] In a vented 40ml PTFE vessel, deionised water (15 ml) was added, followed by drop-wise addition of concentrated hydrochloric acid (45 ml, Sigma). To the resultant 9M HCl, LiF powder (4.8g, Sigma) was added, and the vessel was then placed in a mineral oil bath with stirring at 400 rpm using a magnetic PTFE stirrer bar for 10 minutes to fully dissolve the LiF and allow the temperature to stabilise. Ti_3AlC_2 MAX phase powder (3 g, Carbon-Ukraine ltd.) was then added in small additions to the vessel over a period of 30 minutes to avoid overheating of the solution. The solution was then left stirring at 400 rpm at 35°C for 24 hours to obtain the etched, multilayer $Ti_3C_2T_x$ MXene.

To wash the etchant, the contents of the vessel were transferred evenly into eight 50 ml centrifuge tubes and diluted to a total of 40 ml each with deionised water. The dispersion was then sedimented *via* centrifugation at 5000 rpm using a Thermo

Scientific Heraeus Multifuge X1 for 5 minutes, discarding the supernatant and repeating several times, until the pH of the supernatant had reached at least 6.5. To delaminate the washed multilayer MXene, the tube was sealed tightly and shaken vigorously by hand and vortex mixing for 30 minutes. The dispersion was then centrifuged at 1500 rpm for 30 minutes to sediment any multi-layer MXene or unreacted MAX phase. The supernatant containing delaminated MXene flakes was then collected. This dispersion was then centrifuged at 5000 rpm for 1 hour to sediment the delaminated MXene which was then redispersed to a concentration of approximately 30 mg/ml. Prepared inks were stored in 5 ml glass vials which were purged with nitrogen and filled completely with ink before sealing to avoid trapped oxygen. This is the procedure used to prepare and store MX-N and any other $Ti_3C_2T_x$ used in this Thesis unless otherwise stated.

3.5.2 Determining the Concentration of $Ti_3C_2T_x$ Dispersions

To accurately determine the concentration of the MXene dispersions, 100 µl was transferred to a small glass vial and diluted with a 1:1 (v/v) ratio of deionised water and absolute ethanol (Fisher) before being filtered using a pre-weighed 0.25 µm pore nitrocellulose filter membrane (Millipore VSWP) and vacuum filtration flask. The vial and sides of the funnel were washed down with additional 1:1 deionised water and absolute ethanol. Once the filtration was complete the membrane and MXene filtride were dried overnight in a vacuum desiccator and then weighed to obtain the concentration.

3.5.3 Freeze-Thaw Assisted Delamination of $Ti_3C_2T_x$

The preparation of FAD MXene, denoted MX-F is identical to MX-N above until the end of the washing steps. Instead of proceeding with the 1500 rpm centrifuge to sediment multilayer material, the sediments from the final wash were purged with nitrogen and sealed before placing in a freezer at -20°C overnight. The sediments were then allowed to thaw at ambient temperature before redispersing in 40 ml deionised water per centrifuge tube as before. The size selection and final ink preparation steps were then the same as for MX-N.

MX-PNF was prepared using the sediments removed during the 1500 rpm centrifuge step for MX-N. They were purged and sealed as with MX-F above and then frozen and treated identically as before. In this way, the resultant MX-PNF flakes should consist only of flakes which were not successfully delaminated by normal means.

3.5.4 Electron Microscopy

Characterisation with SEM was performed using a Zeiss Ultra Plus (Carl Zeiss) microscope fitted with a Gemini column, SE detector and ESB detector. The typical acceleration voltage used was 1.5 kV. EDX spectra were acquired using the EDAX detector at an acceleration voltage of 10 kV.

The delaminated MXene flakes were imaged by TEM (FEI Titan) at 300 kV. Dispersions were diluted to 5 µg ml^{-1} and drop cast on lacey carbon copper grids (Pelco, USA). EDX mapping was performed using the EDAX detector of the TEM and superimposed on HAADF images.

3.5.5 Size Distributions

In all cases, dispersions were diluted to a concentration of roughly 5 µg ml^{-1} and drop cast on lacey carbon TEM grids (Ted Pella). A Zeiss Ultra SEM at 1.5 kV was used to image the grids using the energy selective backscattering (ESB) detector with a retarding voltage of 975 V to enhance contrast between thin $Ti_3C_2T_x$ flakes and the ~ 30 nm thick lacey carbon. The area of 200 flakes were calculated using ImageJ and the dimensions, D, estimated as the diameter of a circle with equivalent area such that:

$$D = 2\sqrt{\frac{A}{\pi}} \tag{52}$$

Where A is the area of each flake. Uncertainty given as the standard deviation of the 200 measurements.

3.5.6 X-ray Diffraction Measurements

Filtered films of MX-N, MX-F and MX-PNF were characterized with XRD, using a Bruker D8 Discovery X-ray Diffractometer in θ/2θ configuration, in the range of 3−75 °, at 2° min^{-1}. D-spacing was calculated from the $Ti_3C_2T_x$ (002) reflection according to the formula for Bragg's law, Equation (36).

3.5.7 Optical Spectroscopy

UV-Vis extinction spectra were obtained for dilute (10 µg ml^{-1}) $Ti_3C_2T_x$ dispersions using a spectrophotometer (Biochrom Libra), scanning from 900 to 300 nm.

Raman spectra for $Ti_3C_2T_x$ filtered films were acquired using a WITec Alpha 300R with a 633 nm He-Ne laser source and 1800 lines/mm grating.

3.5.8 Four-point Conductivity Measurements

Filtered films of MX-N, MX-F and MX-PNF were tested using the four-point method to negate contributions from contact resistance by having independent sources of potential and current. An Ossila four-point measurement station was used. For each film, 25 measurements were acquired to obtain a mean conductivity value and standard deviation. The thickness of each film was determined from the average of five digital micrometer (Mitutoyo) measurements.

3.6 Acknowledgements

I would like to thank Ahin Roy for the HRTEM image shown in this chapter.

4 AEROSOL JET PRINTED 3D MXENE STRUCTURES

This Chapter concerns a demonstration of the capabilities of aerosol jet printing in the context of microengineering and microelectronics. Binder-free, aqueous MXene inks are printed in a wide array of 3D geometries and high areal capacitance $Ti_3C_2T_x$ microsupercapacitors are realised by augmenting planar electrodes with 3D structures.

4.1 Introduction

In recent years the demand for energy storage has seen tremendous growth across the globe and across an enormous range of applications, from grid storage down to microelectronics. At smaller scales, such as portable and Internet of Things (IoT) devices, microsupercapacitors may present a solution to the requirement for compact energy storage, especially considering the increasing abandonment of wires for both power and data transfer. Specifically, directly incorporating microsupercapacitors into the structure of a device through printing techniques is very appealing from a design, prototyping, and manufacturing point of view. Recently, MXenes have emerged as a promising family of materials for energy storage, with much of the work surrounding supercapacitors based on $Ti_3C_2T_x$. Nanoflakes of this material combine a metallically conductive titanium carbide core and a surface functionalised by polar and

pseudocapacitive surface groups such as F, O and OH – denoted T_x. Conductivity can reach as high as 15000 S cm^{-1} for the previously discussed annealed film with a thickness of 214 nm,[48] and specific capacitance can reach as high as 450 F g^{-1} for a 90 nm thick film.[247] These properties make it an ideal material for supercapacitors. The hydrophilic nature of $Ti_3C_2T_x$ allows for facile creation of aqueous dispersions, the compatibility of which naturally leads to increased efforts in printing electrodes and current collectors for microsupercapacitors.[248–251] However, in most of these studies, only planar devices were printed. This is an issue because robust control of the electrode architecture is needed, as excessively dense and/or thick electrodes compromise both rate performance and specific capacitance, due to long ion diffusion pathways inhibiting fast charge transfer and restriction of the specific surface area.[34] To address the ion transport and capacitance issues of more conventional, dense, 2D printed films,[249] recent studies have demonstrated 3D printing of MXene-based supercapacitors, though these have been relatively large and achieved using composites [252] or post-processing steps such as freeze drying.[253] Changing the geometry of the electrodes into a 3D shape, rather than a planar one, may increase the areal capacitance of a device without requiring more active material. Research on microsupercapacitors with 3D structured electrodes has mainly focused on conventional fabrication technologies, such as lithography.[254] Though the field of additive manufacturing has shown that perhaps 3D printing of nanoparticle-based inks can be a useful alternative.[253,255,256]

In this chapter, I will show that aerosol jet printing of aqueous $Ti_3C_2T_x$ inks can be used to fabricate high aspect ratio 3D structures up to 1 mm in height and with feature sizes as small as 20 µm, without the aid of supports, binders, or post-processing and in a wide range of geometries such as walls, pillars, and pyramids. 3D micropillars will be used to

augment planar microsupercapacitor electrodes to greatly increase performance of the devices.

4.2 Aerosol Jet Printing of Binder-Free MXene Microstructures

Aerosol-jet printing results in a densified column of aerosolised ink that is stable over up to several millimetres while jetted towards the substrate. The focussing enables high-resolution printing with feature sizes as small as 20 µm. The most important aspect in the scope of this work, however, is the size of the droplets within the aerosol, which enables almost instant drying when the droplet impinges on the substrate. By carefully tuning the process parameters to allow rapid drying of the droplets but minimal in-flight drying of nanosheets, 3D structures can be printed. Note that both overly wet and overly dry deposition will have a detrimental effect. If the droplets contain too much water or are simply too numerous, a thick liquid film will be formed before drying which will spread on the substrate making 3D build up impossible. On the other hand, if the droplets dry in-flight, the capillary forces of the shrinking droplets result in crumpled MXene sheets, which cannot be used to build up stable 3D features either.[257]

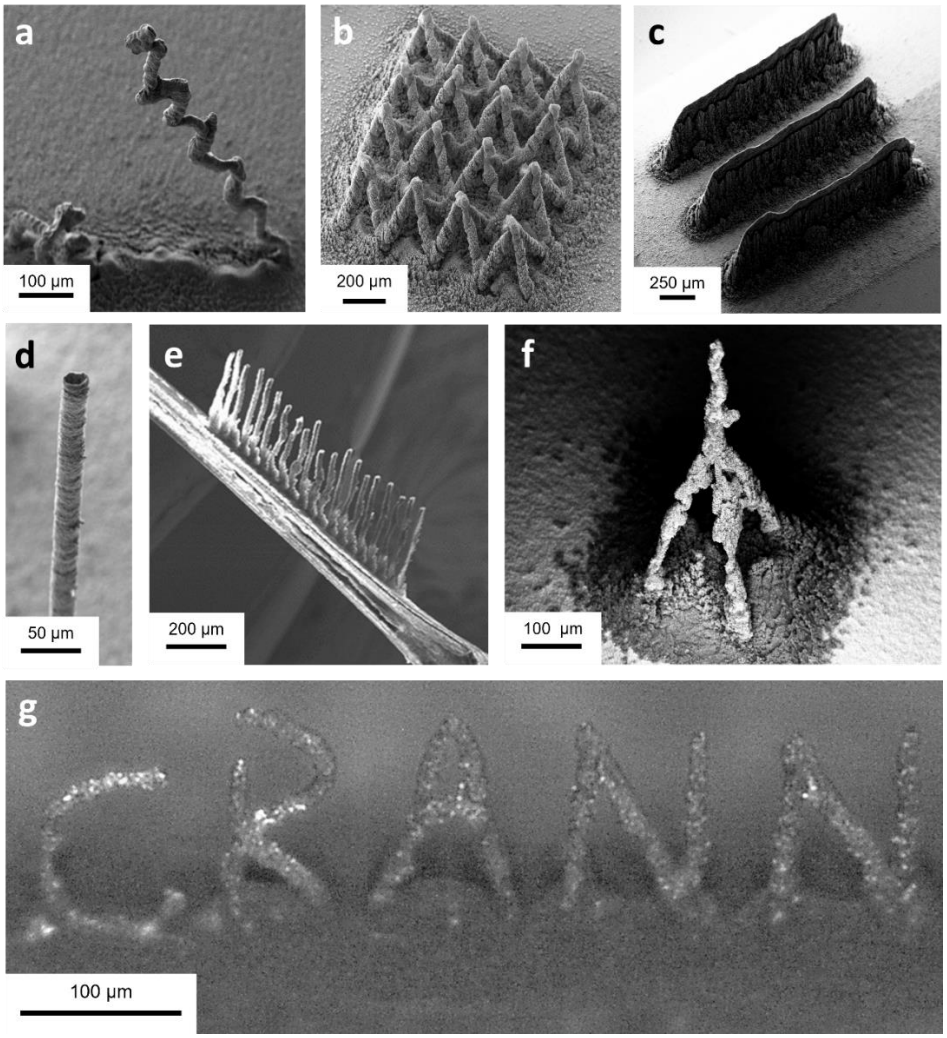

Figure 4.1: Micrographs of example structures printed with binder-free MXene inks. (a) Stair-stepped structure with near-horizontal overhangs ~0.5 mm in total height. (b) Array of pyramidal structures comprised of connected ~45° $Ti_3C_2T_x$ micropillars. (c) $Ti_3C_2T_x$ walls ~0.5 mm tall realised from 1000 repeated layers. (d) MXene vertical micropillar with uniform profile of ~20 µm in diameter. Total height of ~600 µm giving an aspect ratio of 1:30. (e) Micropillar array printed directly onto a human hair, demonstrating the high resolution and repeatability that AJP can achieve. (f) MXene "µ-Eiffel Tower", showcasing both AJP's geometric flexibility and its creator's whimsy. (g) Vertical "µ-billboard" for our institute, CRANN. It should be noted that all the structures were printed in a top-down manner, perpendicular to the substrate, with no tilting of the print head or build plate. Any overhanging features were printed solely with slow lateral movements of the stage.

AJP can be used to create a range of structures limited only by the creativity of the user and the cost of tool time. Presented in Figure 4.1 is a selection of prints realised with the Optomec AJ 300 system. Figure 4.1a is a stair-stepped structure printed by alternating dwelling and slow lateral movements. The lack of any supports and single point of contact with the base demonstrates the mechanical stability of the $Ti_3C_2T_x$ structures, and clearly strong flake-flake interactions. Figure 4.1b is an array of 45° $Ti_3C_2T_x$ micropillars forming an array of pyramids. These were printed according to a pattern wherein the aerosol jeet was slowly (0.1 mm s^{-1}) brought towards the centre of each pyramid. The rapid build-up of material resulting in a freestanding diagonal pillar. Figure 4.1c are walls produced by a more conventional layer-by-layer build-up. They consist of 1000 ~0.5 µm thick MXene layers, forming a 0.5 mm tall wall. It can be seen that the profile of the walls is not perfectly straight, with slight overspray resulting in a wider base. Figure 4.1d is a MXene micropillar, ~20 µm in diameter and with a total height of ~600 µm, giving it an extremely high aspect ratio of 1:30. The profile of the pillar is extremely uniform, though the apex of the structure is dished, likely an artifact of the coffee-ring effect as the topmost region dried. Figure 4.1e is an array of micropillars printed directly onto a human hair. This serves as an easily understood example of not just the minute scale of these structures, but also the overall accuracy of the tool, enabling precision deposition when properly calibrated. Figure 4.1f shows a MXene "µ-Eiffel Tower", printed in a similar fashion to Figure 4.1b. Finally, Figure 4.1g shows a vertical "µ-billboard", demonstrating the range of arches and overhanging structures that can be produced from additive-free MXene dispersions.

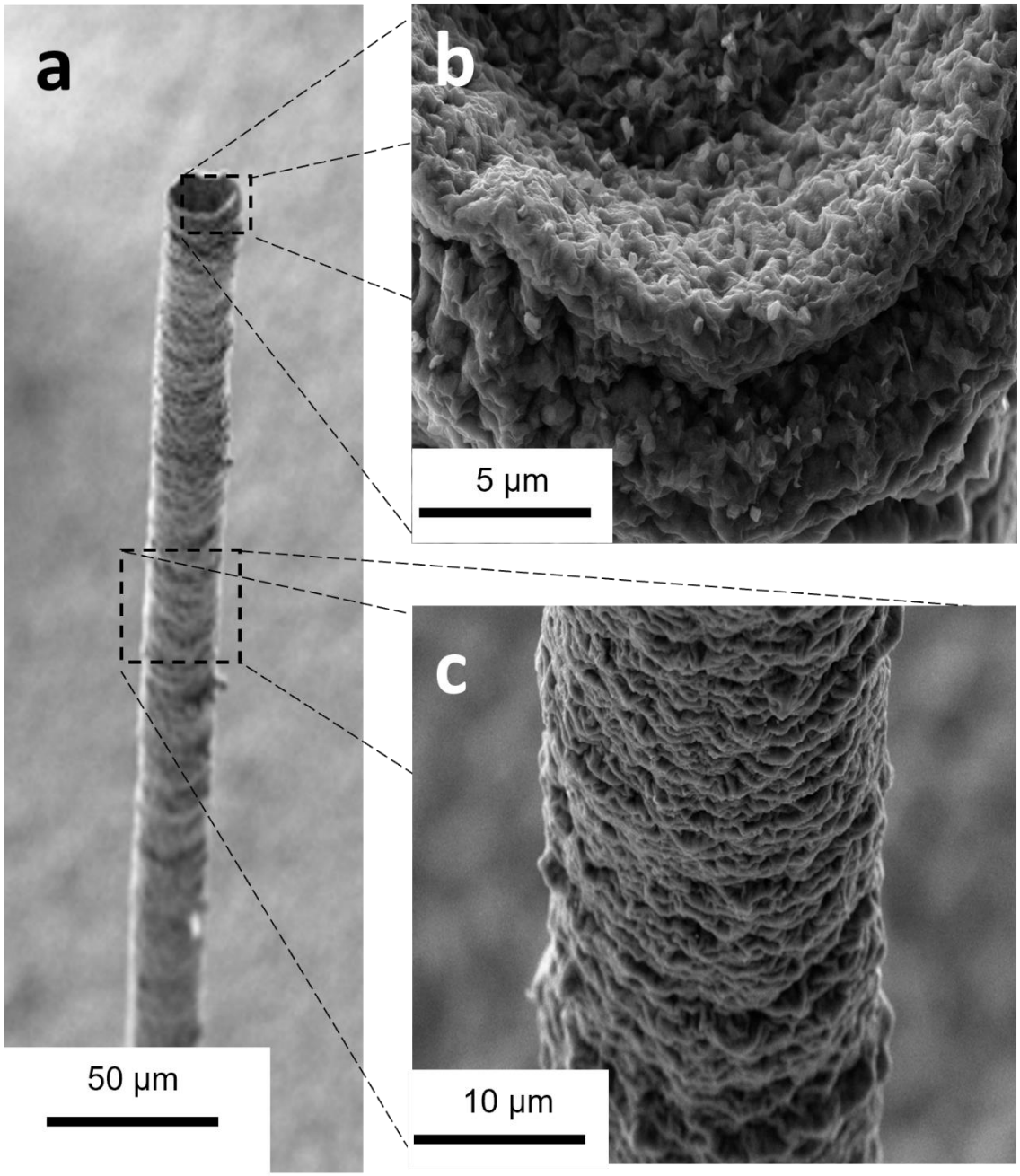

Figure 4.2: Detail views of MXene micropillar. (a) Uniform micropillar, realised by extended dwelling of the aerosol jet. (b) Edge of the dished apex of the pillar, likely an artifact of coffee-ring drying of the ink. Individual MXene flakes easily visible. (c) Micropillar profile, with prominent flake edges, implying an approximately horizontal orientaton of the MXene sheets.

The morphology of the printed structures can be quite beautiful as shown in Figure 4.2. The high magnification SEM image of the dished apex in Figure 4.2b shows very clearly the outline of the individual MXene flakes which form the rim, curving over from vertical. Figure 4.2c shows the profile of the pillar, its surface comprised of angled flakes resembling shingles or scales. The very clear appearance of edges along the entire profile implies that the structure should be easily infiltrated by ions, diffusing rapidly along the basal plane of each flake.

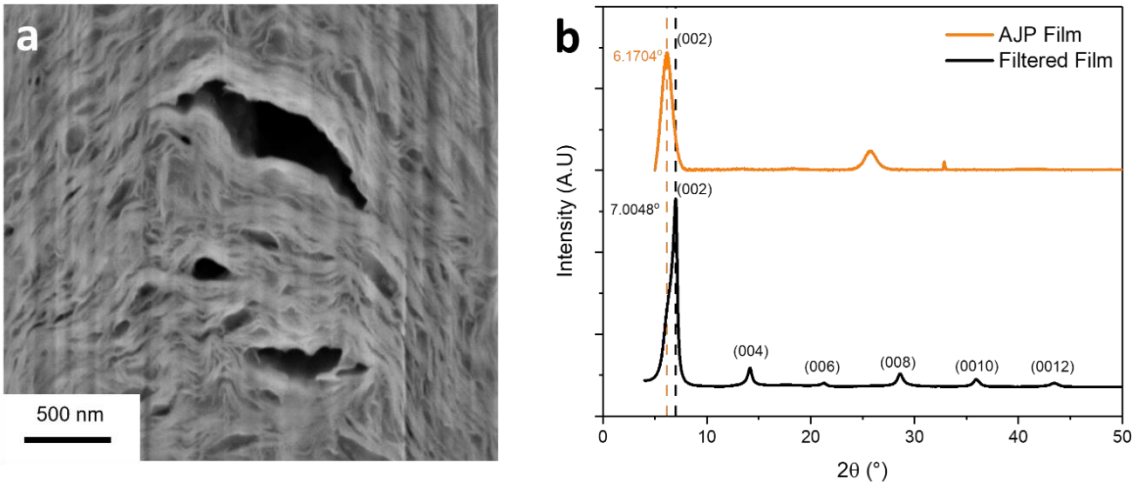

Figure 4.3: Internal structure of AJP MXene. (a) FIB cross-section of $Ti_3C_2T_x$ micropillar. The internal porosity is of particular interest in energy storage applications. Note the increasingly horizontal flake orientation towards the centre. (b) X-ray diffractograms of a filtered $Ti_3C_2T_x$, film and AJP $Ti_3C_2T_x$ film. The absence of higher order reflections implies a more disordered internal structure in the AJP film. The d-spacing is increased over 50% relative to filtered film from 3.2 Å to 4.9 Å (based on dry multilayer spacing of 9.4 Å).[230]

The angled flakes that form the surface of the micropillar were revealed in cross-section by focused ion beam (FIB) milling and SEM imaging as seen in Figure 4.3a. The internal structure is punctuated by voids and has an overall quite porous appearance, reinforcing the previous observations regarding ion transport and appearing very

promising for energy storage applications such as microsupercapacitors. The somewhat disordered internal structure of AJP MXene features is further revealed by XRD, detailed in Figure 4.3b. The (002) reflection is broadened considerably with respect to a filtered film of the same $Ti_3C_2T_x$, and the higher order (00*l*) reflections have vanished. Of note here also is the appearance of a reflection at $2\theta = 25°$, corresponding to anatase TiO_2. As this sample was printed after close to three days of printing, it is not surprising that the ultrasonication resulted in the partial oxidation of some of the nanoflakes. The constant nitrogen carrier gas flow prevents the egregious oxidation one might expect after three days of bath sonication, but clearly there is degradation occurring. To mitigate this issue, only freshly delaminated ink was used to produce the samples detailed in the electrochemical measurements to follow. Overall printing time was also kept to a minimum and ink not used for more than one day of printing. It's possible that more stable MXene produced from Al-rich MAX phase which has recently been published will better avoid this degradation.[231]

4.3 Aerosol Jet Printing of Mass-Equivalent Microsupercapacitors

To investigate what effect (if any) that 3D architectures would have on the performance of microsupercapacitors, it was decided to print devices of equal active area back-to-back, with overall print time equalised such that the pair would be of equal mass. These proof-of-concept devices consisted of an identical underlying electrode and current collector which would be then decorated with either an additional planar active layer or 3D active layer of equal mass. The schematics shown in Figure 4.4a and e correspond to

the design of the 2D, planar device and 3D device, respectively. The 3D device is decorated with an array of micropillars, formed by dwelling in the same spot for a set period of time.

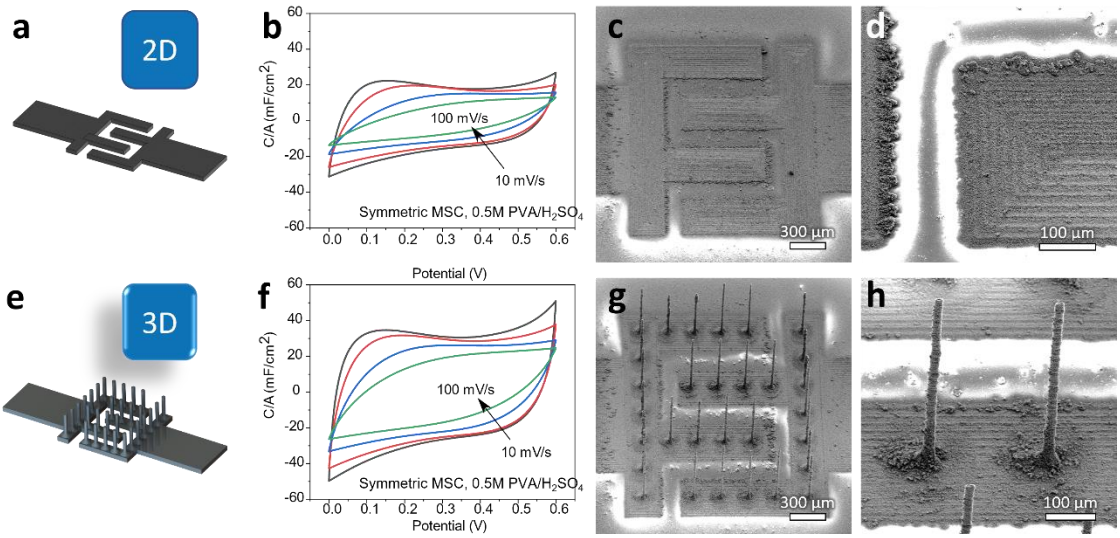

Figure 4.4: Schematic drawings and a direct comparison by SEM and CV measurements of a planar device and an equal-size, equal-mass device with 3D micropillars. (a) Planar device schematic. (b) Planar device CVs. (c) Top-down view of planar device active area. (d) Detail view of planar device electrode surface, note the linear artifacts from the rastering of the aerosol jet. (e) 3D device schematic. (f) 3D device CVs showing approximately 30% capacitance uplift (g) Top-down view of 3D device active area. (d) Detail view of the 3D micropillars, noting their uniform height.

The CVs presented in Figure 4.4b and f show the clear increase in capacitance for the 3D decorated electrode versus 2D. At 10 mV s^{-1} the 3D device has an areal capacitance over 30% greater than the 2D device. This despite their mass being as close to equal as reasonably possible. Figure 4.4c, d, g, and h show SEM micrographs at low and high magnification of the devices overall and the structure of their electrodes. The rationale for the equalisation of mass through identical print parameters and print time was as a result of having no way to directly measure the mass flow of the AJP process, and the

difficulty in accurately weighing printed devices with masses in the low µg range at most, making direct calculation of gravimetric capacitance impractical.

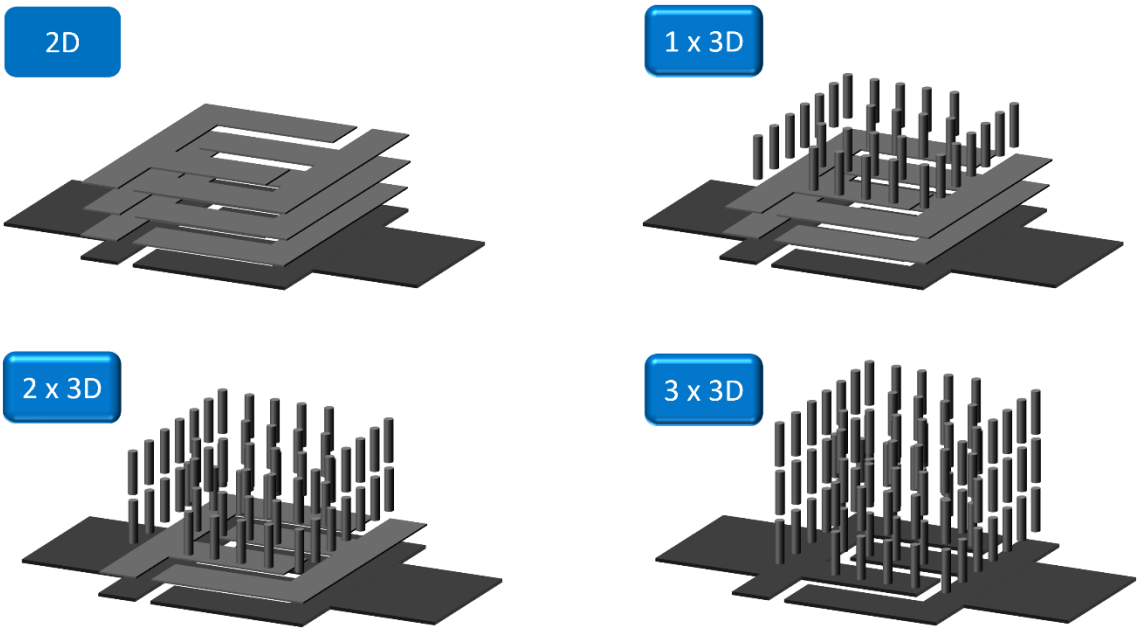

Figure 4.5: Schematic of the layers printed to test the effect of additional planar and/or 3D layers in equal area and equal mass devices. One layer for each device printed sequentially, reversing order every 4 layers to mitigate influence of pressure drift.

With encouraging initial results, it was decided to see if the scaling in areal capacitance would continue for additional layers. As before, interdigitated underlying electrode patterns were used which would then be decorated with a combination of planar or 3D layers; the 3D layers consisting of micropillars distributed along the fingers of the electrodes. Four different device types were produced, shown schematically in Figure 4.5. In each case, the decorating layers (light grey) were printed such that the overall time would be equal, resulting in a set of devices with equivalent mass loading. As detailed in Section 2.2.1, process drift can occur due to material build up in the mist tube. To combat drift while printing of a set of four devices, the order of printing was

reversed after each layer, compensating for any small change in deposition rate as time goes on.

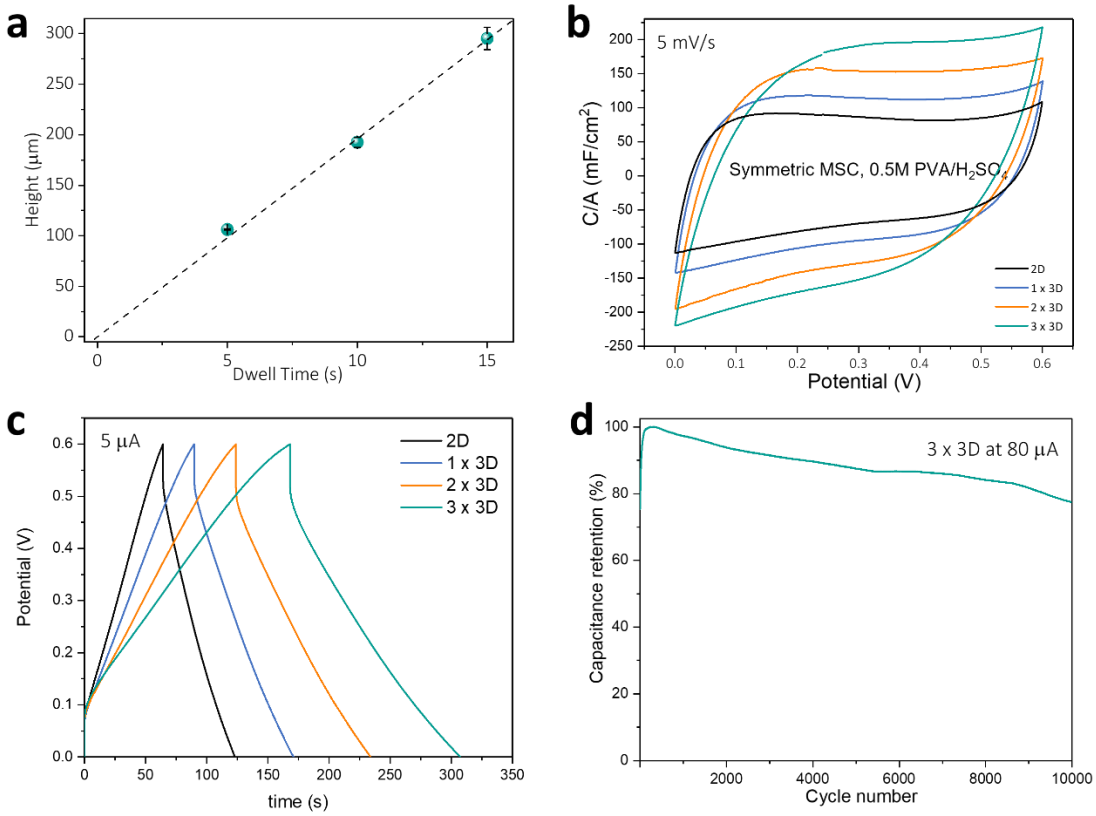

Figure 4.6: Scaling of micropillar height and electrochemical performance. (a) Dependence of pillar height on print head dwell time. Heights averaged over 5 adjacent pillars. The build-up rate was found to be approximately 19.6 µm s^{-1} with a highly linear scaling. (b) CVs of four equal mass devices at 5 mV s^{-1} with increasing proportion of 3D vs. 2D layers. Areal capacitance is found to increase by over 30% for each 3D layer in place of a 2D layer. (c) Charge/discharge curves for the same four equal mass devices at a current of 5 µA. (d) Long-term GCPL cycling of the 3 x 3D layer device (300 µm micropillars), note the capacitance retention of 80% over 10000 cycles at a current of 80 µA with respect to the maximum capacitance at cycle ~500.

The average height of the 3D micropillars produced was measured to assess the consistency of the above approach. Each 3D layer corresponded to a dwell time of 5 s.

The height scaling of the micropillars is shown in Figure 4.6a, where a very linear relationship is observed. The dwell times of 5 s, 10 s and 15 s correspond to the pillars for the 1 x 3D, 2 x 3D, and 3 x 3D devices, respectively. It was found that the rate of build-up was approximately 19.6 µm s^{-1}, giving pillars of 100 µm, 200 µm, and 300 µm height, respectively. The electrochemical performance of the four devices is shown in Figure 4.6b, where the same scaling of over 30% is seen with each increase in the proportion of 3D structures. This results in an areal capacitance for the 3 x 3D device 97% higher than that of the planar device, or 138 mF cm^{-2} at equivalent mass. Similar scaling is seen in the GCPL curves presented in Figure 4.6c. The 3 x 3D device also showed impressive cycle stability, retaining 80% of its capacitance after 10000 cycles at 80 µA. It is reasoned that the enlarged accessible surface area and fast ion diffusion into the pillars of the 3D devices is the main driver for their increased performance.

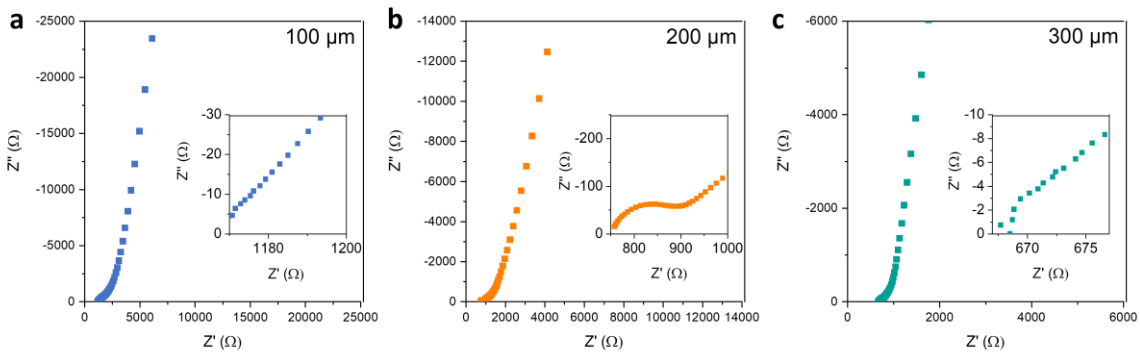

Figure 4.7: Nyquist plots showing the electrochemical impedance spectroscopy (EIS) data for (a) 100 µm, (b) 200 µm and (c) 300 µm micropillar devices. The insets show detail of the high frequency region. ESR is equal to 1170 Ω, 757 Ω and 667 Ω, respectively. Note the semi-circle in the 200 µm sample, probably indicating increased impedance at the electrode/current collector interface, but the absence of such an effect in the other two.[258]

The EIS plots in Figure 4.7a, b, and c represent the 1 x 3D, 2 x 3D and 3 x 3D devices, respectively. Here it can be seen that the ESR is reduced as the pillar height increases, to a minimum of 667 Ω for the 3 x 3D (300 µm) device. From the EIS curves and the approximately rectangular CVs with only slight humps introduced by redox peaks it can be concluded that the AJP microsupercapacitors are operating predominantly as EDLCs.

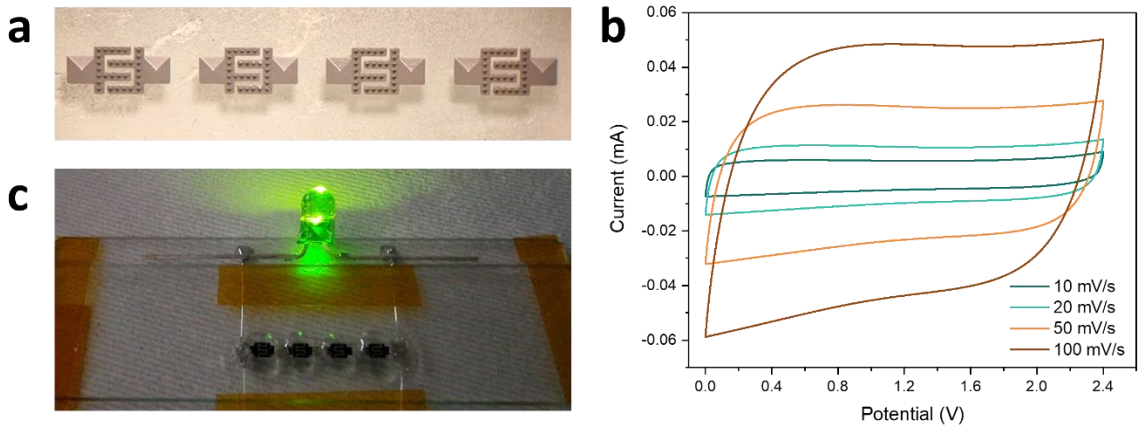

Figure 4.8: Array of four 3 x 3D microsupercapacitors (300 µm height) in series. (a) optical microscope image of the devices. (b) CVs at 10 – 100 mV s^{-1} for the array, operating with a potential window of 2.4 V. (c) Image of the charged microsupercapacitors lighting an LED.

To demonstrate the practical feasibility of 3D AJP microsupercapacitors, an array of four 3 x 3D devices were printed and assembled in series. An overview of the devices is seen in Figure 4.8, and their CV profiles in Figure 4.8. The devices can be successfully cycled up to 2.4 V, sufficient to power an LED connected to the array.

Wishing to better understand the intrinsic performance which may be achieved in AJP microsupercapacitors, three-electrode measurements were carried out on small electrodes decorated with a dense array of micropillars. The pillars were of 100 µm height, decorating an electrode of 1.5 x 0.3 mm. The intrinsic performance of such devices were quite remarkable, as can be seen in Figure 4.9. The pronounced redox

peaks which appear in Figure 4.9a at negative potentials result in a large pseudocapacitance at low scan rates. Figure 4.9b shows the GCPL profiles at large areal current densities, from 0.33 to 1.33 A cm^{-2}.

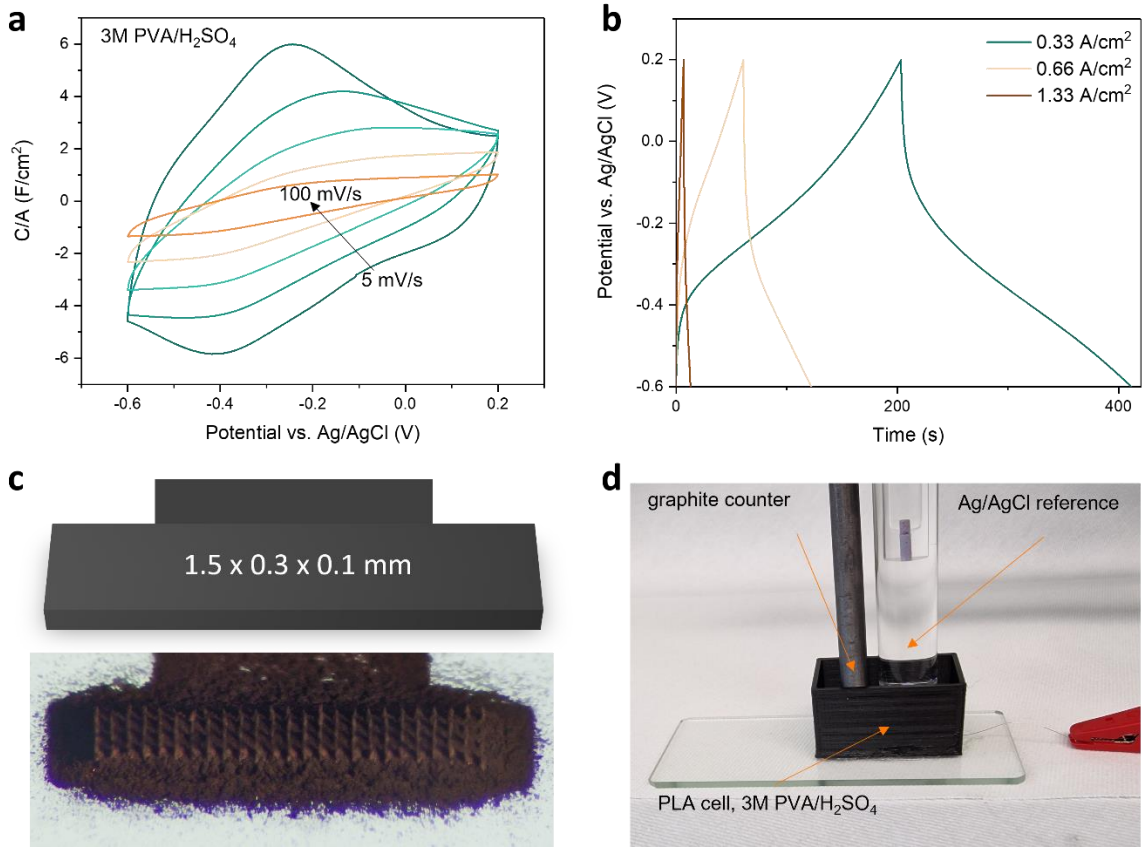

Figure 4.9: Performance and configuration of high density micropillar array electrode. (a) CVs from 5 - 100 mV s^{-1} for a high density electrode, note the pronounced redox peaks at low scan rates. (b) Charge-discharge curves for the electrode at current densities from 0.33 to 1.33 A cm^{-2}. (c) Schematic and optical microscope image of a high density micropillar electrode which occupies a volume of 0.045 mm^3. (d) Three-electode setup using an FDM printed polylactic acid (PLA) cell to contain the 3M PVA/H_2SO_4 electrolyte.

A schematic detailing the area described by the electrode is presented along with an optical microscope image of the electrode itself in Figure 4.9c. The experimental setup including FDM printed cell is shown in Figure 4.9d. The headline figures for the high

density of micropillars device are an areal and volumetric capacitance of 3.47 F cm^{-2} and 347 F cm^{-3} respectively at 5 mV s^{-1}. These represent some of the highest values yet reported for 3D printed supercapacitors, MXene or otherwise.[259]

4.4 Conclusions

The structures described in this Chapter are demonstrated the first direct 3D printing of additive-free aqueous MXene inks on the micro-scale. They are unprecedented in the field of MXene research, considering their geometric variety, self-support of overhangs, robustness, and size. This approach made no use of any post-processing techniques and devices were able to be tested directly after production. 3D structures were used to decorate microsupercapacitors resulting in symmetric devices with high areal capacitance of up to 138 mF/cm^2 at 5 mV/s. These devices were compared to devices with varying proportions of 3D and 2D features showing an increase of 97% in areal capacitance for the 3D devices when compared to 2D devices of equal mass. Three-electrode measurements of high density micropillared electrodes resulted in exceptional values for areal and volumetric capacitance of 3.47 F cm^{-2} and 347 F cm^{-3} respectively at 5 mV s^{-1}.

Overall, this technique offers the possibility of directly integrating 3D MXene microsupercapacitors into compact electronic devices. For instance, 3D microsupercapacitors could be printed on the inside of a device housing, even onto a non-planar surface, as the direct printing method is non-contact and largely substrate-agnostic. I believe that this technique has potential to be employed to help exploit the outstanding properties of MXene microsupercapacitors further in future.

4.5 Experimental Methods

4.5.1 MXene synthesis

$Ti_3C_2T_x$ MXene was synthesised according to the variation of MILD synthesis detailed in Section 3.5.1.

4.5.2 Aerosol Jet Printing

An AJ 300 System (Optomec, USA) aerosol jet printer was employed for all prints. Prior to printing, MXene dispersions were diluted with deionised water to a concentration of 10 mg ml^{-1}. Note that AJP is compatible with higher concentration and higher viscosity inks, however, we obtained best repeatability of our results with diluted inks. During the atomisation, the concentration of the ink within the atomizer slowly rises, as not 100% of the solid loading is transferred into the air-suspended droplets. Therefore, working with a highly concentrated ink reduces the long-term stability of the process. As discussed in Section 2.2.1, using the solvent bubbler can also partially mitigate this effect. 2 ml of the diluted ink were used at a time, the ultrasonic atomizer was temperature controlled and kept at 10 °C and the atomisation current was set to approximately 0.8 A. The 150 µm diameter nozzle was used with carrier and sheath gas flow rates being ~25 +/– 5 SCCM and ~45 +/– 5 SCCM, respectively. Due to variation of environmental conditions (ambient temperature, pressure, humidity), the flow rates have to be adjusted slightly day-to-day. The bubbler was used to moisturise the carrier gas before entering the vial.

Electrodes and current collectors for planar interdigitated microsupercapacitors were printed onto hydrophilized glass slides (Matsunami Glass, USA) and subsequently augmented with pillars varying in height. To ensure a constant mass loading of devices, within one printing session all machine parameters and the total print time of the devices were kept constant. Pillars were printed by dwelling over one location for 5 s, 10 s and 15 s, resulting in pillar heights of 100 µm, 200 µm and 300 µm, respectively. The raster speed for both initial underlying planar electrodes was 1 mm s^{-1} and for additional planar layers compensating for pillars it was 0.83 mm s^{-1}. In this way, the total print time per layer additional layer was kept at a constant 165 s.

4.5.3 Preparation of H_2SO_4 Gel Electrolyte

The semisolid electrolyte was prepared by adding PVA (10 g) to deionised water (100 ml), stirring at 400 rpm and at 85°C for 30 minutes until a clear, homogenous gel was obtained. The gel was allowed to cool fully to room temperature before the drop-wise addition (under stirring) of concentrated H_2SO_4 (30 g). The stirring was continued at ambient temperature for 1 hour to obtain a homogenous 0.5M PVA H_2SO_4 gel electrolyte.

4.5.4 Device Preparation

Symmetric microsupercapacitors were created from the AJP electrodes above by first coating a small quantity of silver conductive paint (RS Pro) onto the current collector of each electrode. While still wet, a length of 0.1 mm silver wire was inserted into the

paint and allowed to dry in a vacuum desiccator for one hour. Once dry, silicone varnish was carefully applied to the silver paint and current collector to insulate them from the electrolyte. 0.5M PVA H_2SO_4 gel electrolyte was carefully applied as a single droplet to the active area of each device, before coating the device with silicone conformal coating to inhibit evaporation.

4.5.5 Electron Microscopy

Characterisation with SEM was performed using a Zeiss Ultra Plus (Carl Zeiss) microscope fitted with a Gemini column, SE detector and ESB detector. The typical acceleration voltage used was 2 kV.

4.5.6 Electrochemical Characterisation

All electrochemical measurements were carried out with a VMP-300 potentiostat (BioLogic S.A.). A potential window of 0 to 0.6 V was chosen for the measurements symmetric microsupercapacitor measurements, which consisted of cyclic voltammetry (CV) from 2 mV s^{-1} to 100 mV s^{-1}; galvanostatic cycling with potential limitation (GCPL) with current density of 5 µA; potentiostatic electrochemical impedance spectroscopy (PEIS) from 10 mHz to 100 kHz, and long term GCPL for 10000 cycles at a current of 80 µA.

To power an LED, four symmetric devices were printed in series and cycled to 2.4 V at 10 to 100 mV s^{-1} before connecting to the LED circuit.

Three-electrode measurements of high areal capacitance electrodes were performed with the AJP electrode as the working electrode, a graphite rod as the counter electrode, and an Ag/AgCl reference (SI Analytics). The electrolyte used was the same 0.5M PVA H_2SO_4 gel. A potential window of -0.6 to 0.2 V was chosen for the measurements, which consisted of CV from 5 to 100 mV s^{-1} and GCPL with current density from 0.33 to 1.33 A cm^{-2}.

Note that no further postprocessing between printing and preparing for electrochemical characterisation was performed.

4.6 Acknowledgements

I would like to thank Matthias Kremer for the printing and imaging of several of the MXene structures detailed in this chapter, and Megan Canavan for FIB-milling of the AJP micropillars.

5 TEMPLATED MXENE THIN FILM 3D NETWORKS

The pseudocapacitive nature of MXenes enables much higher energy and power densities compared to common EDLC materials. However, to create high performance MXene supercapacitors, their properties need to be translated from the nano- to the macro-scale, without limiting mass and charge transport within the electrode. In this Chapter, I present a method to fabricate hierarchical electrodes from $Ti_3C_2T_x$ nanosheets that facilitates the formation of thin films (between ~70 nm and ~220 nm) in a macroscopic (up to several cm^3), highly porous framework. By tailoring both the micro- and nanostructure of the framework, high performance, macroscopic electrodes are produced, with a tremendous combination of gravimetric, areal, and volumetric capacitance.

5.1 Introduction

The global appetite for energy storage is growing at an astounding rate,[260] the often-conflicting goals of sustainability and economic growth being the key drivers. As the prevalence of portable electronics, EVs, and intermittent energy sources such as wind and solar increases, so too does the demand for efficient short- and long-term energy storage. While lithium-ion batteries offer energy densities in excess of 300 Wh kg^{-1}, [261]

their slow, diffusion-limited charge storage, limited cyclability [262] and reliance on strategically valuable lithium make them unsuitable for many applications that require high power for limited duration. Conversely, supercapacitors, typically EDLCs, store charge through physisorption of ions on the surface of the electrode, a kinetically fast process in contrast to intercalation in batteries, granting them high power density and cycle stability at the expense of energy density.[6] Carbon-based EDLCs have therefore shown promise in high-power and high-stakes applications, such as kinetic energy recovery,[263] wind turbine power smoothing [264] and blackout/brownout protection for electronics.[265] Higher energy density would expand the possible use cases for supercapacitors, and this may be achieved through the adoption of pseudocapacitive materials - those which are characterized by fast, surface-confined faradaic charge transfer. Metal oxides such as RuO_2, MnO_2, and Fe_3O_4 are prototypical examples, but suffer from low electronic conductivity with the exception of RuO_2, which is prohibitively expensive.[266]

In recent years, MXenes have shown great promise as pseudocapacitive materials.[34,267,268] However, pitfalls lie in the structure of the electrodes themselves. Dense films of $Ti_3C_2T_x$ such as rolled MXene clay [34] exhibit excellent volumetric capacitance and gravimetric capacitance (900 F cm^{-3} and 245 F g^{-1} respectively at 2 mV s^{-1}), but poor high-rate performance. Dense films typically result in self-restacked layers leading to long diffusion pathways which greatly inhibit ion transport, restricting both the response time and accessible surface area of the electrode.[269] It has been demonstrated, that the gravimetric capacitance and rate performance can be drastically increased to 450 F g^{-1} at 100 V s^{-1} by utilizing electrodes with a thickness below 100 nm.[247] However, such electrodes are impractical in the context of real-world devices due

to a lack of areal mass loading, usually below 1 mg cm^{-2}.[10] Ideally, we would be able to approach these high values of gravimetric performance, but with electrodes of practical dimensions. With respect to this, hierarchically structured, macroscopic $Ti_3C_2T_x$ electrodes have been shown to hold great promise, increasing areal mass loading with high gravimetric capacitance and high rate-performance.[247,269] A wide range of techniques have been employed to fabricate such electrodes: pillaring with cations[270] or surfactants;[271] spacing with nanomaterials [272] or sacrificial polymers;[247,273] and creating aerogels via freeze drying,[274] often with the aid of cross-linkers.[275–277] These electrode structures, with pores at various length scales from meso- to micro- to nano porous, typically reduce diffusion-related mass transport limitations and lead to faster charge transfer [278] and greater availability of electrochemically active sites.[279] However, most of these techniques require the use of additives or outright functionalization of the MXene which may negatively impact the surface chemistry and conductivity of the electrode. Most importantly, extremely porous electrodes such as aerogels have active material densities as low as 12 mg cm^{-3} [280] and the resulting volumetric capacitance is too low to be practical.[281,282] Recently, it has been demonstrated that electrodes produced by unidirectional freeze casting can be further processed by pressing or calendaring to tailor their microstructure, increasing their density, and decreasing porosity. In this way, volumetric capacitance could be increased by a factor of ~100 compared to the as-synthesized aerogel.[274] However, the resulting microstructure is characterized by low ionic conductivity resulting from unaligned diffusion pathways and poor electrical conductivity, making it unsuitable for use in high-power applications. It is clear, that to produce practical electrodes, high areal mass loading and areal capacitance must be achieved, while preserving rate performance as much as

possible. As this can only be achieved when the electrode structures ensure efficient electrical conductivity as well as ion transport, it is therefore necessary to develop new fabrication processes through which the nano- and microstructure of the electrodes may be precisely tuned.

This chapter details a versatile template-based fabrication process for the synthesis of macroscopic, hierarchical electrodes from $Ti_3C_2T_x$ that can be tuned in both micro- and nanostructure in a controlled manner. The template-based process enables the formation of large (up to several cm^3), interconnected, 3D framework structures which are composed of $Ti_3C_2T_x$ thin films in the form of hollow microtubes (Figure 5.1c and d). The effective thickness of the thin films can be adjusted between ~70 nm and ~220 nm. In this way, the nanostructure of the electrode can be precisely tuned to enable high-rate performance. Furthermore, by non-destructively compressing the as-produced framework structures, their microstructure can be tuned to optimize their volumetric capacitance. Through this process, macroscopic supercapacitor electrodes are realised with areal loadings of up to 7.2 mg cm^{-2} and densities of up to 1440 mg cm^{-3}. These electrodes display gravimetric and volumetric capacitances at 200 mV s^{-1} of 210 F g^{-1} and 140 F cm^{-3} respectively. In optimally configured electrodes, capacitance of ~ 1.4 F cm^{-2} (at 200 mV s^{-1}) can be achieved, ~2 times greater than similarly thick and dense MXene electrode systems.[247,274,283,284]

5.2 Fabrication of Freestanding MXene Microtube Thin Film Structures

The fabrication process of the MXene microtube thin film structures is schematically shown in Figure 5.1a. In short, a highly porous (~94 %) ceramic template consisting of interconnected tetrapodal-shaped ZnO (t-ZnO) microparticles (Figure S 1) is infiltrated with a water-based dispersion of MXenes. Upon drying, the MXene sheets uniformly coat the surface of the template. Afterwards, the t-ZnO template is selectively removed and critical point drying (CPD) is used to obtain a freestanding 3D network[285–287] of hollow MXene microtubes (see Figure S 2), referred to below as aero-MXene (AMX). Thereby, the shape of the pre-defined tetrapodal microstructure is fully maintained (Figure 5.1a and b and Figure S 1b). The details of the infiltration process have been reported elsewhere.[285,286,288] For this work, AMX with a cylindrical geometry (12 mm in diameter and 2 mm in height) has been employed. However, the size and shape of the AMX can be precisely adjusted by utilizing other template geometries, as shown in Figure S 1. The AMX structures consist of a network of interconnected hollow microtubes with a mean length of ~25 µm, a diameter of ~2 µm, as shown in Figure 5.1c and d and Figure S 2. While both diameter and length of the tubes are fixed, the wall thickness of the MXene microtubes can be adjusted between ~70 nm and ~220 nm by varying the number of successive MXene depositions, as illustrated in Figure 5.1c. Freestanding AMX could only be obtained when using more than 3 successive depositions.

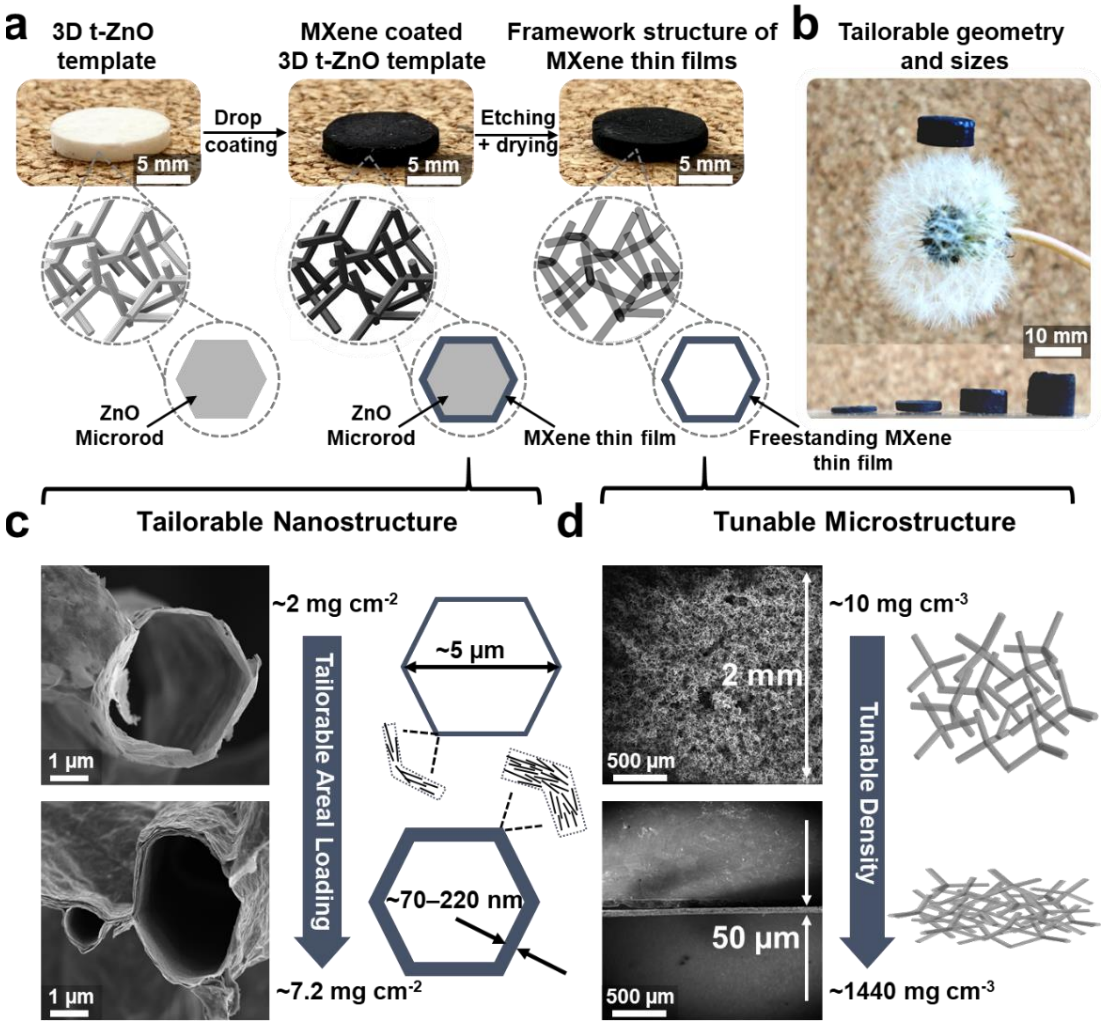

Figure 5.1: Synthesis procedure of freestanding hollow thin film MXene microtubes referred to aero MXene (AMX). (a) Preparation of the freestanding MXene hollow microtube thin films with photographs of the 3D t-ZnO template before and after drop coating with a MXene dispersion, as well as after removal of the template with schematics revealing the microstructure in each step. (b) Photographs of the highly porous (99.9%) AMX structures synthesized in various shapes by template variations. (c) Demonstration of the concept of a tailored nanostructure in which the wall thickness of the hollow microtubes, and thus the area loading of the AMX, can be adjusted by tuning the parameters of the infiltration process, with SEM images of AMX-4D (top) and AMX-20D (bottom) microtubes. (d) Demonstration of the concept of a tuneable microstructure where the density of the AMX can easily be tuned by orders of magnitude with SEM images showing the cross-sections of an as-prepared AMX and an AMX compressed by a factor of 40.

Therefore, AMX-4D-2000 (with D indicating the number of repeated MXene depositions, 2000 indicating the overall thickness in µm), correspond to the lowest possible wall thickness of ~70 nm, while AMX-20D-2000 corresponds to the highest studied wall thickness of ~220 nm (details of the structure see Figure S 3). Through successive MXene depositions, the areal loading of the AMX can be adjusted between ~2 and ~7.2 mg cm^{-2}. Furthermore, the microstructure of the as prepared AMX can be tuned through controlled compression of the AMX, as shown in Figure 5.1d, increasing density with respect to the as-prepared structure of up to 40 times, e.g., by compressing a 2 mm thick AMX structure (AMX-4D-2000) non-destructively to a thickness of 50 µm (AMX-4D-50) (cf. Figure S 4).[289] This controlled compression enables a range of volumetric densities from ~10 to ~1440 mg cm^{-3}.

5.2.1 AMX electrode design for Tuneable Nano and Microstructure

The nanostructure of the AMX material was characterized using advanced TEM techniques. The sum spectra of EDX (Figure 5.2a) indicates complete removal of the sacrificial ZnO scaffold, as does the disappearance of ZnO reflections from XRD in the etched AMX sample (see Figure S 5). The (002) reflection of the etched AMX at 6.03° corresponds to a d-spacing of 14.7 Å, or interlayer spacing of 5.3 Å, based on a dry multilayer spacing of 9.4 Å.[39,230] Raman characterization of the AMX electrodes (Figure S 6) clearly show the in-plane vibration peaks attributable to T_x surface groups at approximately 400 cm^{-1} (predominantly OH), 250 cm^{-1}, and 600 cm^{-1} (predominantly O). Out-of-plane vibrations at approximately 200 cm^{-1} and 720 cm^{-1} often measured in

$Ti_3C_2T_x$ spectra are suppressed due to intercalated water weakening of coupling between the flakes and additionally due to excitation wavelength in the case of the latter.[290]

As described before, the nanostructure, i.e., the wall thickness of the hollow microtubes of the AMX can be tuned by adjusting the parameters of the deposition process. The MXene layer thickness as a function of areal loading is shown in Figure 5.2b. The layer thickness was determined by using STEM-EELS techniques assuming an inelastic electron mean free path of 105 nm (details can be found in the experimental section and in Figure S 7). As shown in Figure 5.2c, there is an almost linear dependence of the MXene microtubes' wall thickness [285,286] from ~11 nm for the AMX-4D-2000 to ~32 nm for the AMX-20D-2000, each deposition step corresponding to an increase in areal loading of ~ 0.3 mg cm^{-2}. The material layer thickness determined via STEM-EELS is the integrated height of solid matter in electron beam direction. Thus, gaps or pores are not considered. The self-organized restacking process of the MXene flakes during deposition process, however, leads to some porosity within the formed hollow MXene microtubes. Furthermore, the calculated inelastic electron mean free path assumes a densely packed material while MXenes themselves have a layered structure with comparatively large lattice parameters in c-direction. Consequently, TEM bright field images (Figure 5.2d and Figure S 8) and SEM images (Figure 5.2 e-i) show a higher (effective) wall thickness of the hollow MXene microtubes compared to the thicknesses from EELS analysis. The coarse layer, or effective, microtube wall thickness thus determined (Figure S 8 and Figure S 9) is in the order of ~70 – 220 nm for the AMX-4D-2000 and AMX-20D-2000 respectively. In addition to the neglection of porosity, the wall thicknesses determined by the EELS log ratio method must be considered as a

lower boundary as the calculated electron mean free paths are often smaller than experimental data in the case of high energy electrons in TEM.[291]

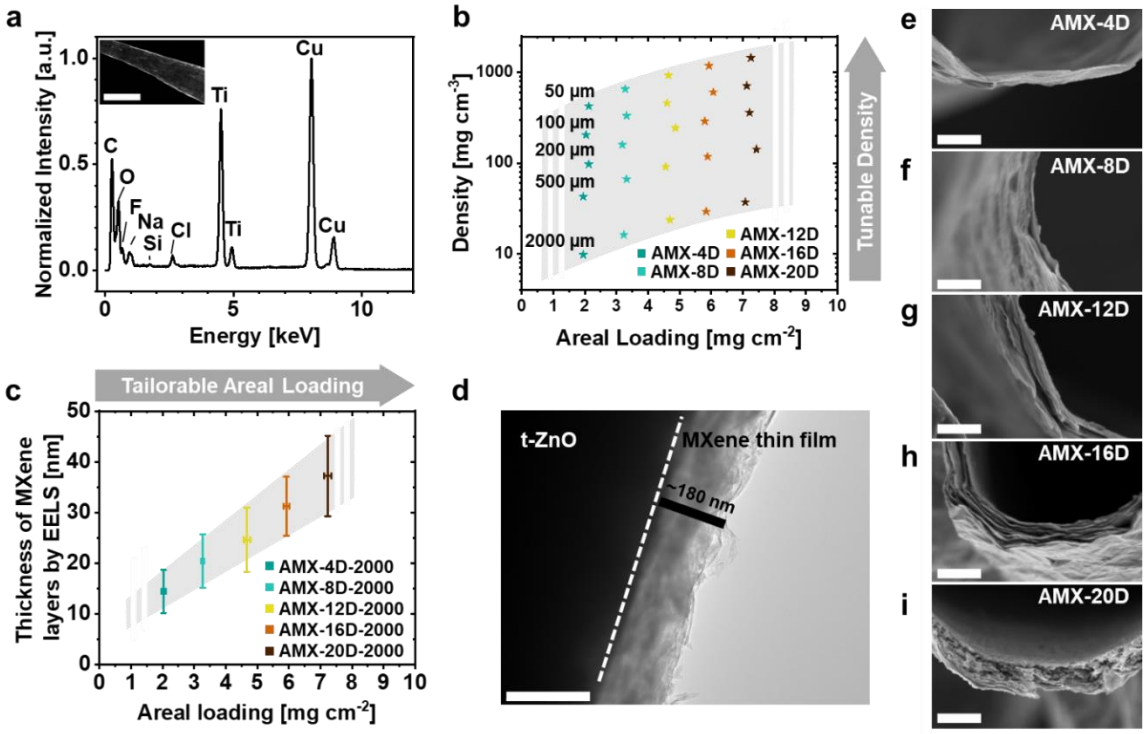

Figure 5.2: (a) EDX spectrum recorded by scanning across an AMX microtube after template removal (see inset, scale bar 4 µm) showing that no (ZnO) is present. (b) Density and area loading of various prepared AMX structures showing the versatility of the approach used, with the grey area denoting the region of possible electrodes and the stars denoting the prepared samples. (c) Layer thickness of the differently prepared AMX structures with tailored nanostructure determined by STEM EELS line scans across individual AMX tubes. (d) Bright field image of an AMX-16D before t-ZnO etching showing the effective film thickness on the t-ZnO surface (scale bar 200 nm), including pores or gaps between MXene flakes. (e-i) SEM images of AMX-4D-2000, AMX-8D-2000, AMX-12D-2000, AMX-16D-2000, AMX-20D-2000, each looking at a free-standing MXene microtube, showing the increase in wall thickness due to the deposition process used (scale bar: 400 nm).

As previously mentioned, the microstructure and thus, the density of the AMX can be tuned by compression. By controlling both the compression and depositions, the density of the AMX can be tuned by orders of magnitude from ~10 mg cm^{-3} – ~1440 mg cm^{-3} while at the same time the areal loading is adjustable from ~2 mg cm^{-2} - ~7.2 mg cm^{-2} (Figure 5.2b and c). In summary, the fabrication process presented here enables highly customizable multi-scale 3D electrode structures comprised of 2D nanomaterials.

5.2.2 Tuneable Nanostructure for High-Rate Areal Capacitance

The electrochemical performance of the AMX supercapacitor electrodes was evaluated in a three-electrode configuration using 0.5 M H_2SO_4 aqueous electrolyte (setup see Figure S 10a, b). AMX electrodes with tailored nanostructure ($4 < D < 20$), each compressed 10 times to ~200 µm height (initial height = 2000 µm), were investigated. Figure 5.3a shows the CVs from 5 mV s^{-1} to 1000 mV s^{-1} of an AMX-16D-200 (others see Figure S 11a, c, e, g and i) indicating typical shape for $Ti_3C_2T_x$, combining the rectangular shape at potential extremes of EDLC with peaks indicative of pseudocapacitance.[228,247,292] The peaks at around –0.45 V (vs. Ag/AgCl) for 5 mV s^{-1} are assigned to pseudocapacitive reactive groups of the MXene.[292] With increasing scan rate, the oxidation and reduction peaks shift to higher and lower potentials, respectively. However, at 500 mV s^{-1} a clear peak in the oxidation scan is still observable, indicating fast diffusion, which indicates good rate performance. Furthermore, at low scan rates there is a narrow peak-to-peak spacing (< 20 mV at 5 mV s^{-1}) and clear oxidation and reduction peaks. Figure 5.3b, c demonstrates the cyclic voltammetry (CV) curves of AMX with different microtube wall thicknesses (AMX-4D-200 to AMX-20D-200), at

scan rates of 10 mV s^{-1} and 200 mV s^{-1}. [17,37,38] As expected from the increase in mass with increasing microtube wall thickness, peak current approximately doubles from AMX-4D-200 to AMX-8D-200 and again to AMX-20D-200 (Figure 5.3a). Oxidation and reduction peaks are clear, and peak-to-peak separation is on the order of 20 mV in all cases, indicating a highly reversible redox process with small IR drop.[293,294] At 200 mV s^{-1} (Figure 5.3c), the aforementioned peak positions are shifted to higher and lower potentials respectively, but are still clearly visible. However, the scaling of the peak current at 200 mV s^{-1} is less linear as the microtube wall thickness increases.

Similar behaviour can be observed in galvanostatic charge and discharge studies, as shown in Figure S 11b, d, f, h, and j. When comparing samples with increasing microtube wall thickness, they show almost identical charge and discharge characteristics, especially at lower current densities in between 2-20 A g^{-1}, indicating good capacitance retention and material activation even at high MXene mass loadings. For example, the sum of charge and discharge time at 20 A g^{-1} is 22.46 s, 23.55 s, 19.87 s, 21.10 s and 19.34 for AMX-4D-200, AMX-8D-200, AMX-12D-200, AMX-16D-200, and AMX-20D-200 respectively, showing only small deviations between the samples. Best performance, at 23.55 s, is achieved by the AMX-8D-200 electrode.

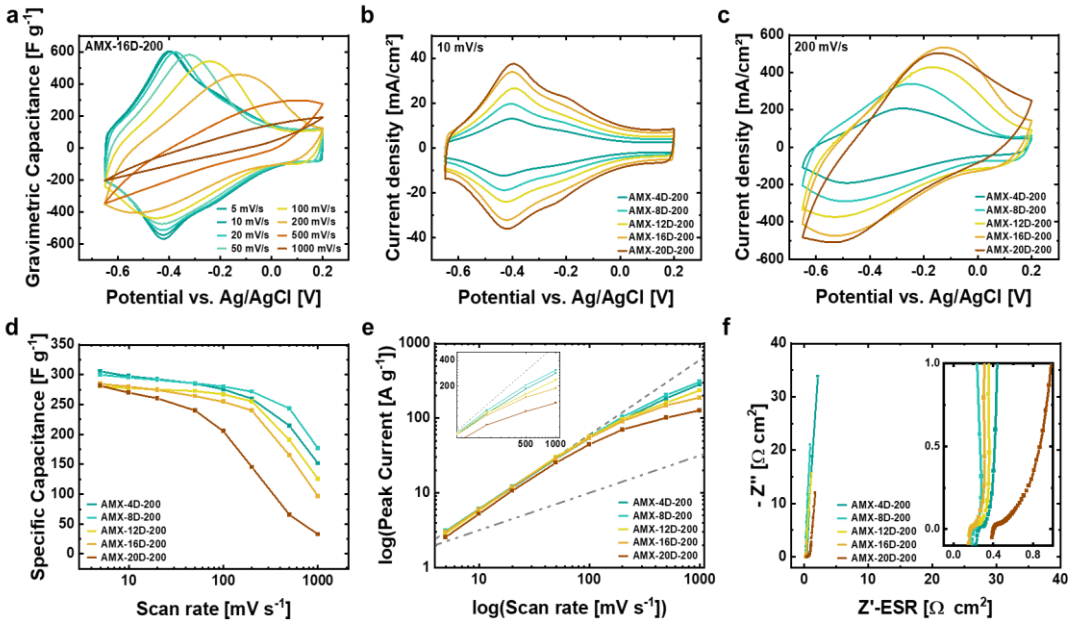

Figure 5.3: Electrochemical performance of $Ti_3C_2T_x$ electrodes with tuned nanostructure. (a) Cyclic voltammograms of an AMX-16D-200 with a mass loading of 5.8 mg cm^{-2} in 0.5 M H_2SO_4 at scan rates from 5 mV s^{-1} to 1000 mV s^{-1}. (b) Cyclic voltammograms of different AMX structures with a thickness of 200 µm and weight loading of 2.1 mg cm^{-2}, 3.2 mg cm^{-2}, 4.4 mg cm^{-2}, 5.8 mg cm^{-2} and 7.2 mg cm^{-2} collected at 10 mV s^{-1} and (c) at 200 mV s^{-1}. d) Rate performance of AMX structures with different microtube wall thickness in terms of gravimetric capacitance. (e) Logarithmic representation of the peak current with respect of the scan rate for the determination of the slope, b, for the AMX structures with different microtube wall thickness. Inset is the region of interest above 200 mVs^{-1} where the samples most strongly diverge. (f) Electrochemical impedance spectroscopy collected at 0.2 V vs Ag/AgCl for different AMX structures with an inset showing a zoom in the high frequency area.

Figure 5.3d shows the gravimetric capacitance of AMX electrodes as a function of scan rate. For all scan rates, the specific gravimetric capacitance is reduced with increasing microtube wall thickness, e.g., at 100 mV s^{-1} the gravimetric capacitance of AMX-4D-200 is around 280 F g^{-1}, while an AMX-16D-200 electrode is around 250 F g^{-1}. As shown in Figure 5.3d, up to 200 mV s^{-1}, the specific gravimetric capacitance only

decreases slightly for all electrode configurations. At higher scan rates (>200 mV s^{-1}) the gravimetric capacitance decreases strongly with increasing microtube wall thickness, resulting in progressively poorer capacitance retention. AMX-8D-200 stands out with 50 % capacitance retention at 1000 mV s^{-1}, whereas AMX-16D-200 retains only 35 % capacitance at the same scan rate. This difference is also visible in Figure S 11, showing the CVs for all other AMX, where AMX-8D-200 has consistently smaller peak-to-peak separation than the other samples, and retains a visible oxidation peak even at 1000 mV s^{-1}.

It is expected that at higher scan rates, thicker microtube walls will restrict ion transport in the electrode, however, as mentioned previously, increased wall thickness is also expected to reduce the internal resistance of the electrode, manifesting in greater overall current and a smaller shift in redox peak potentials. These two properties are optimized for the AMX-8D-200 sample, neither too thick for significant diffusion limitation, nor too thin for poor conductivity.

In CV measurements, the peak current, i_p is comprised of current associated with double layer capacitance and fast faradaic reactions on the surface, i_{cap}, and slow, diffusion-limited processes i_{diff}.[295] To analyse the effect of increased microtube wall thickness on the charge storage kinetics more robustly in each electrode, a power law dependence of peak current on scan rate may be assumed:[296]

$$\boldsymbol{i_p = i_{cap} + i_{diff} = a\nu^b} \quad (53)$$

where ν is the scan rate, and a and b are variables. The linear dependence of i_{cap} on ν means that $b = 1$ for systems in which i_p is entirely dependent on capacitive processes,

whereas for entirely diffusion-limited systems $b = 0.5$ due to the square root dependence of i_{diff} on ν.[297] In Figure 5.3e it can be seen that in all samples, $b \approx 1$ up to 100 mV s^{-1}, though a divergence after this point is observed in the thicker samples, trending towards $b = 0.5$ at a higher rate. This more diffusion limited behavior indicates that the increased conductivity associated with very thick microtube wall thickness cannot compensate for the longer ion diffusion paths of the same at high scan rates. The inset in Figure 5.3e indicates a slight decrease in the slope of AMX-8D-200 with respect to AMX-4D-200 above 500 mV s^{-1}, revealing that the AMX-8D-200 sample is indeed more diffusion limited, however this is compensated for by its larger peak current density, supporting the conclusions from Figure 5.3d. Furthermore, as seen in the inset electrochemical impedance spectroscopy (EIS) plot in Figure 5.3f, the series resistance decreases almost linearly with the number of depositions. This reinforces the previous conclusion of optimized electrical and ionic properties for AMX-8D-200. The long-term performance of the AMX-16D-200 sample at a constant current density of 20 A g^{-1} shows a specific capacitance of 261 F g^{-1} at the beginning and 256 F g^{-1} thereafter with almost no loss, supported by a high coulombic efficiency consistently above 99.6 % (see Figure S 11). Moreover, Raman studies after 0, 50, 100, 300 and 5000 cycles (see Figure S 6c) indicate negligible difference in the shape and height of the peaks, which also indicates no change in the structural and chemical properties of $Ti_3C_2T_x$. Overall, the electrochemical studies clearly demonstrate that increasing the wall thickness of the microtubes and thereby tuning the electrode's nanostructure significantly increases the capacitance per unit area of the electrodes with little loss in gravimetric capacitance and response time, with optimal rate performance observed for AMX-8D-200.

5.2.3 Tuneable Microstructure by Compression for High-Rate Volumetric Capacitance

While tuning the microtube wall thickness enables us to optimize the areal loading of the AMX electrodes, the high overall porosity of the initial framework structure (~99.8 %) results in a poor volumetric capacitance, e.g., AMX-8D-2000 ~5 F cm^{-3}. As previously discussed, (Figure 5.1d) the AMX electrodes can be compressed up to 40 times without appreciable loss in structural integrity. To study the effect of the compression on the microstructure and electrochemical performance AMX-8D-2000 electrodes were compressed in thickness to 500 µm (AMX-8D-500), 200 µm (AMX-8D-200), 100 µm (AMX-8D-100) and 50 µm (AMX-8D-50). As demonstrated in Figure 5.4a, at low scan rates of 5 mV s^{-1}, the electrochemical performance is not affected at all, indicating a retention of the mechanical and electrical integrity of the electrodes, even at a compression factor of ~40. Furthermore, the absence of changes to redox peak amplitude or overall capacitance implies that for low scan rates, diffusion is sufficiently fast, and that significant restacking or other destruction of ionic pathways has not occurred. At higher scan rates of 200 mV s^{-1}, a clear difference in the electrochemical behaviour can be seen as the peak current decreases with increasing compression (Figure 5.4b). These indicate that the best rate performance is obtained from AMX-8D-100, with a clearer oxidation peak at a lower potential and greater capacitance overall (Figure 5.4c). Indeed, in the case of AMX-8D-50, the oxidation peak is barely visible, and capacitance is on the order of half of that compared to other samples. This points to a disimprovement in diffusional properties, most probably because of the loss in porosity. The overall trend in gravimetric capacitance is shown in

Figure 5.4d, with AMX-8D-200 exhibiting greater capacitance up to 200 mV/s. The advantage shifts to AMX-8D-100 at 500 mV s^{-1} and above, which retains 93 % of its maximum capacitance at 500 mV s^{-1} compared to 80 % for AMX-8D-200 and 58 % for AMX-8D-50. All AMX-8D samples show purely capacitive-like behaviour up to 50 mV s^{-1}, with a value of $b \approx 1$ (Figure 5.4e), though a clear divergence after this point is observed in the 50 µm sample, trending towards $b = 0.5$ at a much greater rate. This more diffusion limited behaviour indicates that ion transport is being hindered

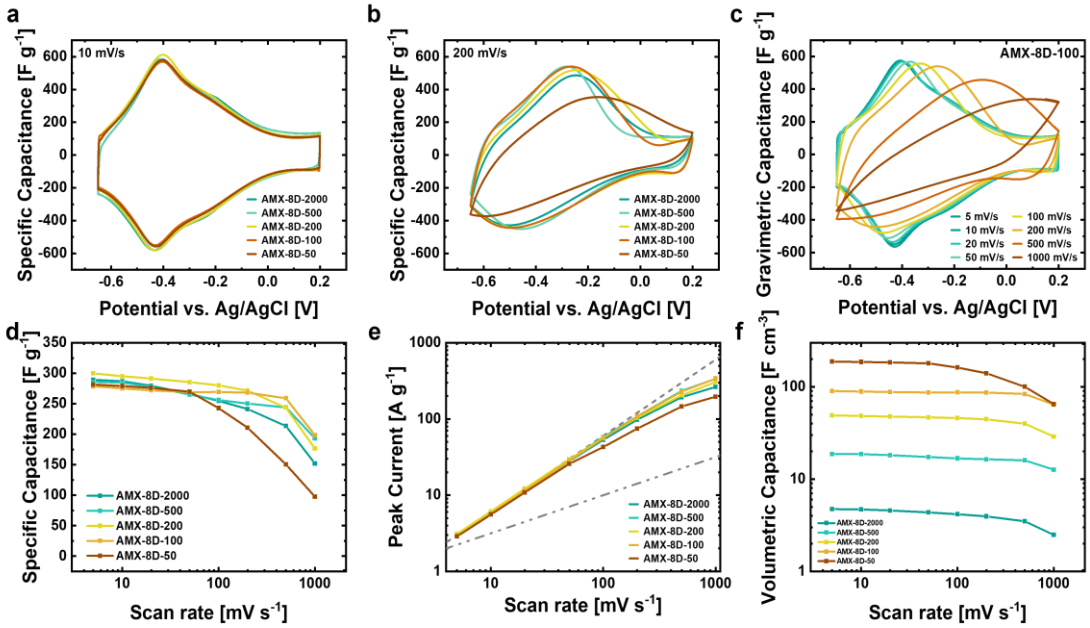

Figure 5.4: Electrochemical performance of $Ti_3C_2T_x$ electrodes with tuned microstructure. (a) Cyclic voltammograms of AMX-8D-2000 structures compressed to 500, 200, 100 and 50 µm collected at 10 mV s^{-1}. (a) Cyclic voltammograms of AMX-8D-2000 structures compressed to 500, 200, 100 and 50 µm collected at 200 mV s^{-1}. (c) Cyclic voltammograms of an AMX-8D-100 with a density 323 mg cm^{-3} collected at scan rates from 5 mV s^{-1} to 1000 mV s^{-1}. d) Rate performance of AMX structures with different density in terms of gravimetric capacitance. (e) Logarithmic representation of the peak current with respect of the scan rate for the determination of the slope, b, for the AMX structures with different density. (f) Rate performance of AMX structures with different density in terms of volumetric capacitance.

by the reduction in porosity more than can be compensated for by the reduction in overall thickness of the electrode at such an extreme degree of compression. On the other hand, the slope above 500 mV s^{-1} is marginally closer to 1 for the AMX-8D-100 sample, indicating that diffusion may be slightly aided by the reduced thickness of the electrode, and that the porosity is sufficient for uninhibited ion transport. While gravimetric capacitance is a useful metric to assess how well the active material in an electrode is utilized, real-world devices are more often limited by volume, and this is where tuning the microstructure of AMX electrodes by compression becomes important. Figure 5.4f gives an overview of the volumetric capacitance of the AMX electrodes, which at scan rates up to 50 mV s^{-1} scales linearly with the degree of compression. Indeed, even at 50 mV s^{-1}, volumetric capacitance of 180 F cm^{-3} is achieved in the AMX-8D-50 sample. Though diffusional limitations cause a steeper falloff in capacitance at high scan rates with respect to the AMX-8D-100, it only reaches parity at a scan rate of 1000 mV s^{-1}. This represents a discharge time of < 1 s, and would make such an electrode suitable for the plurality of energy storage applications SCs are typically employed in.[64,65]

5.2.4 Optimization of Gravimetric and Volumetric Electrode Performance

By addressing both, the nano- and microstructure of the AMX electrodes, their electrochemical performance can be optimized for mass and/or volume depending on the rate performance requirements of the intended application. The relationship between volumetric and gravimetric capacitance at scan rates from 5 to 1000 mV s^{-1} is summarized in Figure 5.5a and b for the tuneable nano- and microstructured AMX

electrodes, respectively. Notably, neither increased compression of the electrode nor increased layer thickness lead to a profound decrease in performance, especially at low scan rates, enabling electrodes with high volumetric and areal capacitance.

Additionally, it is important to note that for commercial SCs, areal capacitance, density and gravimetric capacitance must be considered concurrently. A high areal capacitance improves the packaging of a device by proportionally reducing the amount of supporting material (current collectors, separators) required for the desired overall capacitance. However, the density is one of the most important characteristics of the electrode because it affects both volumetric as well as gravimetric capacitance simultaneously. In terms of the feasibility of 2D nanomaterial-based SCs, gravimetric performance is vital, as commercially available carbon-based SCs have low costs associated with the active material. SC-grade activated carbon has a market value in the region of 15 – 50 USD kg^{-1},[298] and it is therefore critical that efficient use is made of the mass of 2D nanomaterials incorporated in a device. At the high scan rates shown (200 mV s^{-1}), reflecting a discharge time on the order of ~5 s (typical for supercapacitor applications),[64,65] the AMX electrode materials show broadly superior performance than other state-of-the-art supercapacitor electrode systems (Figure 5.5c and d).

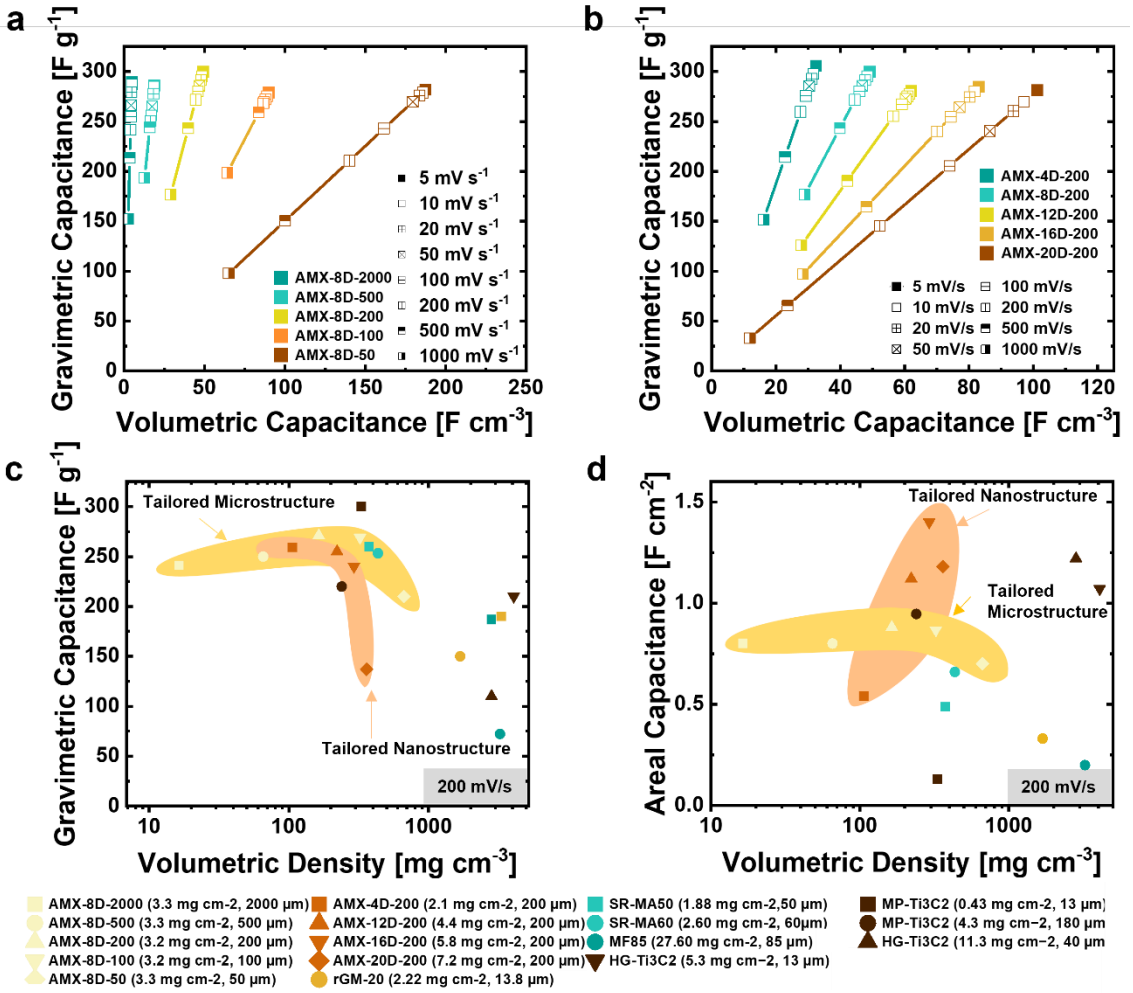

Figure 5.5: (a) Relation between gravimetric and volumetric capacitance for freestanding AMX structures with tailored microstructure and hence, density, at scan rates from 5 mV s^{-1} to 1000 mV s^{-1}. (b) Relation between gravimetric and volumetric capacitance for freestanding AMX structures with tailored nanostructure and hence, areal loading, at scan rates from 5 mV s^{-1} to 1000 mV s^{-1}. (c) Relationship between gravimetric capacitance and volumetric density of fabricated freestanding AMX structures with tailored nano- and microstructure compared to other electrode structures with comparable density and electrode thickness from current literature. (d) Relationship between areal capacitance and volumetric density of fabricated freestanding AMX structures with tailored nano- and microstructure compared to other electrode structures from current literature.[247,274,283,284]

Notable outliers are MP-Ti3C2 (0.43 mg cm^{-2}, 13 µm)[247] and HG-Ti3C2 (11.3 mg cm^{-2}, 40 µm),[247] which exceed AMX electrodes in gravimetric capacitance and volumetric density, respectively. These electrodes are analogous to AMX in their controlled microstructure in the case of MP-Ti3C2 (0.43 mg cm^{-2}, 13 µm) and nanostructure in the case of HG-Ti3C2 (11.3 mg cm^{-2}, 40 µm). However, taking Figures 5.5c and d in aggregate, MP-Ti3C2 (0.43 mg cm^{-2}, 13 µm) shows order of magnitude smaller areal capacitance than AMX, in return for a relatively modest improvement in gravimetric capacitance. Similarly, the volumetric density of HG-Ti3C2 (11.3 mg cm^{-2}, 40 µm) comes at the cost of gravimetric capacitance to the extent that the areal capacitance is comparable to that of AMX. This outstanding performance can be attributed to the well-controlled micro- and nanostructure of AMX electrodes.

5.2.5 Device Performance

To evaluate the practical performance of the AMX-based electrodes, an asymmetric supercapacitor of AMX-4D-200 against oversized activated carbon cloth in 0.5 M H_2SO_4 in a CR2032 coin cell was tested as a proof of principle device. Figure 5.6a shows CV curves at different scan rates ranging from 5-100 mV s^{-1}. Especially at low scan rates, the typical rectangular pattern of EDLC as well as peaks attributable to pseudocapacitance are present. As the scan rate increases, the peaks shift to higher potentials for the oxidation and vice versa for the reduction processes.

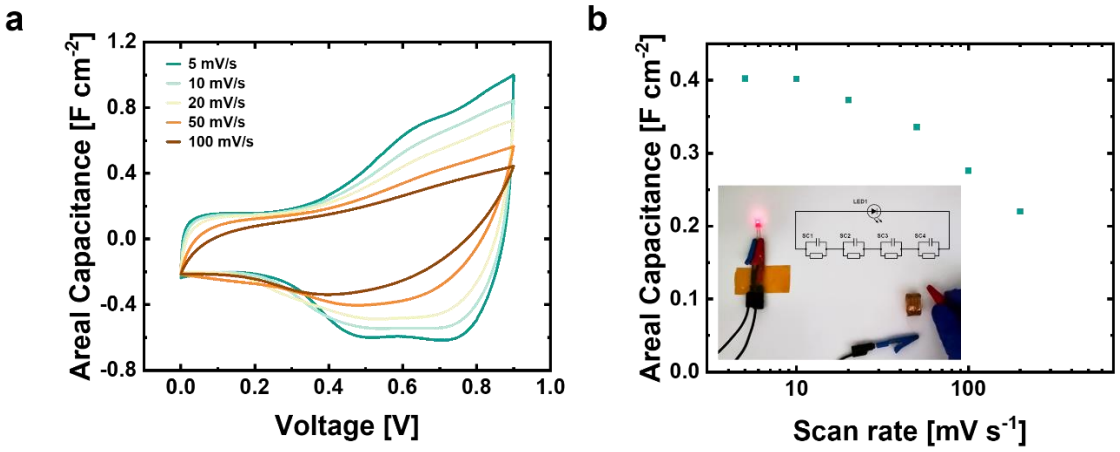

Figure 5.6: (a) Cyclic voltammograms of a two-electrode asymmetrical device consisting of an AMX-4D-200 working electrode and a carbon cloth counter at scan rates ranging from 5 to 100 mV s^{-1}. (b) Areal capacitance calculated for the AMX-4D-200 electrode for various scan rates with inset showing a photograph of a red LED illuminated by four AMX-4D-200/carbon cloth supercapacitors in series.

Areal capacitance normalized to the common area of the electrodes vs. scan rate is shown in Figure 5.6b, decreasing from 0.402 F cm^{-2} at 5 mV s^{-1} to 0.220 F cm^{-2} at 200 mV s^{-1} (see Figure 5.6b). Inset is an image of four CR2032 AMX-based asymmetric devices in series, powering a red LED, showing the possibility of practical implementation of such devices as a stand-alone power supply. Figure S 13b shows long-term cycling at 9 mA cm^{-2} for 10000 cycles with good cycling stability of ~0.309 F cm^{-2} before testing and ~0.264 F cm^{-2} after testing as well as a constant coulombic efficiency of about 96%.

5.3 Conclusions

In summary, this Chapter has demonstrated how the micro- and nanostructure of 3D networked MXene thin films affect electrochemical performance and demonstrated a versatile and simple approach to improve both structural aspects using the same experimental approach. Well-aligned MXene layers are formed on a sacrificial scaffold by wet chemical assembly, resulting in a highly organized electrode structure with highly conductive electronic and ionic pathways. The 3D networked MXene thin films may be tuned in thickness from tens to hundreds of nanometres, leading to good accessibility of the individual MXene flakes and resulting in high gravimetric capacitance of 240 F g^{-1}, even at 200 mV s^{-1}. Second, controlled densification by up to 40 times compared to the initial state did not compromise the mechanical integrity of the electrodes and resulted in a high volumetric capacitance of up to 180 F cm^{-3} at 50 mV s^{-1}. Furthermore, excellent areal capacitance of more than 1.4 F cm^{-2} at high scan rates of 200 mV s^{-1} was achieved. These unique properties mean that 3D networked MXene thin film electrodes compare favourably to other state-of-the-art supercapacitor electrodes when adopting a wholistic view of tunability as well as gravimetric, volumetric, and areal capacitance. This study clearly demonstrates the importance of thorough control over the nanometre- and micrometre-scale features of electrodes and opens new possibilities for application-grade supercapacitors.

5.4 Experimental Methods

5.4.1 MXene Synthesis

$Ti_3C_2T_x$ MXene was synthesised according to the variation of MILD synthesis detailed in Section 3.5.1.

5.4.2 Preparation of $Ti_3C_2T_x$ Aeromaterial

For the preparation of freestanding $Ti_3C_2T_x$ electrodes, tetrapodal ZnO (t-ZnO) particles, produced by a simple flame transport synthesis [299], were used as a sacrificial template material. The obtained t-ZnO powder is pressed into cylinders (diameter = 12 mm, height = 2 mm) with a density of 0.3 g cm^{-3}. The cylinders were heat treated at 1150 °C for 5 h to obtain a freestanding and interconnected network. The prior obtained concentrated MXene ink was diluted to ~2 mg/ml using deionized water and probe sonicated at 30% amplitude for 2 mins (Sonoplus, Bandelin) to achieve a well-mixed dispersion. Afterwards, the t-ZnO networks were saturated with the MXene dispersion and dried at 40 °C for 4 hours to allow evaporation of the water. By repeated saturation and drying steps, the weight loading with MXene is adjusted. The final template was then treated in diluted HCl (Carl Roth) overnight to fully etch the ZnO and rinsed with deionized water and absolute ethanol (99.99 %, Carl Roth) and finally dried using a critical point dryer (Leica EM CPD300). Compression of the tuneable microstructure samples was achieved using a steel die with a spacer corresponding to the final thickness which was compressed gently by hand.

5.4.3 Preparation of $Ti_3C_2T_x$ Aeromaterial Electrodes

The freestanding $Ti_3C_2T_x$ aeromaterial structures were affixed to glass slides using 100 µl silver conductive paint (RS Pro) spread into an approximately 11 mm circle into which a doubled length of 0.1 mm silver wire was inserted (cf. Figure S 5b). The electrode was placed onto the paint and pressed gently to ensure adhesion but avoid deformation. The exposed silver wire was covered with Kapton tape (RS components) leaving sufficient length free at the end to connect a crocodile clip. The paste was dried in ambient conditions for 1 hour before being placed in a vacuum desiccator for a minimum of 2 hours to fully dry the silver paint.

5.4.4 Preparation of $Ti_3C_2T_x$/Activated Carbon Cloth Asymmetric Devices

Steel 2032-type coin cell housings, spacers, and springs (MTI) were used to prepare the asymmetric devices. Freestanding $Ti_3C_2T_x$ aeromaterial structures were used as the negative electrode and oversized activated carbon cloth (Kynol GmbH) cut into 12 mm discs used as the positive electrode. Both electrodes were pre-soaked with 0.5 M H_2SO_4 and were assembled with PES filter membrane (Whatman) cut into 14 mm discs as separator.

5.4.5 Electrochemical Measurements

All electrochemical measurements were carried out with a VMP-300 potentiostat (BioLogic S.A.). The electrochemical cell, as seen in Figure S 5a was configured with

the as-prepared Ti_3C_2 electrode as the working electrode, an oversized glassy carbon rod as the counter electrode, and an Ag/AgCl reference (SI Analytics). The electrolyte used was 0.5 M H_2SO_4. A potential window of -0.65 to 0.2 V was chosen for the measurements, which consisted briefly of cyclic voltammetry (CV) from 5 mV s^{-1} to 1000 mV s^{-1}; galvanostatic cycling with potential limitation (GCPL) with current density from 2 to 100 A g^{-1}; potentiostatic electrochemical impedance spectroscopy (PEIS) from 10 mHz to 100 kHz, and long term GCPL for 5000 cycles at a current density of 10 A g^{-1}. Samples were pre-cycled before the above set of measurements using CV at 50 mV s^{-1} for 300 cycles. This was to allow full wetting of the electrodes, especially in the case of the highly compressed samples.

Electrochemical characterization of the $Ti_3C_2T_x$/activated carbon cloth asymmetric devices was performed using a VMP-300 potentiostat (BioLogic S.A.). A potential window of 0 to 0.9 V was used for the measurements, which consisted of CVs from 5 to 100 mV s^{-1} and GCPL with a current density of 9 mA cm^{-2} for 10000 cycles for long term stability testing. Areal capacitance was calculated using the common area of the two electrodes. To power an LED, four asymmetric devices were assembled in series and charged to 3.6 V at 5 mA, before connecting to the circuit.

5.4.6 Capacitance Calculations

Specific capacitance for each electrode was calculated using the discharge portion of the fourth CV curve according to the following equation:

$$C/m = \frac{1}{m_e \upsilon \Delta V} \int_{-0.65}^{0.2} idV$$

Where $C\ m^{-1}$ is the specific capacitance (F g^{-1}), i is the current (mA), V is the potential (V), m_e is the electrode mass (g), υ is the scan rate (mV s^{-1}) and ΔV is the potential window (V). See also Section 2.7.1.

The volumetric capacitance was calculated in the same manner according to the following equation:

$$C/V = \frac{1}{V_e \upsilon \Delta V} \int_{-0.65}^{0.2} idV$$

Where CV^{-1} is the specific capacitance (F cm^{-3}), i is the current (mA), V is the potential (V), V_e (cm^{-3}) is the volume of the electrode defined by the area of the template used (cm^{-2}) and the thickness determined by SEM (cm), υ is the scan rate (mV s^{-1}) and ΔV is the potential window (V).

5.4.7 Characterisation of Structure and Properties

The structure and morphology of the aeromaterial was characterised by SEM using a Zeiss Supra 55VP operated at 2 kV.

The nanostructure of both MXene covered ZnO templates as well as free-standing AMX structure was analysed by transmission electron microscopy (TEM) with a FEI Tecnai F30 G^2 at 300 kV acceleration voltage. In order to obtain separated tetrapods a small amount of material was ground in butanol and drop coated onto lacey carbon TEM grids. The chemical composition of single tubes of the AMX material is analysed via

energy dispersive x-ray spectroscopy (EDX, EDAX Si-Li detector) in the TEM. The wall thickness of single AMX tetrapod arms / tubes is determined via the electron energy loss spectroscopy (EELS) log ratio method.[211]

The thickness in electron beam direction can be determined in multiples of the electron mean free path (eMFP) by comparing the integrated intensity of the zero-loss peak to the total integrated intensity (see Figure S 10) in the case of inelastic scattering. A scanning TEM (STEM) EELS line scan over the width of an AMX tube yields an eMFP thickness profile. Taking an average of the centre region, multiplying with a suitable value of the eMFP for the $Ti_3C_2T_x$ MXene material and dividing by a factor of 2 (due to two layers being penetrated by the electron beam) then gives the wall thickness of the aeromaterial. Values for the eMFP can be calculated *via* an estimation given in [211] or [300]. Multiple tubes and positions are measured for each amount of areal loading.

5.5 Acknowledgements

I would like to thank Helge Krüger for the preparation and imaging of the AMX materials in Germany for our electrochemical experiments in both Kiel and Dublin. I would also like to thank Niklas Kohlmann for the TEM and EELS measurements detailed in this chapter.

6 CONCLUSIONS AND OUTLOOK

In this work, the results of two methods, distinct in technique but similar in goal, for the fabrication of hierarchical 3D structured electrodes have been presented. These were based on the MXene, $Ti_3C_2T_x$.

The MXene was synthesised from its precursor MAX phase, Ti_3AlC_2 and shown to be of high quality, suitable for the lofty electrochemical goals of the subsequent works. The material was etched using a derivative of the MILD synthesis protocol, relying on the formation of *in situ* HF to both etch and delaminate the MAX phase. The yield synthesis was improved dramatically by a simple, single step, freeze-thaw assisted delamination, increasing the mass of MXene flakes obtained by 42 ± 6% and resulting in larger flakes from which, more conductive films could be made.

Chapter 4 detailed the first direct 3D printing of microsupercapacitors from binder free aqueous MXene inks. These microsupercapacitors were enabled by the extremely versatile AJP process, which allowed for the creation of miniscule 3D structures with enormous variety in geometry. 3D microsupercapacitors were shown to perform 97% better in areal capacitance than 2D devices of equal mass and three-electrode measurements of high density micropillared electrodes resulted in exceptional values for areal and volumetric capacitance. These results were enabled by the 3D micropillar

arrays from which the electrodes were constructed, allowing for exceptional areal loading without compromising performance. Notably, this was all made possible without the use of any post-processing techniques, binders, or organic solvents.

Moving up in scale, Chapter 5 detailed a versatile and simple approach to tailor the nano- and microstructure of 3D networked MXene thin films. The 3D aeromaterials were formed from MXene deposited on a sacrificial scaffold by wet chemical assembly, resulting in a highly porous and electrically conductive structure. The nanostructure of the 3D networked thin films could be tailored in thickness from tens to hundreds of nanometres, resulting in high gravimetric capacitance and high-rate performance. Additionally, the microstructure could be controlled though densification by a factor of up to 40 times that of the initial aeromaterial. This could be done without severely compromising the integrity of the electrodes and resulted in a high volumetric capacitance and areal capacitance, even at high scan rates. The 3D networked MXene thin film electrodes compared favourably to other state-of-the-art supercapacitor electrodes when adopting a wholistic view of gravimetric, volumetric, and areal capacitance.

The overall outlook for these works is extremely positive. The freeze-thaw assisted delamination can likely be extended to other MXenes from more exotic MAX phases to make the most of these often-expensive precursors. AJP printing of 3D MXene microsupercapacitors has promise in the creation of integrated energy storage in compact electronic devices and has potential to be employed to help exploit the outstanding properties of MXene microsupercapacitors even further. The 3D networked MXene thin film electrodes have performed exceptionally and have formed the basis for

important work going forward. The results from Chapter 5 were used to justify and secure a joint EIC transition project between the Nicolosi Group and our collaborators in Kiel. This is of course important for our respective groups but especially for me because it means I have a job until 2025. We will be scaling up the electrodes and creating exciting pseudocapacitive energy storage devices that are close to market ready by the end of the 3-year project. The 2.5M grant is to cover our supercapacitor development and the development of a novel DC-DC converter with integrated energy storage by the Power Electronics group in Kiel. I'm gladdened to know that the work on which my Thesis is based will at a bare minimum fund further exciting science, and with any luck, will help move MXene supercapacitors further from the fume hood and closer to the market.

7 REFERENCES

1. Toth, N. P., Schick, K. D. & Semaw, S. *The Oldowan: case studies into the earliest stone age*. (Stone Age Institute Press Bloomington, 2006).
2. Schaming, D. & Remita, H. Nanotechnology: from the ancient time to nowadays. *Found Chem* **17**, 187–205 (2015).
3. Arnold, W. *et al.* A Red Opaque Glass From Sardis and Some Thoughts on Red Opaques in General. *The Journal of Glass Studies* **30**, 16–27 (1988).
4. Reibold, M. *et al.* Carbon nanotubes in an ancient Damascus sabre. *Nature* **444**, 286 (2006).
5. Faraday, M. Experimental Relations of Gold (and other Metals) to Light. *Phil. Trans. R. Soc.* **147**, 145–181 (1857).
6. Simon, P. & Gogotsi, Y. Materials for electrochemical capacitors. *Materials for Sustainable Energy: A Collection of Peer-Reviewed Research and Review Articles from Nature Publishing Group* 138–147 (2010) doi:10.1142/9789814317665_0021.
7. Wang, Y. *et al.* Supercapacitor devices based on graphene materials. *Journal of Physical Chemistry C* **113**, 13103–13107 (2009).
8. Kossyrev, P. Carbon black supercapacitors employing thin electrodes. *J Power Sources* **201**, 347–352 (2012).

9. Zhang, X., Zhang, Z. & Zhou, Z. MXene-based materials for electrochemical energy storage. *Journal of Energy Chemistry* **27**, 73–85 (2018).

10. Sun, H. *et al*. Hierarchical 3D electrodes for electrochemical energy storage. *Nat Rev Mater* **4**, 45–60 (2019).

11. Boholm, M. & Arvidsson, R. A Definition Framework for the Terms Nanomaterial and Nanoparticle. *Nanoethics* **10**, 25–40 (2016).

12. Kreyling, W. G., Semmler-Behnke, M. & Chaudhry, Q. A complementary definition of nanomaterial. *Nano Today* **5**, 165–168 (2010).

13. Barsoum, M. W. MN+1AXN phases: a new class of solids; thermodynamically stable nanolaminates. *Progress in Solid State Chemistry* **28**, 201–281 (2000).

14. Jeitschko, W., Nowotny, H. & Benesovsky, F. Kohlenstoffhaltige ternäre Verbindungen (H-Phase). *Monatsh Chem* **94**, 672–676 (1963).

15. Jeitschko, W., Nowotny, H. & Benesovsky, F. Kohlenstoffhaltige ternare Verbindungen. *Mh. Chem.* **94**, 844–850 (1963).

16. Jeitschko, W., Nowotny, H. & Benesovsky, F. Carbides of formula T2MC. *Journal of The Less-Common Metals* **7**, 133–138 (1964).

17. Jeitschko, W. & Nowotny, H. Die Kristallstruktur von Ti3SiC2-ein neuer Komplexcarbid-Typ. *Monatsh Chem* **98**, 329–337 (1967).

18. Barsoum, M. W. & El-Raghy, T. Synthesis and characterization of a remarkable ceramic: Ti3SiC2. *Journal of the American Ceramic Society* **79**, 1953–1956 (1996).

19. Barsoum, M. W. *et al*. High-resolution transmission electron microscopy of Ti4AlN3, or Ti3Al2N2 revisited. *Journal of the American Ceramic Society* **82**, 2545–2547 (1999).

20. Procopio, A. T., El-Raghy, T. & Barsoum, M. W. Synthesis of Ti4AIN3 and phase equilibria in the Ti-AI-N system. *Metall Mater Trans A Phys Metall Mater Sci* **31**, 373–378 (2000).

21. Eklund, P., Beckers, M., Jansson, U., Högberg, H. & Hultman, L. The Mn + 1AXn phases: Materials science and thin-film processing. *Thin Solid Films* **518**, 1851–1878 (2010).

22. Barsoum, M. W. & Radovic, M. Elastic and mechanical properties of the MAX phases. *Annu Rev Mater Res* **41**, 195–227 (2011).

23. Pang, W. K., Low, I. M. & Sun, Z. M. In situ high-temperature diffraction study of the thermal dissociation of Ti3AlC2 in vacuum. *Journal of the American Ceramic Society* **93**, 2871–2876 (2010).

24. Emmerlich, J. *et al*. Thermal stability of Ti3SiC2 thin films. *Acta Mater* **55**, 1479–1488 (2007).

25. El-Raghy, T. & Barsoum, M. W. Diffusion kinetics of the carburization and silicidation of Ti3SiC2. *J Appl Phys* **83**, 112–119 (1998).

26. Barsoum, M. W. *et al*. The Topotactic Transformation of Ti3SiC2 into a Partially Ordered Cubic Ti (C 0.67Si0.06) Phase by the Diffusion of Si into Molten Cryolite. *J Electrochem Soc* **146**, 3919–3923 (1999).

27. Naguib, M. *et al*. Two-dimensional nanocrystals produced by exfoliation of Ti 3AlC 2. *Advanced Materials* **23**, 4248–4253 (2011).

28. Naguib, M. *et al*. Two-dimensional transition metal carbides. *ACS Nano* **6**, 1322–1331 (2012).

29. Halim, J. *et al*. X-ray photoelectron spectroscopy of select multi-layered transition metal carbides (MXenes). *Appl Surf Sci* **362**, 406–417 (2016).

30. Wang, H. W., Naguib, M., Page, K., Wesolowski, D. J. & Gogotsi, Y. Resolving the Structure of Ti3C2Tx MXenes through Multilevel Structural Modeling of the Atomic Pair Distribution Function. *Chemistry of Materials* **28**, 349–359 (2016).

31. Hope, M. A. *et al*. NMR reveals the surface functionalisation of Ti3C2 MXene. *Physical Chemistry Chemical Physics* **18**, 5099–5102 (2016).

32. Naguib, M. *et al*. New two-dimensional niobium and vanadium carbides as promising materials for li-ion batteries. *J Am Chem Soc* **135**, 15966–15969 (2013).

33. Naguib, M., Mochalin, V. N., Barsoum, M. W. & Gogotsi, Y. 25th anniversary article: MXenes: A new family of two-dimensional materials. *Advanced Materials* **26**, 992–1005 (2014).

34. Ghidiu, M., Lukatskaya, M. R., Zhao, M. Q., Gogotsi, Y. & Barsoum, M. W. Conductive two-dimensional titanium carbide ‘clay’ with high volumetric capacitance. *Nature* **516**, 78–81 (2015).

35. Wang, X. *et al*. A new etching environment (FeF3/HCl) for the synthesis of two-dimensional titanium carbide MXenes: A route towards selective reactivity: Vs. water. *J Mater Chem A Mater* **5**, 22012–22023 (2017).

36. Naguib, M., Unocic, R. R., Armstrong, B. L. & Nanda, J. Large-scale delamination of multi-layer transition metal carbides and carbonitrides 'MXenes'. *Dalton Transactions* **44**, 9353–9358 (2015).

37. Lipatov, A. *et al*. Effect of Synthesis on Quality, Electronic Properties and Environmental Stability of Individual Monolayer Ti3C2 MXene Flakes. *Adv Electron Mater* **2**, (2016).

38. Sang, X. *et al*. Atomic defects in monolayer titanium carbide (Ti3C2Tx) MXene. *ACS Nano* **10**, 9193–9200 (2016).

39. Alhabeb, M. *et al*. Guidelines for Synthesis and Processing of Two-Dimensional Titanium Carbide (Ti3C2Tx MXene). *Chemistry of Materials* **29**, 7633–7644 (2017).

40. Halim, J. *et al*. Synthesis and Characterization of 2D Molybdenum Carbide (MXene). *Adv Funct Mater* **26**, 3118–3127 (2016).

41. Liu, F. *et al*. Preparation of Ti 3 C 2 and Ti 2 C MXenes by fluoride salts etching and methane adsorptive properties. *Appl Surf Sci* **416**, 781–789 (2017).

42. Hart, J. L. *et al*. Control of MXenes' electronic properties through termination and intercalation. *Nat Commun* **10**, (2019).

43. Khazaei, M., Ranjbar, A., Arai, M., Sasaki, T. & Yunoki, S. Electronic properties and applications of MXenes: a theoretical review. *J Mater Chem C Mater* **5**, 2488–2503 (2017).

44. Khazaei, M. *et al*. Novel electronic and magnetic properties of two-dimensional transition metal carbides and nitrides. *Adv Funct Mater* **23**, 2185–2192 (2013).

45. Ying, Y. *et al*. Two-dimensional titanium carbide for efficiently reductive removal of highly toxic chromium(VI) from water. *ACS Appl Mater Interfaces* **7**, 1795–1803 (2015).

46. Lunardi, C. N., Gomes, A. J., Rocha, F. S., de Tommaso, J. & Patience, G. S. Experimental methods in chemical engineering: Zeta potential. *Canadian Journal of Chemical Engineering* **99**, 627–639 (2021).

47. Eda, G., Mattevi, C., Yamaguchi, H., Kim, H. & Chhowalla, M. Insulator to semimetal transition in graphene oxide. *Journal of Physical Chemistry C* **113**, 15768–15771 (2009).

48. Zhang, J. *et al*. Scalable Manufacturing of Free-Standing, Strong Ti3C2Tx MXene Films with Outstanding Conductivity. *Advanced Materials* **32**, 1–9 (2020).

49. Wang, X., Zhi, L. & Müllen, K. Transparent, conductive graphene electrodes for dye-sensitized solar cells. *Nano Lett* **8**, 323–327 (2008).

50. Becerril, H. A. *et al*. Evaluation of solution-processed reduced graphene oxide films as transparent conductors. *ACS Nano* **2**, 463–470 (2008).

51. Sun, Y., Chen, D. & Liang, Z. Two-dimensional MXenes for energy storage and conversion applications. *Mater Today Energy* **5**, 22–36 (2017).

52. Lukatskaya, M. R. *et al*. Probing the Mechanism of High Capacitance in 2D Titanium Carbide Using in Situ X-Ray Absorption Spectroscopy. *Adv Energy Mater* **5**, 2–5 (2015).

53. Zhan, C. *et al*. Understanding the MXene Pseudocapacitance. *Journal of Physical Chemistry Letters* **9**, 1223–1228 (2018).

54. Liu, J. *et al*. Advanced Energy Storage Devices: Basic Principles, Analytical Methods, and Rational Materials Design. *Advanced Science* **5**, (2018).

55. Malik, V., Srivastava, S., Bhatnagar, M. K. & Vishnoi, M. Comparative study and analysis between Solid Oxide Fuel Cells (SOFC) and Proton Exchange Membrane (PEM) fuel cell - A review. *Mater Today Proc* **47**, 2270–2275 (2021).

56. Wang, Y. *et al*. Single Atom Catalysts for Fuel Cells and Rechargeable Batteries: Principles, Advances, and Opportunities. *ACS Nano* **15**, 210–239 (2021).

57. Costa, C. M. *et al*. Recycling and environmental issues of lithium-ion batteries: Advances, challenges and opportunities. *Energy Storage Mater* **37**, 433–465 (2021).

58. Marin Halper James C Ellenbogen, V. S. *Supercapacitors: A Brief Overview*. http://www.mitre.org/tech/nanotech (2006).

59. Bird, J. *Electrical circuit theory and technology*. (Routledge, 2017).

60. Simon, P., Gogotsi, Y. & Dunn, B. Where do batteries end and supercapacitors begin? *Science (1979)* **343**, 1210–1211 (2014).

61. Yip, G., Qiu, J., Ng, W. T. & Lu, Z. H. Effect of metal contacts on the electrical characteristics of Al 2O3 dielectric thin films. *Appl Phys Lett* **92**, 1–4 (2008).

62. Yu, A., Chabot, V. & Zhang, J. *Electrochemical supercapacitors for energy storage and delivery: Fundamentals and applications*. *Electrochemical Supercapacitors for Energy Storage and Delivery: Fundamentals and Applications* (CRC Press, 2017). doi:10.1201/b14671.

63. Zhang, L. & Zhao, X. S. Carbon-based materials as supercapacitor electrodes. *Chem Soc Rev* **38**, 2520–2531 (2009).

64. Rafik, F., Gualous, H., Gallay, R., Crausaz, A. & Berthon, A. Frequency, thermal and voltage supercapacitor characterization and modeling. *J Power Sources* **165**, 928–934 (2007).

65. Eyer, J., Corey, G. P. & SANDIA. Energy storage for the electricity grid: Benefits and market potential assessment guide. *A study for the DOE energy storage systems program* 232 (2010).

66. Gogotsi, Y. & Penner, R. M. Energy Storage in Nanomaterials - Capacitive, Pseudocapacitive, or Battery-like? *ACS Nano* **12**, 2081–2083 (2018).

67. Secor, E. B. Principles of aerosol jet printing. *Flexible and Printed Electronics* **3**, (2018).

68. Marquez, G. J., Renn, M. J. & Miller, W. D. Aerosol-based direct-write of biological materials for biomedical applications. *Materials Research Society Symposium - Proceedings* **698**, 343–349 (2002).

69. Marinov, V. R. Electrical Resistance of Laser Sintered Direct-Write Deposited Materials for Microelectronic Applications. *Journal of Microelectronics and Electronic Packaging* **1**, 261–268 (2004).

70. Maher, M., Smith, A. & Margiotta, J. A synopsis of the Defense Advanced Research Projects Agency (DARPA) investment in additive manufacture and what challenges remain. *Laser 3D Manufacturing* **8970**, 897002 (2014).

71. Paulsen, J. A., Renn, M., Christenson, K. & Plourde, R. Printing conformal electronics on 3D structures with aerosol jet technology. *FIIW 2012 - 2012 Future of Instrumentation International Workshop Proceedings* 47–50 (2012) doi:10.1109/FIIW.2012.6378343.

72. Wilkinson, N. J., Smith, M. A. A., Kay, R. W. & Harris, R. A. A review of aerosol jet printing—a non-traditional hybrid process for micro-manufacturing. *International Journal of Advanced Manufacturing Technology* **105**, 4599–4619 (2019).

73. Mahajan, A., Frisbie, C. D. & Francis, L. F. Optimization of aerosol jet printing for high-resolution, high-aspect ratio silver lines. *ACS Appl Mater Interfaces* **5**, 4856–4864 (2013).

74. Zhao, D. *et al*. Conductivity enhancement of aerosol-jet printed electronics by using silver nanoparticles ink with carbon nanotubes. *Microelectron Eng* **96**, 71–75 (2012).

75. Rosker, E. S. *et al.* Approaching the Practical Conductivity Limits of Aerosol Jet Printed Silver. *ACS Appl Mater Interfaces* **12**, 29684–29691 (2020).

76. Jabari, E. & Toyserkani, E. Aerosol-Jet printing of highly flexible and conductive graphene/silver patterns. *Mater Lett* **174**, 40–43 (2016).

77. Liu, R. *et al*. All-carbon-based field effect transistors fabricated by aerosol jet printing on flexible substrates. *Journal of Micromechanics and Microengineering* **23**, (2013).

78. Jabari, E. & Toyserkani, E. Micro-scale aerosol-jet printing of graphene interconnects. *Carbon N Y* **91**, 321–329 (2015).

79. Ha, M. *et al*. Aerosol jet printed, low voltage, electrolyte gated carbon nanotube ring oscillators with sub-5 μs stage delays. *Nano Lett* **13**, 954–960 (2013).

80. Goh, G. L., Agarwala, S. & Yeong, W. Y. Aerosol-Jet-Printed Preferentially Aligned Carbon Nanotube Twin-Lines for Printed Electronics. *ACS Appl Mater Interfaces* **11**, 43719–43730 (2019).

81. Lu, S. *et al*. Flexible, Print-in-Place 1D-2D Thin-Film Transistors Using Aerosol Jet Printing. *ACS Nano* **13**, 11263–11272 (2019).

82. Cao, C., Andrews, J. B. & Franklin, A. D. Completely Printed, Flexible, Stable, and Hysteresis-Free Carbon Nanotube Thin-Film Transistors via Aerosol Jet Printing. *Adv Electron Mater* **3**, 1–10 (2017).

83. Zhao, D. *et al*. Conductivity enhancement of aerosol-jet printed electronics by using silver nanoparticles ink with carbon nanotubes. *Microelectron Eng* **96**, 71–75 (2012).

84. Tait, J. G. *et al*. Uniform Aerosol Jet printed polymer lines with 30 μm width for 140 ppi resolution RGB organic light emitting diodes. *Org Electron* **22**, 40–43 (2015).

85. Tarabella, G., Vurro, D., Lai, S., Angelo, P. D. & Ascari, L. Aerosol jet printing of PEDOT : PSS for large area flexible electronics.

86. Yang, C., Zhou, E., Miyanishi, S., Hashimoto, K. & Tajima, K. Preparation of active layers in polymer solar cells by aerosol jet printing. *ACS Appl Mater Interfaces* **3**, 4053–4058 (2011).

87. Folgar, C. E., Suchicital, C. & Priya, S. Solution-based aerosol deposition process for synthesis of multilayer structures. *Mater Lett* **65**, 1302–1307 (2011).

88. Xie, W., Zhang, X., Leighton, C. & Frisbie, C. D. 2D Insulator–Metal Transition in Aerosol-Jet-Printed Electrolyte-Gated Indium Oxide Thin Film Transistors. *Adv Electron Mater* **3**, 1–6 (2017).

89. Williams, N. X., Watson, N., Joh, D. Y., Chilkoti, A. & Franklin, A. D. Aerosol jet printing of biological inks by ultrasonic delivery. *Biofabrication* **12**, (2020).

90. Xiao, Y., Kalaitzidou, K., Yao, D., Yeo, W. H. & Harris, T. A. L. Challenges and Advances in Aerosol Jet Printing of Regenerated Silk Fibroin Solutions. *Adv Mater Interfaces* **7**, 1–5 (2020).

91. Degryse, O., Bloemen, V. & Ferraris, E. Collagen composite inks for Aerosol Jet® printing in bone tissue engineering applications. *Procedia CIRP* **110**, 180–185 (2022).

92. Cheng, P. K. *et al.* Nonlinear optical properties of two-dimensional palladium ditelluride (PdTe2) and its application as aerosol jet printed saturable absorbers for broadband ultrafast photonics. *Appl Mater Today* **26**, 101296 (2022).

93. Li, Y. *et al.* Aerosol Jet Printed WSe2 Crossbar Architecture Device on Kapton with Dual Functionality as Resistive Memory and Photosensor for Flexible System Integration. *IEEE Sens J* **20**, 4653–4659 (2020).

94. Ouyang, J., Cormier, D., Williams, S. A. & Borkholder, D. A. Photonic Sintering of Aerosol Jet Printed Lead Zirconate Titanate (PZT) Thick Films. *Journal of the American Ceramic Society* **99**, 2569–2577 (2016).

95. Glushkova, A. *et al.* Ultrasensitive 3D Aerosol-Jet-Printed Perovskite X-ray Photodetector. *ACS Nano* **15**, 4077–4084 (2021).

96. Lu, S. *et al.* Uniform and Stable Aerosol Jet Printing of Carbon Nanotube Thin-Film Transistors by Ink Temperature Control. *ACS Appl Mater Interfaces* **12**, 43083–43089 (2020).

97. Borghetti, M., Serpelloni, M., Sardini, E., Spurling, D. & Nicolosi, V. Temperature influence on Ti3C2Tx lines printed by aerosol jet printing. *Sens Actuators A Phys* **332**, 113185 (2021).

98. Deiner, L. J. & Reitz, T. L. Inkjet and Aerosol Jet Printing of Electrochemical Devices for Energy Conversion and Storage. *Adv Eng Mater* **19**, 1–18 (2017).

99. Deiner, L. J., Jenkins, T., Howell, T. & Rottmayer, M. Aerosol Jet Printed Polymer Composite Electrolytes for Solid-State Li-Ion Batteries. *Adv Eng Mater* **21**, 1900952 (2019).

100. Wu, Y. *et al*. Crumpled and Eccentric Nanospheres of Ti3C2Tx MXene by Aerosol Jet Printing on Heat Substrate. *Adv Eng Mater* **24**, (2022).

101. Jahn, D. *et al*. Digital Aerosol Jet Printing for the Fabrication of Terahertz Metamaterials. *Adv Mater Technol* **3**, 1–6 (2018).

102. Shastri, A. *et al*. 3D printing of millimetre wave and low-terahertz frequency selective surfaces using aerosol jet technology. *IEEE Access* **8**, 177341–177350 (2020).

103. Craton, M. T., Konstantinou, X., Albrecht, J. D., Chahal, P. & Papapolymerou, J. A chip-first microwave package using multimaterial aerosol jet printing. *IEEE Trans Microw Theory Tech* **68**, 3418–3427 (2020).

104. Oakley, C. & Chahal, P. Aerosol Jet Printed Quasi-Optical Terahertz Components. *IEEE Trans Terahertz Sci Technol* **8**, 765–772 (2018).

105. Turan, N. *et al*. Atmospheric Pressure and Ambient Temperature Plasma Jet Sintering of Aerosol Jet Printed Silver Nanoparticles. *ACS Appl Mater Interfaces* **13**, 47244–47251 (2021).

106. Zhao, D., Liu, T., Zhang, M., Liang, R. & Wang, B. Fabrication and characterization of aerosol-jet printed strain sensors for multifunctional composite structures. *Smart Mater Struct* **21**, (2012).

107. Zhu, Y., Yu, L., Wu, D., Lv, W. & Wang, L. A high-sensitivity graphene ammonia sensor via aerosol jet printing. *Sens Actuators A Phys* **318**, 112434 (2021).

108. Agarwala, S. *et al*. Wearable Bandage-Based Strain Sensor for Home Healthcare: Combining 3D Aerosol Jet Printing and Laser Sintering. *ACS Sens* **4**, 218–226 (2019).

109. Parate, K. *et al*. Aerosol-Jet-Printed Graphene Immunosensor for Label-Free Cytokine Monitoring in Serum. *ACS Appl Mater Interfaces* **12**, 8592–8603 (2020).

110. Cantù, E. *et al*. Aerosol jet printed 3D electrochemical sensors for protein detection. *Sensors (Switzerland)* **18**, 1–14 (2018).

111. Parate, K. *et al*. Aerosol-jet-printed graphene electrochemical histamine sensors for food safety monitoring. *2d Mater* **7**, (2020).

112. di Novo, N. G., Cantù, E., Tonello, S., Sardini, E. & Serpelloni, M. Support-material-free microfluidics on an electrochemical sensors platform by aerosol jet printing. *Sensors (Switzerland)* **19**, (2019).

113. Gupta, A. A., Arunachalam, S., Cloutier, S. G. & Izquierdo, R. Fully Aerosol-Jet Printed, High-Performance Nanoporous ZnO Ultraviolet Photodetectors. *ACS Photonics* **5**, 3923–3929 (2018).

114. Kopola, P. *et al*. Aerosol jet printed grid for ITO-free inverted organic solar cells. *Solar Energy Materials and Solar Cells* **107**, 252–258 (2012).

115. Eckstein, R., Hernandez-Sosa, G., Lemmer, U. & Mechau, N. Aerosol jet printed top grids for organic optoelectronic devices. *Org Electron* **15**, 2135–2140 (2014).

116. Christenson, K. K., Paulsen, J. A., Renn, M. J., McDonald, K. & Bourassa, J. Direct printing of circuit boards using Aerosol Jet®. *International Conference on Digital Printing Technologies* 433–436 (2011).

117. Smith, M., Choi, Y. S., Boughey, C. & Kar-Narayan, S. Controlling and assessing the quality of aerosol jet printed features for large area and flexible electronics. *Flexible and Printed Electronics* **2**, (2017).

118. Elmogi, A. *et al*. Aerosol-jet printed interconnects for 2.5 D electronic and photonic integration. *Journal of Lightwave Technology* **36**, 3528–3533 (2018).

119. Rahman, T., Renaud, L., Heo, D., Renn, M. & Panat, R. Aerosol based direct-write micro-additive fabrication method for sub-mm 3D metal-dielectric structures. *Journal of Micromechanics and Microengineering* **25**, (2015).

120. Saleh, M. S., Hu, C. & Panat, R. Three-dimensional microarchitected materials and devices using nanoparticle assembly by pointwise spatial printing. *Sci Adv* **3**, (2017).

121. Saleh, M. S., Hu, C., Brenneman, J., al Mutairi, A. M. & Panat, R. 3D printed three-dimensional metallic microlattices with controlled and tunable mechanical properties. *Addit Manuf* **39**, 101856 (2021).

122. Umrani, A. Fabrication of micro pillar arrays via aerosol jet printing. *Advisor: Denis Cormier* (Rochester Institute of Technology, 2015).

123. Mette, A., Richter, P. L., Hörteis, M. & Glunz, S. W. Metal aerosol jet printing for solar cell metallization. *Progress in Photovoltaics: Research and Applications* **15**, 621–627 (2007).

124. Derby, B. Inkjet printing of functional and structural materials: Fluid property requirements, feature stability, and resolution. *Annu Rev Mater Res* **40**, 395–414 (2010).

125. Binder, S., Glatthaar, M. & Rädlein, E. Analytical investigation of aerosol jet printing. *Aerosol Science and Technology* **48**, 924–929 (2014).

126. Renn, M. J., Christenson, K. K., Giroux, D. & Blazej, D. Aerosol Jet® Printing of Conductive Epoxy for 3D Packaging. *Pan Pacific Microelectronics Symposium* 1–7 (2013).

127. Cheek, K., Neville, E. & D'Arezzo, K. Aerosol Jet® AJ 300 System User Manual. *Optomec, Inc* 260 (2016).

128. Goodridge, C. L., Hentschel, H. G. E. & Lathrop, D. P. Breaking faraday waves: Critical slowing of droplet ejection rates. *Phys Rev Lett* **82**, 3062–3065 (1999).

129. Deepu, P., Peng, C. & Moghaddam, S. Dynamics of ultrasonic atomization of droplets. *Exp Therm Fluid Sci* **92**, 243–247 (2018).

130. Donnelly, T. D. *et al*. Using ultrasonic atomization to produce an aerosol of micron-scale particles. *Review of Scientific Instruments* **76**, 1–10 (2005).

131. Donnelly, T. D. *et al*. An experimental study of micron-scale droplet aerosols produced via ultrasonic atomization. *Physics of Fluids* **16**, 2843–2851 (2004).

132. Goodridge, C. L., Shi, W. T. & Lathrop, D. P. Threshold dynamics of singular gravity-capillary waves. *Phys Rev Lett* **76**, 1824–1827 (1996).

133. Goodridge, C. L., Tao Shi, W., Hentschel, H. G. E. & Lathrop, D. P. Viscous effects in droplet-ejecting capillary waves. *Phys Rev E Stat Phys Plasmas Fluids Relat Interdiscip Topics* **56**, 472–475 (1997).

134. Lang, R. J. Ultrasonic Atomization of Liquids. *J Acoust Soc Am* **34**, 6–8 (1962).

135. William Thomson, B. K. XLVI. Hydrokinetic solutions and observations. *The London, Edinburgh, and Dublin Philosophical Magazine and Journal of Science* **42**, 362–377 (1871).

136. Eisenmenger, W. Dynamic properties of the surface tension of water and aqueous solutions of surface active agents with standing capillary waves in the frequency range from 10 kc/s to 1.5 Mc/s. *Acta Acustica united with Acustica* **9**, (1959).

137. Chen, G., Gu, Y., Tsang, H., Hines, D. R. & Das, S. The Effect of Droplet Sizes on Overspray in Aerosol-Jet Printing. *Adv Eng Mater* **20**, 1701084 (2018).

138. Pallas, N. R. & Harrison, Y. An automated drop shape apparatus and the surface tension of pure water. *Colloids and Surfaces* **43**, 169–194 (1990).

139. Ball, P. Water: Water - An enduring mystery. *Nature* **452**, 291–292 (2008).

140. Zhang, Y., Liu, C. & Whalley, D. Direct-write techniques for maskless production of microelectronics: A review of current state-of-the-art technologies. *2009 International Conference on Electronic Packaging Technology and High Density Packaging, ICEPT-HDP 2009* 497–503 (2009) doi:10.1109/ICEPT.2009.5270702.

141. Williams, B. A. *et al*. Copper-Zinc-Tin-Sulfide Thin Films via Annealing of Ultrasonic Spray Deposited Nanocrystal Coatings. *ACS Appl Mater Interfaces* **9**, 18865–18871 (2017).

142. Tafoya, R. R. & Secor, E. B. Understanding and mitigating process drift in aerosol jet printing. *Flexible and Printed Electronics* **5**, (2020).

143. Tan, C. W. & Hsu, C. J. Diffusion of aerosols in laminar flow in a cylindrical tube. *J Aerosol Sci* **2**, 117–124 (1971).

144. Thomas, J. W. Gravity settling of particles in a horizontal tube. *J Air Pollut Control Assoc* **8**, 32–34 (1958).

145. Gormley, P. G. & Kennedy, M. Diffusion from a Stream Flowing through a Cylindrical Tube. *Proceedings of the Royal Irish Academy. Section A: Mathematical and Physical Sciences* **52**, 163–169 (1949).

146. Renn, M. J. United States Patent US 7,108,894 B2. (2006).

147. Kahn, B. The M3D aerosol jet system, an alternative to inkjet printing for printed electronics. *Organic and Printed Electronics* **1**, 14–17 (2007).

148. Lall, P., Abrol, A., Kothari, N., Leever, B. & Miller, S. Effect of Print Parameters on Print Consistency of Aerosol Jet Printed Electronics. in *2019 18th IEEE Intersociety Conference on Thermal and Thermomechanical Phenomena in Electronic Systems (ITherm)* 633–642 (2019). doi:10.1109/ITHERM.2019.8757268.

149. Wang, X., Kruis, F. E. & McMurry, P. H. Aerodynamic focusing of nanoparticles: I. Guidelines for designing aerodynamic lenses for nanoparticles. *Aerosol Science and Technology* **39**, 611–623 (2005).

150. Hoey, J. M., Lutfurakhmanov, A., Schulz, D. L. & Akhatov, I. S. A review on aerosol-based direct-write and its applications for microelectronics. *J Nanotechnol* **2012**, (2012).

151. Israel, G. W. & Friedlander, S. K. High-speed beams of small particles. *J Colloid Interface Sci* **24**, 330–337 (1967).

152. de La Mora, J. F. & Riesco-Chueca, P. Aerodynamic focusing of particles in a carrier gas. *J Fluid Mech* **195**, 1–21 (1988).

153. Hinds, W. C. & Zhu, Y. *Aerosol technology: properties, behavior, and measurement of airborne particles*. (John Wiley & Sons, 2022).

154. Secor, E. B. Guided ink and process design for aerosol jet printing based on annular drying effects. *Flexible and Printed Electronics* **3**, (2018).

155. Ha, M. *et al*. Aerosol-jet-printed, 1 volt h-bridge drive circuit on plastic with integrated electrochromic pixel. *ACS Appl Mater Interfaces* **5**, 13198–13206 (2013).

156. Marple, V. A. & Liu, B. Y. H. Characteristics of Laminar Jet Impactors. *Environ Sci Technol* **8**, 648–654 (1974).

157. Stringer, J. & Derby, B. Formation and stability of lines produced by inkjet printing. *Langmuir* **26**, 10365–10372 (2010).

158. Yarin, A. L. Drop impact dynamics: Splashing, spreading, receding, bouncing.. *Annu Rev Fluid Mech* **38**, 159–192 (2006).

159. Reitberger, T., Hoerber, J., Schramm, R., Sennefelder, S. & Franke, J. Aerosol Jet® printing of optical waveguides. *Proceedings of the International Spring Seminar on Electronics Technology* **2015-Septe**, 5–10 (2015).

160. Gupta, A. A., Bolduc, A., Cloutier, S. G. & Izquierdo, R. Aerosol Jet Printing for printed electronics rapid prototyping. *Proceedings - IEEE International Symposium on Circuits and Systems* **2016-July**, 866–869 (2016).

161. Span, R. & Wagner, W. A new equation of state for carbon dioxide covering the fluid region from the triple-point temperature to 1100 K at pressures up to 800 MPa. *J Phys Chem Ref Data* **25**, 1509–1596 (1996).

162. Humphreys, W. J. & Henk, W. G. Critical point drying of biological specimens. *Scan Electron Microsc* **VOL. 2**, 235–240 (1979).

163. Land, V. D., Harris, T. M. & Teeters, D. C. Processing of low-density silica gel by critical point drying or ambient pressure drying. *J Non Cryst Solids* **283**, 11–17 (2001).

164. A. Mark Smith. *From Sight to Light: The Passage from Ancient to Modern Optics*. *University of Chicago Press* (2014). doi:https://doi.org/10.1002/bewi.201601795.

165. Hänninen, P. Light microscopy: Beyond the diffraction limit. *Nature* **419**, 802 (2002).

166. Hell, S. W. Nobel Lecture: Nanoscopy with freely propagating light. *Rev Mod Phys* **87**, 1169 (2015).

167. Kohl, H. & Reimer, L. Transmission Electron Microscopy. *Springer Series in Optical Sciences* **36**, (2008).

168. Rottenfusser, R., Wilson, E. E. & Davidson, M. W. Numerical Aperture and Resolution. Preprint at (2020).

169. Raja, P. M. v & Barron, A. R. *Physical methods in chemistry and nano science*. *Rice University* (2019). doi:10.1002/jctb.5000533702.

170. Knoll, M. & Ruska, E. Das elektronenmikroskop. *Zeitschrift für physik* **78**, 318–339 (1932).

171. Davies, T. E. *et al*. Experimental methods in chemical engineering: Scanning electron microscopy and X-ray ultra-microscopy—SEM and XuM. *Can J Chem Eng* **100**, 3145–3159 (2022).

172. Egerton, R. F. & others. *Physical principles of electron microscopy*. vol. 56 (Springer, 2005).

173. Egerton, R. F., McLeod, R., Wang, F. & Malac, M. Basic questions related to electron-induced sputtering in the TEM. *Ultramicroscopy* **110**, 991–997 (2010).

174. Egerton, R. F. Mechanisms of radiation damage in beam-sensitive specimens, for TEM accelerating voltages between 10 and 300 kV. *Microsc Res Tech* **75**, 1550–1556 (2012).

175. David, B. W. & Carter, C. B. *Transmission electron microscopy: A textbook for materials science*. (Springer Science+ Business Media, LLC, 1996).

176. Hillyard, S. & Silcox, J. Detector geometry, thermal diffuse scattering and strain effects in ADF STEM imaging. *Ultramicroscopy* **58**, 6–17 (1995).

177. Goldstein, J. I. *et al*. *Scanning electron microscopy and X-ray microanalysis*. (Springer, 2017).

178. Bogner, A., Jouneau, P. H., Thollet, G., Basset, D. & Gauthier, C. A history of scanning electron microscopy developments: Towards 'wet-STEM' imaging. *Micron* **38**, 390–401 (2007).

179. Bogner, A., Thollet, G., Basset, D., Jouneau, P. H. & Gauthier, C. Wet STEM: A new development in environmental SEM for imaging nano-objects included in a liquid phase. *Ultramicroscopy* **104**, 290–301 (2005).

180. Pendse, D. R. & Chin, A. K. Cathodoluminescence and Transmission Cathodoluminescence. in *Encyclopedia of Materials: Science and Technology* (eds. Buschow, K. H. J. et al.) 1–7 (Elsevier, 2001). doi:https://doi.org/10.1016/B0-08-043152-6/00190-X.

181. Kowoll, T. *et al*. Contrast of backscattered electron SEM images of nanoparticles on substrates with complex structure. *Scanning* **2017**, (2017).

182. Golla-Schindler, U. *et al*. Imaging Li–Ion Battery Material with Low Voltage Backscattered Electrons – comparison of a Field Emission SEM Crossbeam540/Merlin with the DELTA SEM. *Microscopy and Microanalysis* **25**, 448–449 (2019).

183. Mehedi, H. A. *et al*. Formation of oriented nanostructures in diamond using metallic nanoparticles. *Nanotechnology* **23**, (2012).

184. Perkampus, H.-H. *UV-VIS Spectroscopy and its Applications*. (Springer Science & Business Media, 2013).

185. Chang, C. C. Auger electron spectroscopy. *Surf Sci* **25**, 53–79 (1971).

186. Berti, E., Cardoso, V. & Will, C. M. Gravitational-wave spectroscopy of massive black holes with the space interferometer LISA. *Physical Review D - Particles, Fields, Gravitation and Cosmology* **73**, 1–41 (2006).

187. Winefordner, J. D. & Vickers, T. J. Atomic Fluorescence Spectrometry as a Means of Chemical Analysis. *Anal Chem* **36**, 161–165 (1964).

188. Bohr, N. On the constitution of atoms and molecules. *Philosophical Magazine* **26**, 37 (1913).

189. Einstein, A. On a Heuristic Point of View about the Creation and Conversion of Light, translated from german by Haar, T. *Ann Phys* **17**, 132–148 (1905).

190. Anslyn, E. v & Dougherty, D. A. *Modern physical organic chemistry*. (University science books, 2006).

191. Kreibig, U. & Vollmer, M. *Optical properties of metal clusters*. (Springer, 1995).

192. Amendola, V., Pilot, R., Frasconi, M., Maragò, O. M. & Iatì, M. A. Surface plasmon resonance in gold nanoparticles: A review. *Journal of Physics Condensed Matter* **29**, (2017).

193. Arnold, M. D. & Blaber, M. G. Optical performance and metallic absorption in nanoplasmonic systems. *Opt Express* **17**, 3835 (2009).

194. Brar, S. K. & Verma, M. Measurement of nanoparticles by light-scattering techniques. *TrAC - Trends in Analytical Chemistry* **30**, 4–17 (2011).

195. Raman, C. v. & Krishnan, K. S. A new type of secondary radiation. *Nature* **121**, 501–502 (1928).

196. McCreery, R. L. *Raman Spectroscopy for Chemical Analysis*. *Measurement Science and Technology* vol. 12 (2001).

197. Young, A. T. Rayleigh scattering. *Appl. Opt.* **20**, 533–535 (1981).

198. Bunker, P. R. & Jensen, P. *Molecular symmetry and spectroscopy*. vol. 46853 (NRC research press, 2006).

199. Liang, F. *et al*. Raman spectroscopy characterization of two-dimensional materials. *Chinese Physics B* **27**, (2018).

200. Thompson, A. C. *et al*. *X-RAY DATA BOOKLET*. (Lawrence Berkeley National Laboratory, 2001).

201. Haug, E. & Nakel, W. *The elementary process of bremsstrahlung*. vol. 73 (World Scientific, 2004).

202. Statham, P. J. Measuring Performance of Energy-Dispersive X-ray Systems. *Microscopy and Microanalysis* **4**, 605–615 (1998).

203. Carter, C. B. & Williams, D. B. *Transmission electron microscopy: Diffraction, imaging, and spectrometry*. (Springer, 2016).

204. Han, Y. *et al*. Deep learning STEM-EDX tomography of nanocrystals. *Nat Mach Intell* **3**, 267–274 (2021).

205. Hua, Y. Estimating Method for Electron Beam Accelerating Voltage Used in Energy-Dispersive X-Ray Microanalysis: Application in Failure Analysis of Wafer Fabrication. *Instrum Sci Technol* **32**, 115–126 (2004).

206. Egerton, R. F. Choice of operating voltage for a transmission electron microscope. *Ultramicroscopy* **145**, 85–93 (2014).

207. Ahn, C. C., Krivanek, O. L. & Disko, M. M. *EELS atlas a reference collection of electron energy loss spectra covering all stable elements*. (HREM Facility, Center for Solid State Science, Arizona State University, 1983).

208. Egerton, R. F. Electron energy-loss spectroscopy in the TEM. *Reports on Progress in Physics* **72**, 16502 (2008).

209. Sasaki, T. *et al*. Performance of low-voltage STEM/TEM with delta corrector and cold field emission gun. *J Electron Microsc (Tokyo)* **59**, 7–13 (2010).

210. Leapman, R. D., Fiori, C. E. & Swyt, C. R. Mass thickness determination by electron energy loss for quantitative X-ray microanalysis in biology. *J Microsc* **133**, 239–253 (1984).

211. Malis, T., Cheng, S. C. & Egerton, R. F. EELS log-ratio technique for specimen-thickness measurement in the TEM. *J Electron Microsc Tech* **8**, 193–200 (1988).

212. Bragg, W. H. The Reflection of X-Rays by Crystals. *Nature* **91**, 477 (1913).

213. Hammond, C. *The basics of crystallography and diffraction*. vol. 21 (International Union of Crystal, 2015).

214. Bagotsky, V. S. *Fundamentals of electrochemistry*. (John Wiley & Sons, 2005).

215. Gamry Instruments. Two-, Three-, and Four-Electrode Experiments. Preprint at (2011).

216. Elgrishi, N. *et al*. A Practical Beginner's Guide to Cyclic Voltammetry. *J Chem Educ* **95**, 197–206 (2018).

217. Zhang, S. & Pan, N. Supercapacitors performance evaluation. *Adv Energy Mater* **5**, 1–19 (2015).

218. Alano, J. H. *et al.* A simple and complete supercapacitor characterization system using a programmable sourcemeter. *Orbital* **11**, 133–141 (2019).

219. Chang, B. Y. & Park, S. M. Electrochemical impedance spectroscopy. *Annual Review of Analytical Chemistry* **3**, 207–229 (2010).

220. Frackowiak, E. & Béguin, F. Carbon materials for the electrochemical storage of energy in capacitors. *Carbon N Y* **39**, 937–950 (2001).

221. Zuliani, J. E., Caguiat, J. N., Kirk, D. W. & Jia, C. Q. Considerations for consistent characterization of electrochemical double-layer capacitor performance. *J Power Sources* **290**, 136–143 (2015).

222. Stoller, M. D. & Ruoff, R. S. Best practice methods for determining an electrode material's performance for ultracapacitors. *Energy Environ Sci* **3**, 1294–1301 (2010).

223. Chen, T. & Dai, L. Flexible supercapacitors based on carbon nanomaterials. *J Mater Chem A Mater* **2**, 10756–10775 (2014).

224. Noori, A., El-Kady, M. F., Rahmanifar, M. S., Kaner, R. B. & Mousavi, M. F. Towards establishing standard performance metrics for batteries, supercapacitors and beyond. *Chem Soc Rev* **48**, 1272–1341 (2019).

225. Saka, M. *Metallic micro and nano materials: fabrication with atomic diffusion*. (Springer Science & Business Media, 2011).

226. Krupka, J. Contactless methods of conductivity and sheet resistance measurement for semiconductors, conductors and superconductors. *Meas Sci Technol* **24**, (2013).

227. Harvard University. *Guidelines for the Safe Use of Hydrofluoric Acid*. *Department of Chemistry* vol. 2 (2007).

228. Maleski, K., Ren, C. E., Zhao, M. Q., Anasori, B. & Gogotsi, Y. Size-Dependent Physical and Electrochemical Properties of Two-Dimensional MXene Flakes. *ACS Appl Mater Interfaces* **10**, 24491–24498 (2018).

229. Orangi, J., Hamade, F., Davis, V. A. & Beidaghi, M. 3D Printing of Additive-Free 2D Ti3C2Tx (MXene) Ink for Fabrication of Micro-Supercapacitors with Ultra-High Energy Densities. *ACS Nano* **14**, 640–650 (2020).

230. Shekhirev, M., Shuck, C. E., Sarycheva, A. & Gogotsi, Y. Characterization of MXenes at every step, from their precursors to single flakes and assembled films. *Prog Mater Sci* **120**, 100757 (2021).

231. Mathis, T. S. *et al*. Modified MAX Phase Synthesis for Environmentally Stable and Highly Conductive Ti3C2MXene. *ACS Nano* **15**, 6420–6429 (2021).

232. Ward, J. *et al*. Crystallographic evolution of MAX phases in proton irradiating environments. *Journal of Nuclear Materials* **502**, 220–227 (2018).

233. Chang, F., Li, C., Yang, J., Tang, H. & Xue, M. Synthesis of a new graphene-like transition metal carbide by de-intercalating Ti3AlC2. *Mater Lett* **109**, 295–298 (2013).

234. von Treifeldt, J. E. *et al*. The effect of Ti3AlC2 MAX phase synthetic history on the structure and electrochemical properties of resultant Ti3C2 MXenes. *Mater Des* **199**, 109403 (2021).

235. Yang, D. & Frindt, R. F. Powder x-ray diffraction of two-dimensional materials. *J Appl Phys* **79**, 2376–2385 (1996).

236. Hu, T. *et al*. Vibrational properties of Ti3C2 and Ti3C2T2 (T = O, F, OH) monosheets by first-principles calculations: A comparative study. *Physical Chemistry Chemical Physics* **17**, 9997–10003 (2015).

237. Mauchamp, V. *et al*. Enhanced and tunable surface plasmons in two-dimensional Ti3 C2 stacks: Electronic structure versus boundary effects. *Phys Rev B Condens Matter Mater Phys* **89**, 1–6 (2014).

238. Lin, H., Wang, X., Yu, L., Chen, Y. & Shi, J. Two-Dimensional Ultrathin MXene Ceramic Nanosheets for Photothermal Conversion. *Nano Lett* **17**, 384–391 (2017).

239. Li, R., Zhang, L., Shi, L. & Wang, P. MXene Ti3C2: An Effective 2D Light-to-Heat Conversion Material. *ACS Nano* **11**, 3752–3759 (2017).

240. Khatun, N., Dey, S., Behera, G. C. & Roy, S. C. Ti3C2Tx MXene functionalization induced enhancement of photoelectrochemical performance of TiO2 nanotube arrays. *Mater Chem Phys* **278**, 125651 (2022).

241. Tang, J. *et al*. Optimizing Ion Pathway in Titanium Carbide MXene for Practical High-Rate Supercapacitor. *Adv Energy Mater* **11**, 1–8 (2021).

242. Huang, X. & Wu, P. A Facile, High-Yield, and Freeze-and-Thaw-Assisted Approach to Fabricate MXene with Plentiful Wrinkles and Its Application in On-Chip Micro-Supercapacitors. *Adv Funct Mater* **30**, 1910048 (2020).

243. Xuan, J. *et al.* Organic-Base-Driven Intercalation and Delamination for the Production of Functionalized Titanium Carbide Nanosheets with Superior Photothermal Therapeutic Performance. *Angewandte Chemie - International Edition* **55**, 14569–14574 (2016).

244. Cai, X., Luo, Y., Liu, B. & Cheng, H. M. Preparation of 2D material dispersions and their applications. *Chem Soc Rev* **47**, 6224–6266 (2018).

245. Han, F. *et al.* Boosting the Yield of MXene 2D Sheets via a Facile Hydrothermal-Assisted Intercalation. *ACS Appl Mater Interfaces* **11**, 8443–8452 (2019).

246. Wu, W. *et al.* Two-Dimensional Nanosheets by Rapid and Efficient Microwave Exfoliation of Layered Materials. *Chemistry of Materials* **30**, 5932–5940 (2018).

247. Lukatskaya, M. R. *et al.* Ultra-high-rate pseudocapacitive energy storage in two-dimensional transition metal carbides. *Nat Energy* **6**, 1–6 (2017).

248. Zhang, C. J. *et al.* Stamping of Flexible, Coplanar Micro-Supercapacitors Using MXene Inks. *Adv Funct Mater* **28**, 1–10 (2018).

249. Zhang, C. (John) *et al.* Additive-free MXene inks and direct printing of micro-supercapacitors. *Nat Commun* **10**, 1795 (2019).

250. Akuzum, B. *et al.* Rheological Characteristics of 2D Titanium Carbide (MXene) Dispersions: A Guide for Processing MXenes. *ACS Nano* **12**, 2685–2694 (2018).

251. Quain, E. *et al*. Direct Writing of Additive-Free MXene-in-Water Ink for Electronics and Energy Storage. *Adv Mater Technol* **4**, 1800256 (2019).

252. Wang, Y. *et al*. Three-dimensional porous MXene/layered double hydroxide composite for high performance supercapacitors. *J Power Sources* **327**, 221–228 (2016).

253. Yang, W. *et al*. 3D Printing of Freestanding MXene Architectures for Current-Collector-Free Supercapacitors. *Advanced Materials* **31**, 1902725 (2019).

254. Beidaghi, M. & Gogotsi, Y. Capacitive energy storage in micro-scale devices: recent advances in design and fabrication of micro-supercapacitors. *Energy Environ Sci* **7**, 867 (2014).

255. Wei, M. *et al*. 3D direct writing fabrication of electrodes for electrochemical storage devices. *J Power Sources* **354**, 134–147 (2017).

256. Saleh, M. S., Li, J., Park, J. & Panat, R. 3D printed hierarchically-porous microlattice electrode materials for exceptionally high specific capacity and areal capacity lithium ion batteries. *Addit Manuf* **23**, 70–78 (2018).

257. Shah, S. A. *et al*. Template-free 3D titanium carbide (Ti3C2Tx) MXene particles crumpled by capillary forces. *Chemical Communications* **53**, 400–403 (2017).

258. Mathis, T. S. *et al*. Energy Storage Data Reporting in Perspective—Guidelines for Interpreting the Performance of Electrochemical Energy Storage Systems. *Adv Energy Mater* **9**, 1–13 (2019).

259. Jha, S. *et al*. Additively manufactured electrodes for supercapacitors: A review. *Appl Mater Today* **26**, 101220 (2022).

260. U.S. Department of Energy. Energy Storage Grand Challenge Energy Storage Market Report 2020. *U.S. Department of Energy* **Technical**, 65 (2020).

261. Li, W., Erickson, E. M. & Manthiram, A. High-nickel layered oxide cathodes for lithium-based automotive batteries. *Nat Energy* **5**, 26–34 (2020).

262. Li, W. *et al*. Mn versus Al in Layered Oxide Cathodes in Lithium-Ion Batteries: A Comprehensive Evaluation on Long-Term Cyclability. *Adv Energy Mater* **8**, 1703154 (2018).

263. Berrueta, A., Ursua, A., Martin, I. S., Eftekhari, A. & Sanchis, P. Supercapacitors: Electrical Characteristics, Modeling, Applications, and Future Trends. *IEEE Access* **7**, 50869–50896 (2019).

264. Barra, P. H. A., de Carvalho, W. C., Menezes, T. S., Fernandes, R. A. S. & Coury, D. v. A review on wind power smoothing using high-power energy storage systems. *Renewable and Sustainable Energy Reviews* vol. 137 Preprint at https://doi.org/10.1016/j.rser.2020.110455 (2021).

265. Yu, A., Chabot, V. & Zhang, J. *Electrochemical supercapacitors for energy storage and delivery: Fundamentals and applications*. *Electrochemical Supercapacitors for Energy Storage and Delivery: Fundamentals and Applications* (CRC Press, 2017). doi:10.1201/b14671.

266. Wang, G., Zhang, L. & Zhang, J. A review of electrode materials for electrochemical supercapacitors. *Chem Soc Rev* **41**, 797–828 (2012).

267. Xia, Y. *et al*. Thickness-independent capacitance of vertically aligned liquid-crystalline MXenes. *Nature* **557**, 409–412 (2018).

268. Zhang, C. J. *et al*. Stamping of Flexible, Coplanar Micro-Supercapacitors Using MXene Inks. *Adv Funct Mater* **28**, 1–10 (2018).

269. Tontini, G., Greaves, M., Ghosh, S., Bayram, V. & Barg, S. MXene-based 3D porous macrostructures for electrochemical energy storage. *JPhys Materials* **3**, (2020).

270. Li, S. *et al*. Intercalation of Metal Ions into Ti3C2Tx MXene Electrodes for High-Areal-Capacitance Microsupercapacitors with Neutral Multivalent Electrolytes. *Adv Funct Mater* **30**, (2020).

271. Simon, P. Two-Dimensional MXene with Controlled Interlayer Spacing for Electrochemical Energy Storage. *ACS Nano* **11**, 2393–2396 (2017).

272. Zhao, M. Q. *et al*. Flexible MXene/carbon nanotube composite paper with high volumetric capacitance. *Advanced Materials* **27**, 339–345 (2015).

273. Li, K. *et al*. An Ultrafast Conducting Polymer@MXene Positive Electrode with High Volumetric Capacitance for Advanced Asymmetric Supercapacitors. *Small* **16**, (2020).

274. Bayram, V. *et al*. MXene Tunable Lamellae Architectures for Supercapacitor Electrodes. *ACS Appl Energy Mater* **3**, 411–422 (2020).

275. Li, L., Zhang, M., Zhang, X. & Zhang, Z. New Ti3C2 aerogel as promising negative electrode materials for asymmetric supercapacitors. *J Power Sources* **364**, 234–241 (2017).

276. Liu, J. *et al*. Multifunctional, Superelastic, and Lightweight MXene/Polyimide Aerogels. *Small* **14**, (2018).

277. Wang, X. *et al*. 3D Ti3C2T: X aerogels with enhanced surface area for high performance supercapacitors. *Nanoscale* **10**, 20828–20835 (2018).

278. Li, W., Liu, J. & Zhao, D. Mesoporous materials for energy conversion and storage devices. *Nat Rev Mater* **1**, (2016).

279. Schneider, D., Mehlhorn, D., Zeigermann, P., Kärger, J. & Valiullin, R. Transport properties of hierarchical micro-mesoporous materials. *Chem Soc Rev* **45**, 3439–3467 (2016).

280. Yue, Y. *et al*. Highly Self-Healable 3D Microsupercapacitor with MXene-Graphene Composite Aerogel. *ACS Nano* **12**, 4224–4232 (2018).

281. Tontini, G., Greaves, M., Ghosh, S., Bayram, V. & Barg, S. MXene-based 3D porous macrostructures for electrochemical energy storage. *JPhys Materials* **3**, (2020).

282. Wang, Q., Yan, J. & Fan, Z. Carbon materials for high volumetric performance supercapacitors: Design, progress, challenges and opportunities. *Energy Environ Sci* **9**, 729–762 (2016).

283. Luo, Y. *et al*. Micro-Structural and Flexible Reduced Graphene Oxide/Ti3C2Tx Composite Film Electrode with Long Cycle Life for Supercapacitor. *Adv Mater Interfaces* **9**, 2101619 (2022).

284. Zhao, Z., Wang, S., Wan, F., Tie, Z. & Niu, Z. Scalable 3D Self-Assembly of MXene Films for Flexible Sandwich and Microsized Supercapacitors. *Adv Funct Mater* **31**, 1–7 (2021).

285. Rasch, F. *et al.* Wet-Chemical Assembly of 2D Nanomaterials into Lightweight, Microtube-Shaped, and Macroscopic 3D Networks. *ACS Appl Mater Interfaces* **11**, 44652–44663 (2019).

286. Schütt, F. *et al.* Hierarchical self-entangled carbon nanotube tube networks. *Nat Commun* **8**, 1–10 (2017).

287. Krüger, H. *et al.* Double Hierarchical 3D Carbon Nanotube Network with Tailored Structure as a Lithium Sulfur Cathode. in *Proceedings of the 2021 IEEE 11th International Conference 'Nanomaterials: Applications and Properties', NAP 2021* (2021). doi:10.1109/NAP51885.2021.9568505.

288. Mecklenburg, M. *et al.* Aerographite: Ultra lightweight, flexible nanowall, carbon microtube material with outstanding mechanical performance. *Advanced Materials* **24**, 3486–3490 (2012).

289. Meija, R. *et al.* Nanomechanics of individual aerographite tetrapods. *Nat Commun* **8**, 1–9 (2017).

290. Sarycheva, A. & Gogotsi, Y. Raman Spectroscopy Analysis of the Structure and Surface Chemistry of Ti3C2T xMXene. *Chemistry of Materials* **32**, 3480–3488 (2020).

291. Meltzman, H. *et al.* An experimental method for calibration of the plasmon mean free path. *J Microsc* **236**, 165–173 (2009).

292. Shao, H. *et al.* Unraveling the charge storage mechanism of Ti3C2Tx MXene electrode in acidic electrolyte. *ACS Energy Lett* **5**, 2873–2880 (2020).

293. Wu, J., Yuan, X. Z. & Wang, H. Cyclic voltammetry. *PEM Fuel Cell Diagnostic Tools* 71–85 (2011) doi:10.1201/9781439807842.ch10.

294. Tichter, T., Schneider, J. & Roth, C. Convolutive modeling of cyclic voltammetry, AC-voltammetry, sine wave voltammetry and impedance spectroscopy with interfacial CPE behaviour and uncompensated ohmic resistances: A Unified Theory. *Electrochim Acta* **393**, 139006 (2021).

295. MacArthur, D. M. The Proton Diffusion Coefficient for the Nickel Hydroxide Electrode. *J Electrochem Soc* **117**, 729 (1970).

296. Lindström, H. *et al*. Li+ ion insertion in TiO2 (anatase). 1. Chronoamperometry on CVD films and nanoporous films. *Journal of Physical Chemistry B* **101**, 7710–7716 (1997).

297. Wang, J., Polleux, J., Lim, J. & Dunn, B. Pseudocapacitive contributions to electrochemical energy storage in TiO 2 (anatase) nanoparticles. *Journal of Physical Chemistry C* **111**, 14925–14931 (2007).

298. Wang, Y., Wang, J., Zhang, X., Bhattacharyya, D. & Sabolsky, E. M. Quantifying Environmental and Economic Impacts of Highly Porous Activated Carbon from Lignocellulosic Biomass for High-Performance Supercapacitors. *Energies (Basel)* **15**, (2022).

299. Mishra, Y. K. *et al*. Fabrication of macroscopically flexible and highly porous 3D semiconductor networks from interpenetrating nanostructures by a simple flame transport approach. *Particle and Particle Systems Characterization* **30**, 775–783 (2013).

300. Iakoubovskii, K., Mitsuishi, K., Nakayama, Y. & Furuya, K. Thickness measurements with electron energy loss spectroscopy. *Microsc Res Tech* **71**, 626–631 (2008).

8 SUPPLEMENTARY FIGURES

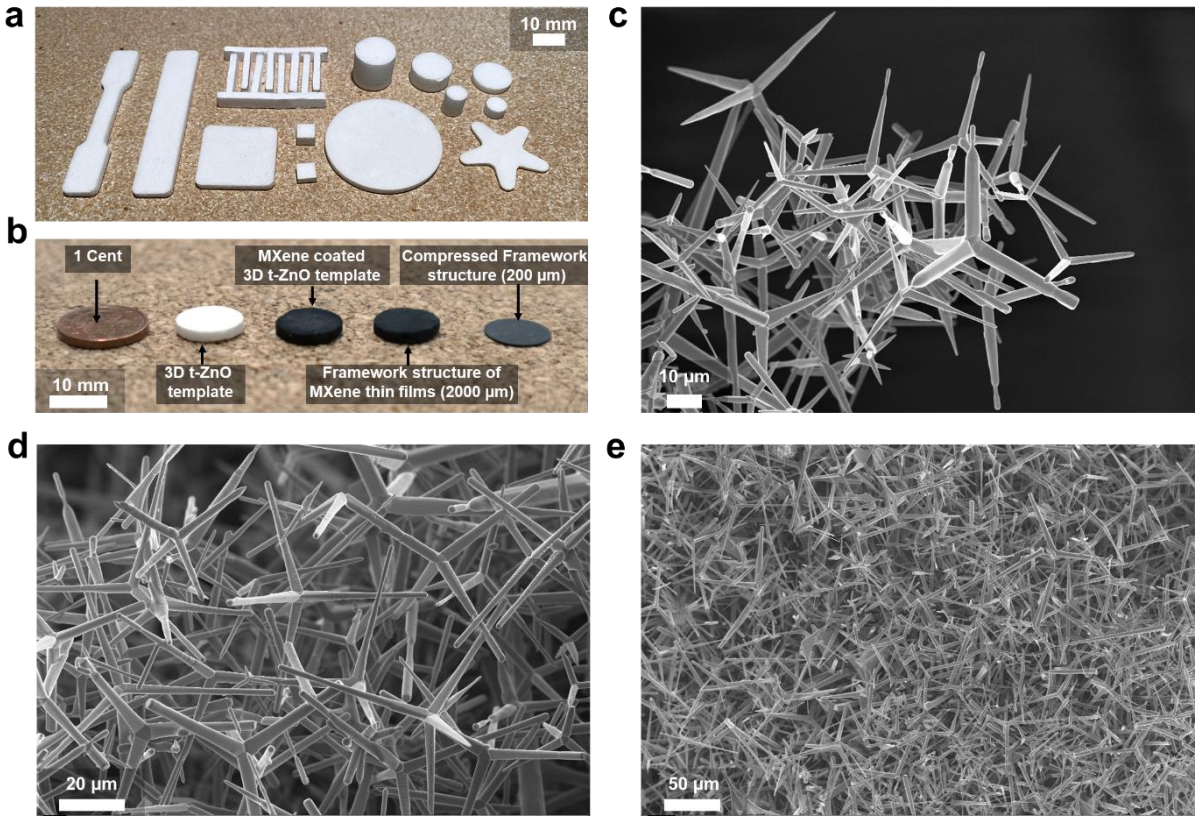

Figure S 1: (a) Photograph of t-ZnO templates with different shapes and sizes illustrating the versatility of the template approach. (b) Photograph comparing the 3D t-ZnO template, the MXene coated 3D t-ZnO template, the etched and dried framework structure of MXene thin films as well as a 10 times compressed framework structure with a 1 Cent coin. (c-e) SEM images of the 3D t-ZnO template material at different magnifications indicating the highly porous structure composed of interconnected, tetrapodal ZnO.

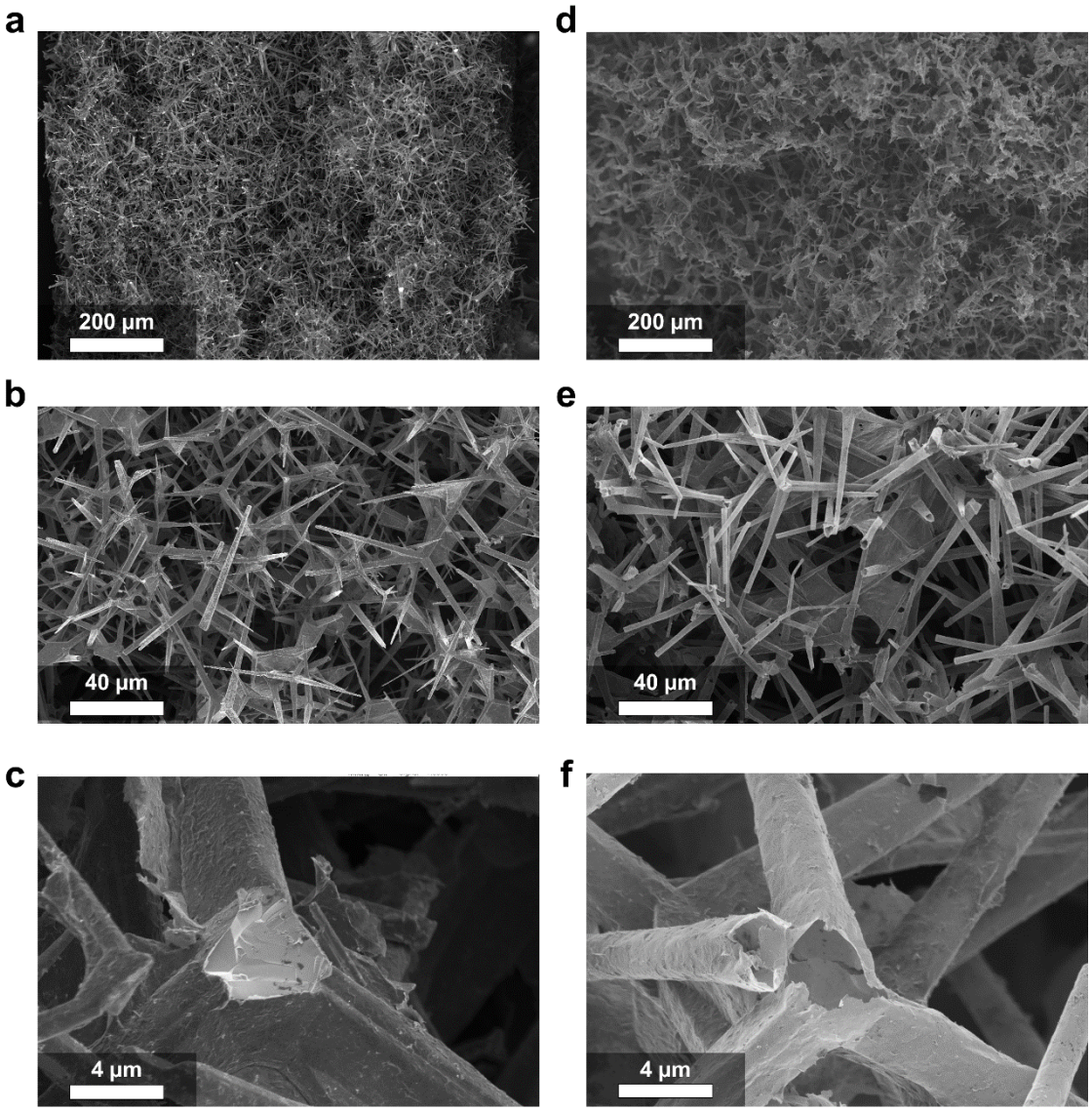

Figure S 2: (a-c) SEM images of the MXene-coated 3D t-ZnO template structure at different magnifications, showing a homogeneous thin layer of MXene flakes on the ZnO template structure. (d-f) SEM images of the etched and dried framework structure at different magnifications, showing the perfect negative of the previous 3D t-ZnO structure with MXene flakes in the form of thin film microtubes.

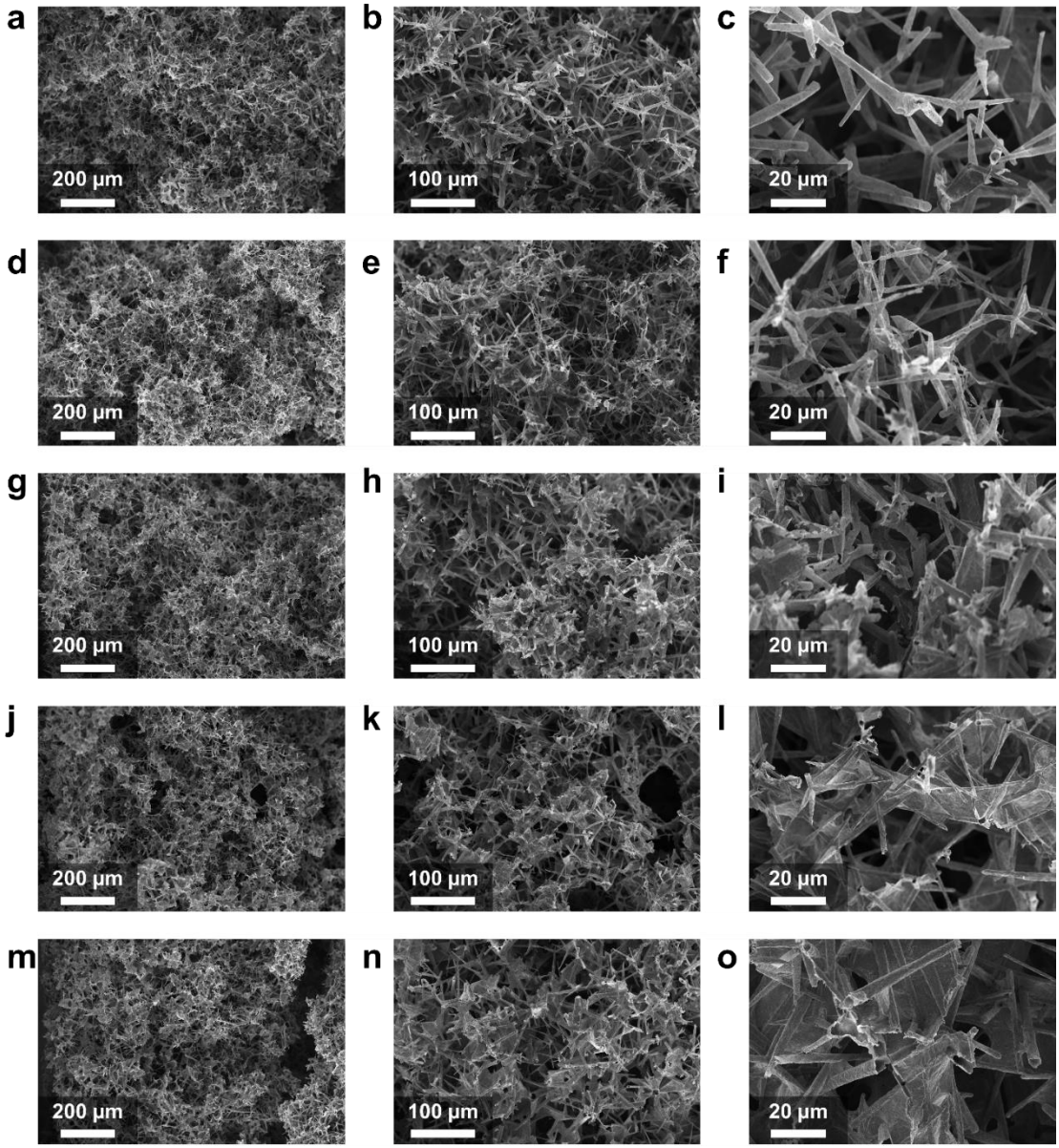

Figure S 3: SEM images at different magnification of the prepared AMX-4D-2000 (a-c), AMX-8D-2000 (d-f), AMX-12D-2000 (g-i), AMX-16D-2000 (j-l) and AMX-20D-2000 (m-o).

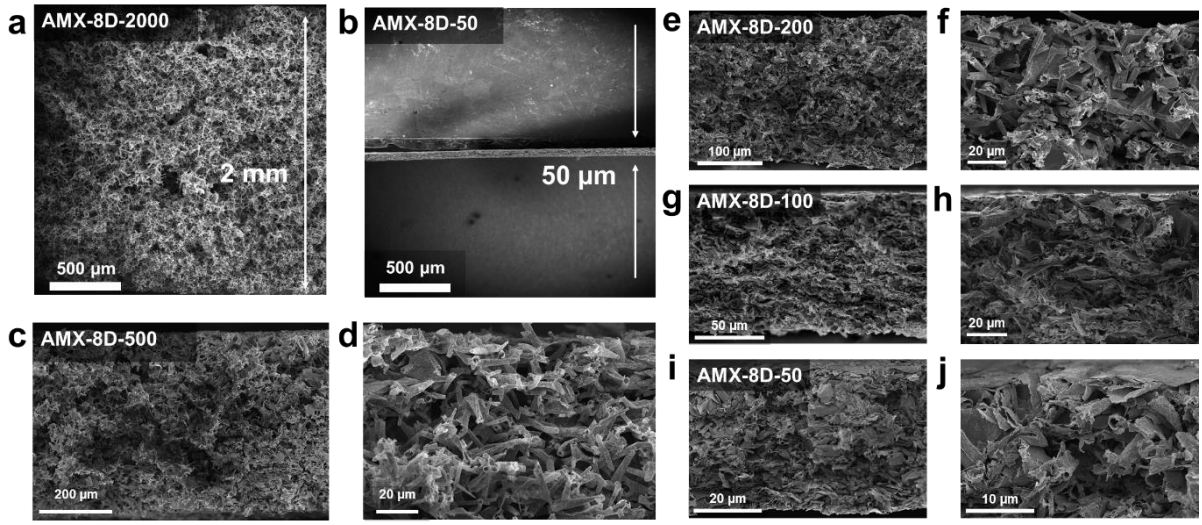

Figure S 4: SEM images at different magnification of AMX cross-sections. Comparison of the cross-section of an AMX-8D-2000 (a) and AMX-8D-50 (b) at same magnification indicating the compression. (c-d) Cross-section of an AMX-8D-500 at different magnification. (e-f) Cross-section of an AMX-8D-200 at different magnification. (g-h) Cross-section of an AMX-8D-200 at different magnification. (i-j) Cross-section of an AMX-8D-50 at different magnification.

X-ray diffraction (XRD)

The synthesized AMX was characterized with XRD, using a Bruker D8 Discovery X-ray Diffractometer in θ/2θ configuration, in the range of 3−75 °, at 2° min^{-1}. D-spacing was calculated from the $Ti_3C_2T_x$ (002) reflection according to the formula for Bragg's law:

$$n\lambda = 2d \sin\theta$$

Where n is the diffraction order, λ is the wavelength of x-rays, d is the grating constant and θ is the glancing angle.

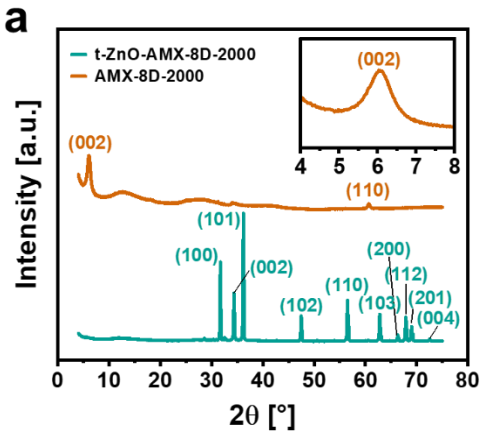

Figure S 5: (a) XRD studies of a MXene-coated 3D t-ZnO structure as well as a freestanding AMX-8D structure. Inset: MXene (0 0 2) peak at 2θ = 6.03°, corresponding to a d-spacing of 1.47 nm.

Raman Studies

Raman spectroscopy analysis was done using an alpha 300 RA (WITech system) with a CCD detector at an excitation wavelength of 532.2 nm. The sample studied before electrochemical testing (Figure S a) was used without further preparation. Samples cycled for different number of cycles were rinsed properly in DI water and dried under inert atmosphere (Figure S b).

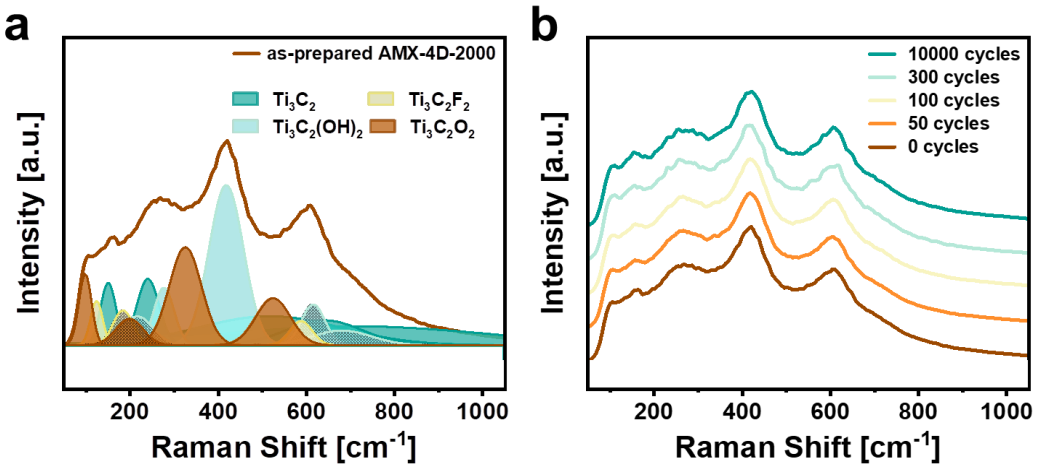

Figure S 6: (a) Raman data of the as-prepared aeromaterial and (b) after various cycle numbers.

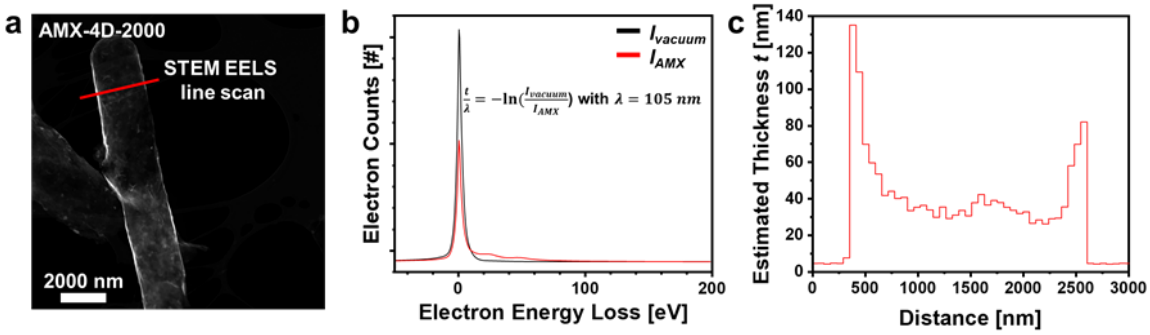

Figure S 7: Representative images for determining the MXene microtube film thickness by EELS. (a) HAADF-STEM micrograph along an individual freestanding MXene microtube thin film. (b) Exemplary EELS spectra of the zero-loss peak at two points, over vacuum and over the MXene microtube thin film. (c) Estimated thickness scan along the red path in (a) calculated via the log ratio method assuming a mean free path of 105 nm.

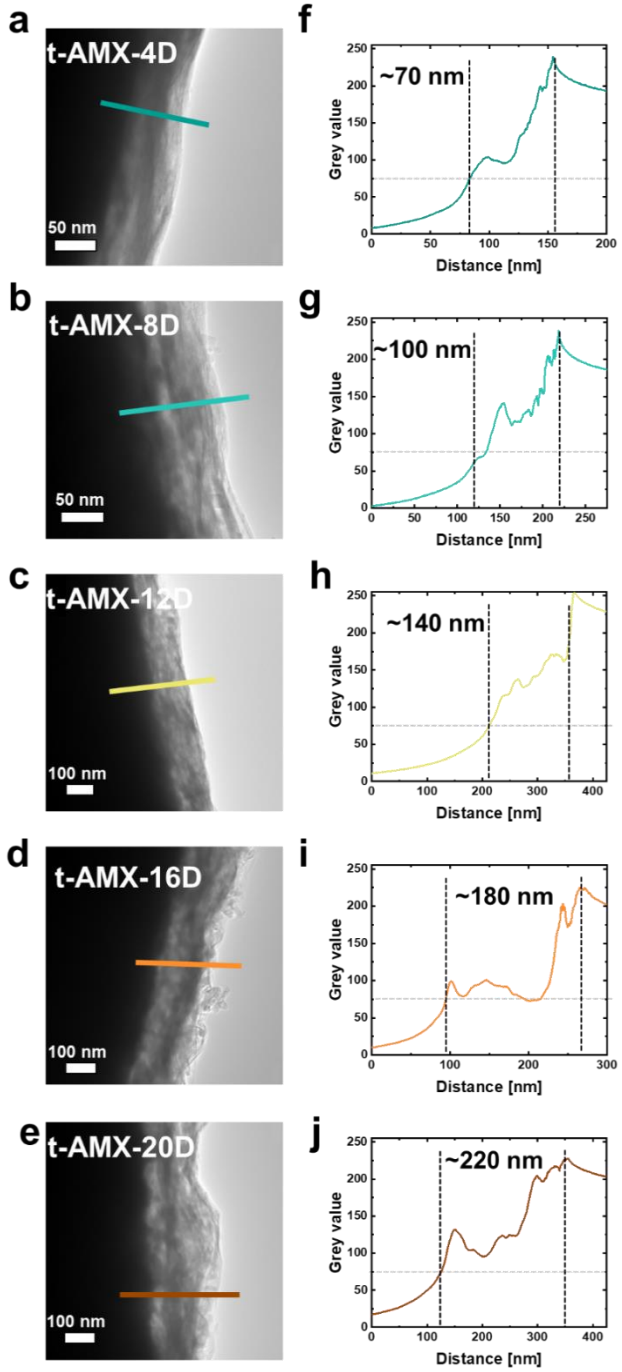

Figure S 8: (a-e) Bright Field images of different t-AMX samples after different number repeated MXene depositions at the interface of ZnO, MXene and air. (f-j) represent a corresponding thickness plot obtained from the intensity profile along the line indicated in the corresponding bright field image

To further showcase the difference in integrated thickness as determined via EELS log ratio versus the effective microtube film thickness including porosity HRTEM micrographs of ZnO tetrapods covered with 4D to 20D of MXene are investigated. The combined mass-thickness and diffraction contrast allow to distinguish between ZnO core and MXene shell using intensity profiles (obtained using Image J). To avoid falsely enlarged film thicknesses due to MXene flakes protruding from the surface orthogonal to the viewing direction sections of local minimum film thickness are evaluated. Here, for statistics, a set of six intensity profiles is evaluated for each brightfield image with respect to MXene layer thickness. In this way it can be safely assumed that only the densely packed MXene layer is counted towards the thickness. The determined thicknesses given in 8 and 9 show a roughly linear increase with the amount of deposited MXene material.

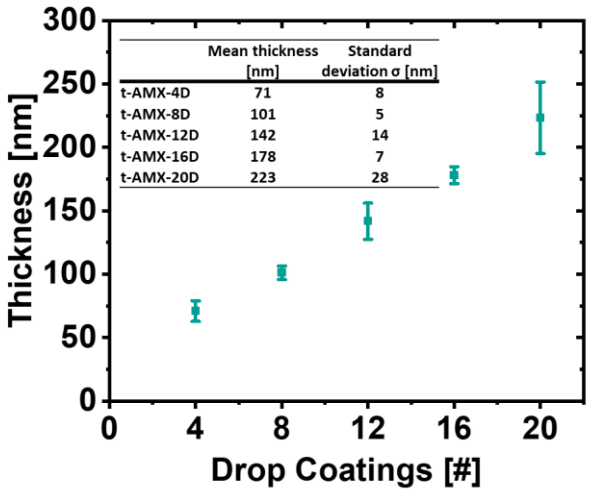

Figure S 9: Mean values from six different intensity profiles of brightfield images in 8 with standard deviation of thickness as a function of the number of drop coatings in AMX preparation. A table with the corresponding values can be found as an inset.

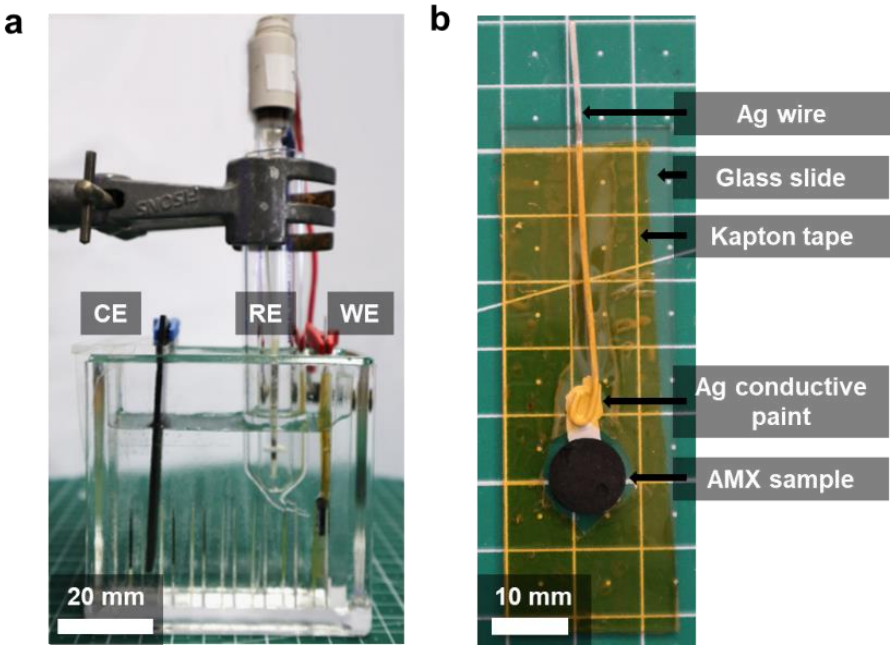

Figure S 10: (a) Three electrode setup for the electrochemical analysis of the synthesized AMX structures with graphite used as the counter electrode (CE), an Ag/AgCl reference electrode (RE) as well as the AMX as the working electrode (WE). (b) Photograph of the electrically contacted AMX sample.

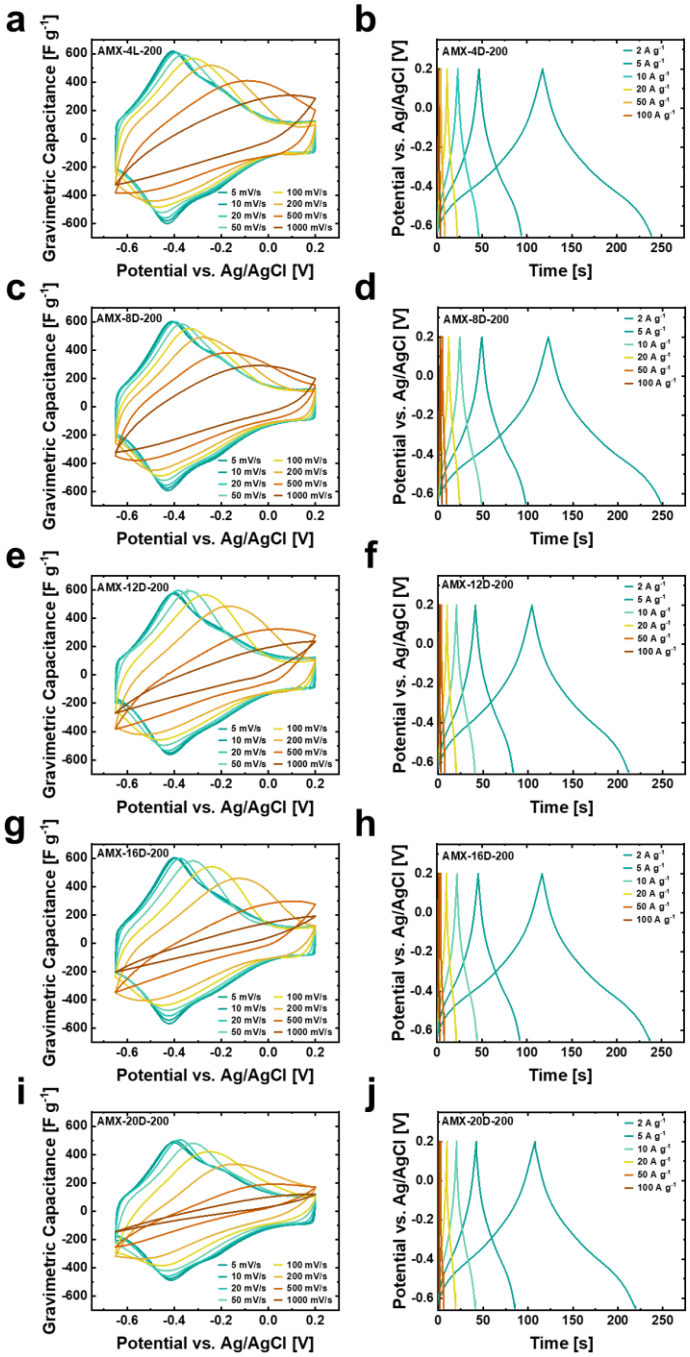

Figure S 11: Electrochemical performance of $Ti_3C_2T_x$ electrodes with tuned nanostructure, namely AMX-4D-200 (a-b), AMX-8D-200 (c-d), AMX-12D-200 (e-f), AMX-16D-200 (g-h) and AMX-20D-200 (i-j), investigated by cyclic voltammetry (5 – 1000 mV s^{-1}) and galvanostatic charge and discharge studies (2 – 100 A g^{-1})

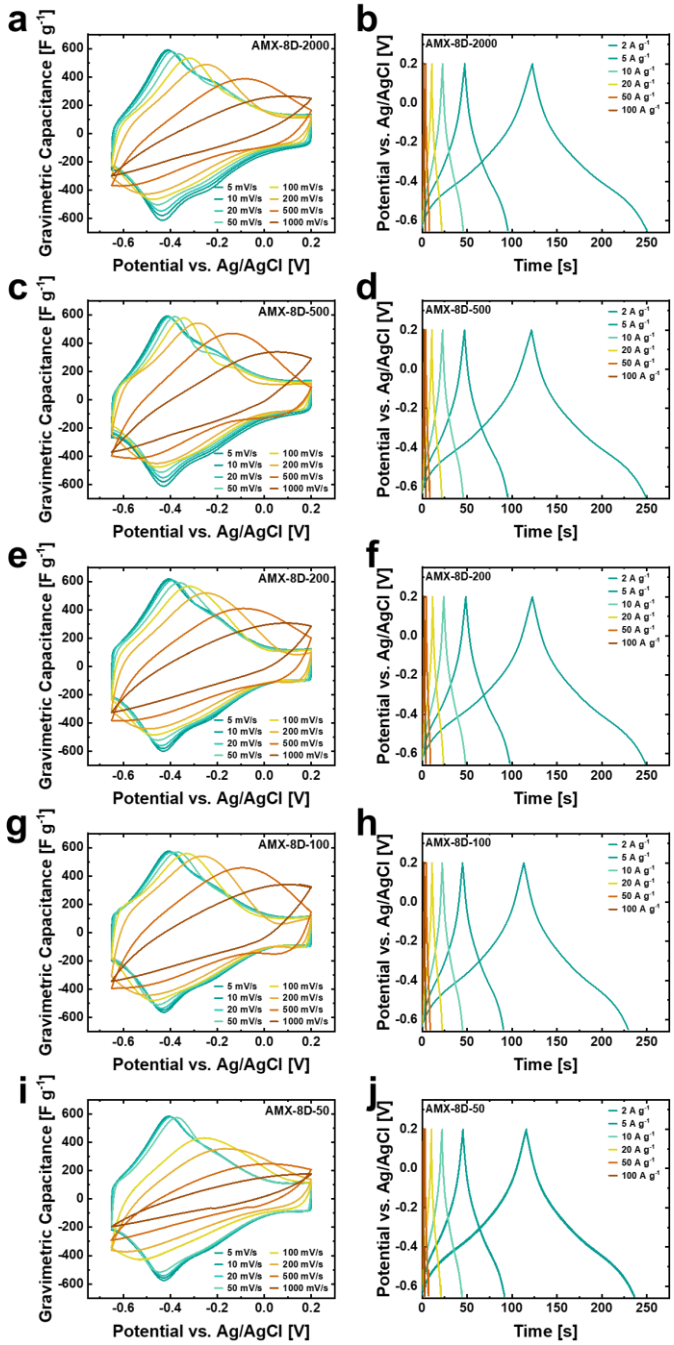

Figure S 12: Electrochemical performance of $Ti_3C_2T_x$ electrodes with tuned microstructure, namely AMX-8D-2000 (a-b), AMX-8D-500 (c-d), AMX-8D-200 (e-f), AMX-8D-100 (g-h) and AMX-8D-50 (i-j), investigated by cyclic voltammetry (5 – 1000 mV s^{-1}) and galvanostatic charge and discharge studies (2 – 100 A g^{-1})

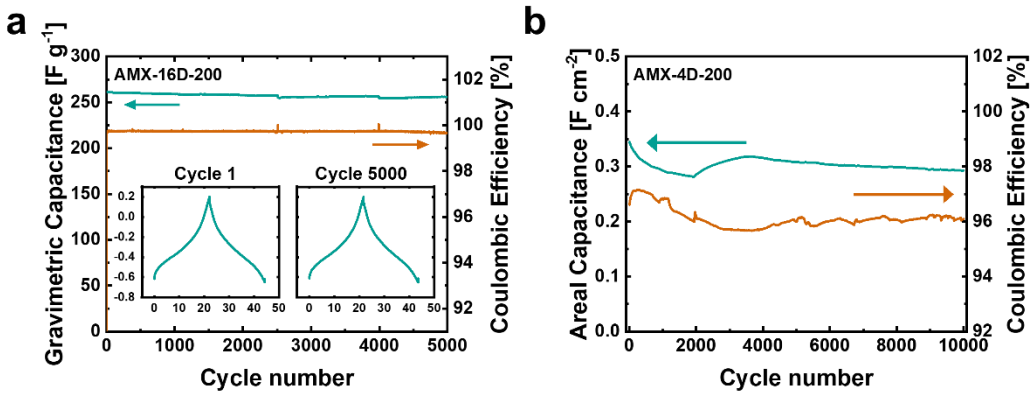

Figure S 13: (a) Long-term cycling with respect to the gravimetric capacitance and coulombic efficiency of the AMX-16D-200 measured with the three-electrode setup with insets indicating the galvanostatic charge and discharge curves of the first and last cycle. (b) Long-term cycling at 9 mA cm^{-2} with respect to the areal capacitance and coulombic efficiency of an AMX-4D-200 assembled in a device against a carbon cloth counter electrode.